Nonlinear Micropolar Models for Composite Materials: Theory and Computation

by

Armanj D. Hasanyan

A dissertation submitted in partial fulfillment
of the requirements for the degree of
Doctor of Philosophy
(Aerospace Engineering)
in the University of Michigan
2018

Doctoral Committee:

Professor Anthony M. Waas, Chair
Associate Professor Nakhiah C. Goulbourne
Associate Professor Veera Sundararaghavan
Professor Alan S. Wineman

Armanj D. Hasanyan

armanj@umich.edu

ORCID iD: 0000-0003-3676-9439

To my *parents* and *brother* for their continuing support.

ACKNOWLEDGMENTS

First, I would like to express my sincere gratitude to my advisor, Dr. Anthony Waas for his guidance through my graduate research. Dr. Waas was always an extremely supportive and caring advisor and I thank him for exposing me to the wonderful world of composite materials. I have truly been inspired by his enthusiasm for research and passion in teaching throughout these years.

I am grateful to Prof. Veera Sundararaghavan, Prof. Nakhiah C. Goulbourne, and Prof. Alan S. Wineman for finding the time to serve on my doctoral committee.

It was a great pleasure to work with my colleagues in the Composite Structures Laboratory. Special thanks to Royan D'Mello, Paul Davidson, Ashith Joseph, Deepak Patel, David Singer, Shiyao Lin, Avinkrishnan Vijayachandran, Linda Leben, Minh Nguyen, Kuo Tian, and many others I had the pleasure to work with throughout the years. I thank you all for our numerous technical discussions, which were invaluable to me.

Most importantly, I would like to thank my family for their unwavering support throughout my graduate career. This thesis would not have been possible without your love and encouragement.

TABLE OF CONTENTS

LIST OF FIGURES

LIST OF TABLES

LIST OF APPENDICES

ABSTRACT

Composites are attractive as lightweight materials for a variety of structural load bearing applications, especially in the aerospace industry. To model their behavior at the global scale (macroscale), continuum models are employed for computational efficiency. However, classical (Cauchy) continuum models often disregard the local structural effects, such as local bending and rotations of the constituents. For example, fiber reinforced composites, which are generally composed of fibers surrounded by polymer matrix material, when subjected to macroscopic loading, the fibers at the microscale undergo local bending and rotations. Similarly, in cellular materials, such as honeycomb structures and foams, when viewed as an assembly of beams or shells, there is inherent bending of cell walls introduced into the continuum deformation.

The higher order micropolar continuum theory, which is an extension of a Cauchy continuum, introduces these higher order effects with the generalization of the kinematic degrees of freedom. In addition to the displacement field, there is also an additional independent rotational field introduced into the formulation. As a consequence, there is couple-stress (moment stresses) tensor in addition to the classical force-stress tensor. These correspond to the local rotations/moments present due to the microstructure of a composite. These aspects of micropolar theory are appropriate for representing the local mechanics of fiber reinforced composites and cellular materials, which are studied in this thesis.

In literature, the challenge of micropolar theory has been two-fold: (1) the determination of the additional micropolar material constants that are introduced, and (2) the analytical and numerical implementation of finite micropolar theory. In the this thesis, physics based methods will be developed to determine the properties of fiber reinforced composites. In addition, the classical Hill-Mandel condition from classical micromechanics will be extended to a micropolar continuum to determine the constitutive relation of a structured cellular solid. Finite micropolar theory, which accounts for both geometric and material nonlinearities, is developed in this thesis. This is implemented via an updated Lagrangian finite element framework for analyzing fiber reinforced structures.

Micropolar theory is applied to boundary value problems where local rotations and moments are dominant. This includes problems where the wavelength of the deformation is comparable to the characteristic length of the microstructure. An example of this is the formation of localized deformation in fiber-reinforced composites (fiber kinking) under compression loading. Micropolar theory is not only a high fidelity model that helps to quantify the local moments and rotations, but it also prevents the loss of ellipticity of the governing equations at the onset of localization. This is useful for analyzing the post-peak response of fiber reinforced composites. The details regarding this are also explained in this thesis.

CHAPTER 1

Introduction

1.1 Motivation for Micropolar Theory

Continuum theories are concerned with the macroscopic behavior of a physical system containing large number of particles (electrons, atoms, ions, molecules, etc). A classical example of this is thermodynamic theory, which is the study of the kinematic behavior of particles in a given macroscopic system. Theoretically speaking, the direct approach of modeling can be done through a detailed, microscopic analysis of the individual motion of the constituents (micromechanics). The micromechanics approach could in principle yield accurate results, but due to the inherent large degrees of freedom, it is inefficient in terms of computational time, often beyond the capabilities of supercomputers. This is impractical for most engineering applications, where quick, back of the envelope estimations are preferred over detailed, accurate results. To overcome this, macroscopic, or continuum models are employed. However, these theories are phenomenological in nature, in that they are based on a small number of postulates, which relate measurable macroscopic quantities, independent to the hypothesis of the constituents at the microscale. These measurable quantities are in a sense averages over the individual particles. Now, instead of describing the system through the position and momentum of each particle, the continuum approach presents terminologies such as temperature, heat, density, stress, etc. In

such approaches, an incomplete description of the constituents is obtained, where the macroscopic behavior of the system is viewed "as through an opaque window." As seen in the schematic in Fig. 1.1, under the this approach, much of the information regarding the microstructure of the system is disregarded in favor of faster computation. The efficiency of the continuum models is in solving partial differential equations for the field functions, instead of a large number of coupled differential equations.

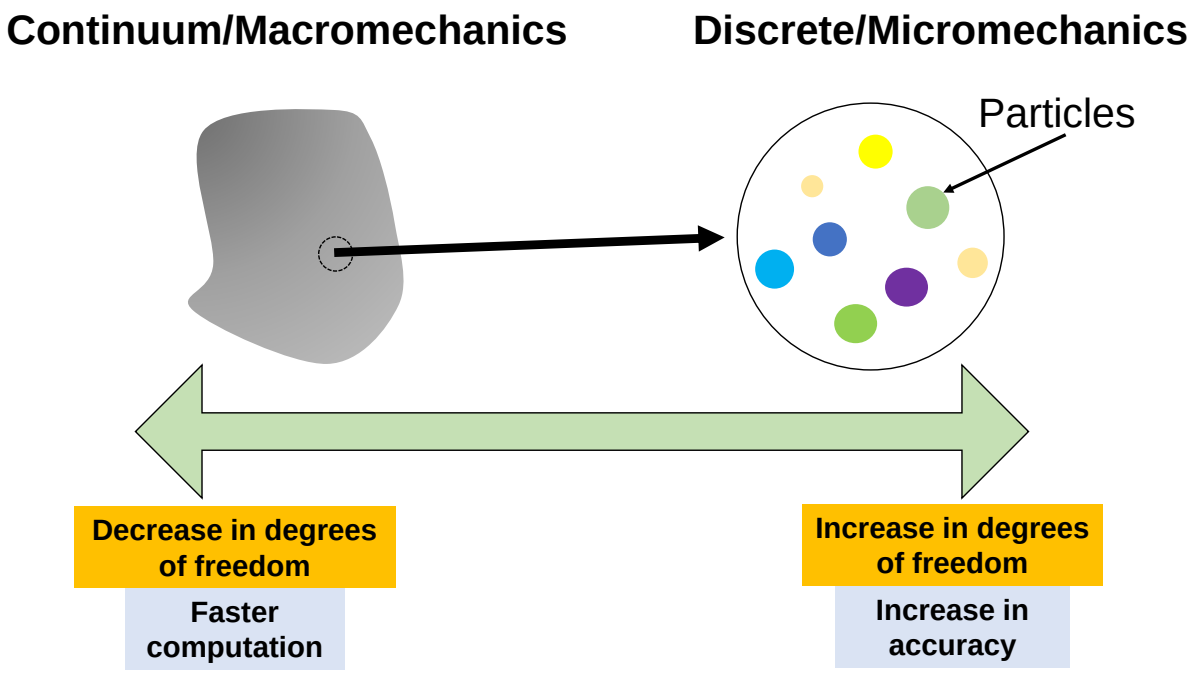

Figure 1.1: Continuum vs. discrete models.

For the continuum approach to be valid, the system must contain sufficient number of particles, or constituents N, inside a given volume ΔV, enclosed within a surface ΔS. Otherwise, the macroscopic field functions become dependent on the size of the system. As explained by Eringen in [1], an example of this is in the definition of the density of a material, which is defined

$$\rho = \lim_{\Delta V \to 0} \frac{m(\Delta V)}{\Delta V} \tag{1.1}$$

where for a given volume ΔV, $m(\Delta V)$ is the total mass enclosed inside it. As seen in the schematic in Fig. 1.2, the macroscopic function ρ is independent of volume size when $\Delta V > \Delta V_{cr}$. In this region, the classical (Cauchy) continuum assumptions are applicable, where the body is assumed to be composed of infinite number of particles of infinitesimal size. This allows for operations such as spatial differentiation across points in the volume. Next, considering an experiment, where density measurements are recorded by progressively taking smaller volume sizes, the density is seen to be strongly dependent on the volume size as $\Delta V \to 0$. This is because real materials are not continua, but are composed of particles of finite size, occupying a volume composed largely of empty space. As a result, continuum assumptions are no longer valid when $\Delta V << \Delta V_{cr}$. In this region, discrete, or micromechanics models are employed. It should be highlighted that the value of the critical volume ΔV_{cr} is dependent on the geometry and the properties of the constituents. In this thesis, the generalized, higher-order micropolar theory is discussed, which is applicable to the intermediate region $\Delta V < \Delta V_{cr}$. Unlike a Cauchy continuum, where the kinematics of a point is characterized by a displacement field, in a micropolar continuum, each point is assumed to have both displacement and an independent rotational degrees of freedom. This generalization treats each material point in the continuum as a rigid body particle of infinitesimal size. With the additional kinematic degrees of freedom, a length-scale parameter is naturally introduced in the continuum through the constitutive relation, which is associated with the characteristic length of the microstructure.

In addition, similar continuum approximations are used to model the macroscopic behavior of multiple continuum-phase heterogeneous media. This includes materials such as fiber reinforced composites, textiles, and cellular honeycomb structures, which have often found engineering applications as lightweight materials. Similar to the example demonstrated earlier, the direct modeling of these materials as an effective,

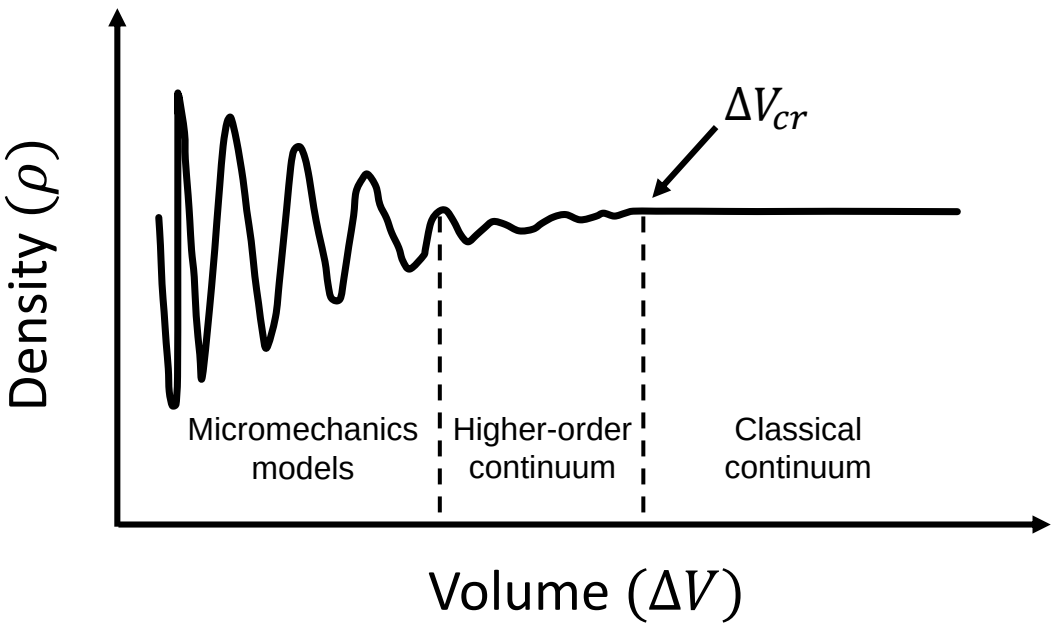

Figure 1.2: Example of a size effect in macroscopic density definition [1].

homogeneous continuum is dependent on the relations of the length scales of the problem. The validity of the continuum representation is governed by the principle of separation of scales, i.e. the macroscopic length of the domain is much larger than the mesoscopic characteristic length over which homogenization is carried out ($L_{macro} \gg L_{meso}$). In addition, the direct applicability of a Cauchy continuum is dependent on the size of the microstructure L_{micro} (average size of the fibers, grains, inclusion, etc.) relative to the length of the mesoscale. For example, considering a continuum in Fig. 1.3, the normal component of the traction at point P, on the surface associated with the normal $\boldsymbol{n}$ is defined,

$$t_n = \lim_{\Delta S \to 0} \frac{F_n(\Delta S)}{\Delta S} \tag{1.2}$$

In a Cauchy continuum, with the assumption that ΔS goes to zero, the force F_n acting along the normal direction becomes uniform. Thus, the gradients of F_n acting

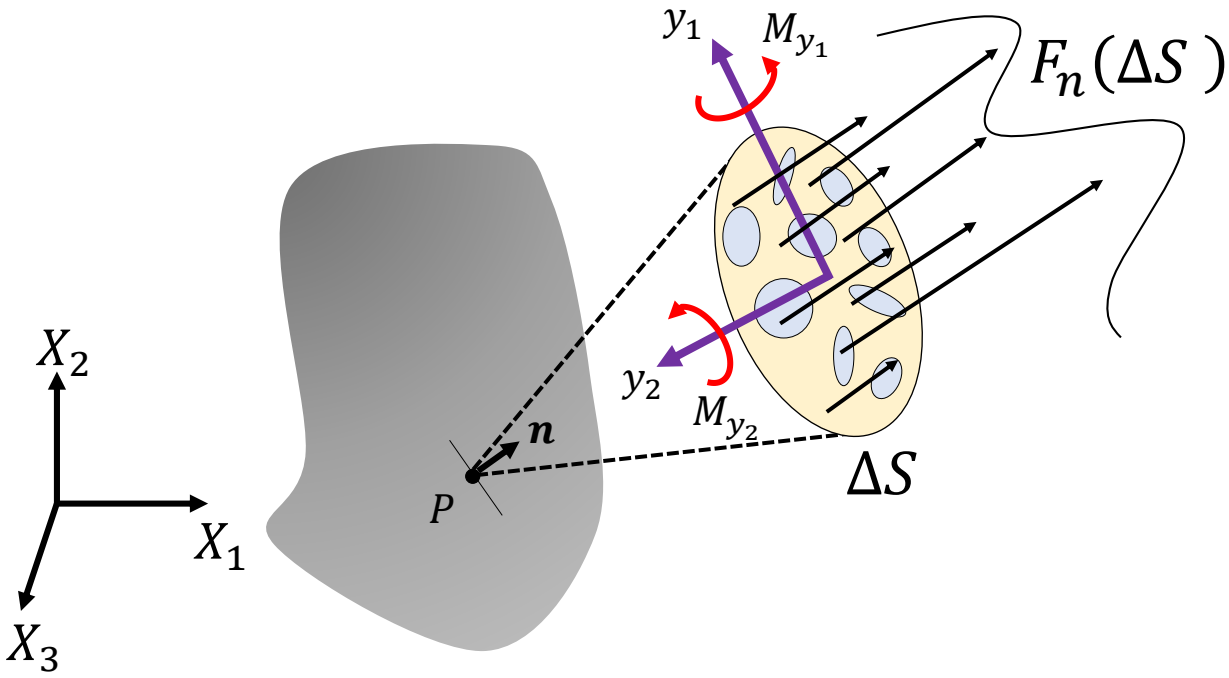

Figure 1.3: Introduction of surface moments in materials with a microstructure.

on the surface are neglected as it is independent of ΔS. However, considering the microstructure of the material, this limit is finite and bounded from below by the mesoscopic length, where the nonuniformity of the force F_n acting on the surface of a finite size ΔS induces moments,

$$M_{y_1} = \int_{\Delta S} y_2 dF_n \tag{1.3a}$$

$$M_{y_2} = \int_{\Delta S} y_1 dF_n \tag{1.3b}$$

from which couple-traction are defined by normalizing it by the surface area ΔS

$$Q_{y_1} = \lim_{\Delta S \to 0} \frac{M_{y_1}(\Delta S)}{\Delta S} \tag{1.4a}$$

$$Q_{y_2} = \lim_{\Delta S \to 0} \frac{M_{y_2}(\Delta S)}{\Delta S} \tag{1.4b}$$

Similarly, the presence of surface shear forces acting on ΔS induce a torsion M_n and

couple-traction Q_n. While in a general micropolar theory the continuum assumption is valid and the limits in Eqn. 1.2 and 1.4 are assumed to exist, the gradients induced because of the microstructure are introduced phenomenologically by the presence of the additional couple-traction. As a result, in addition to the force-stress tensor $\boldsymbol{\Sigma}$, which relates the surface traction $\boldsymbol{t}$ to the unit normal $\boldsymbol{n}$,

$$\boldsymbol{t} = \boldsymbol{\Sigma}^T \cdot \boldsymbol{n} \tag{1.5}$$

in a generalized micropolar continuum, an additional couple-stress tensor $\boldsymbol{M}$ is introduced, which relates couple-traction $\boldsymbol{Q}$ to the unit normal $\boldsymbol{n}$

$$\boldsymbol{Q} = \boldsymbol{M}^T \cdot \boldsymbol{n} \tag{1.6}$$

In a generalized micropolar continuum, the stresses and couple-stresses are shown on a 2D volume element in Fig. 1.4. In the absence of body forces and inertia effects,

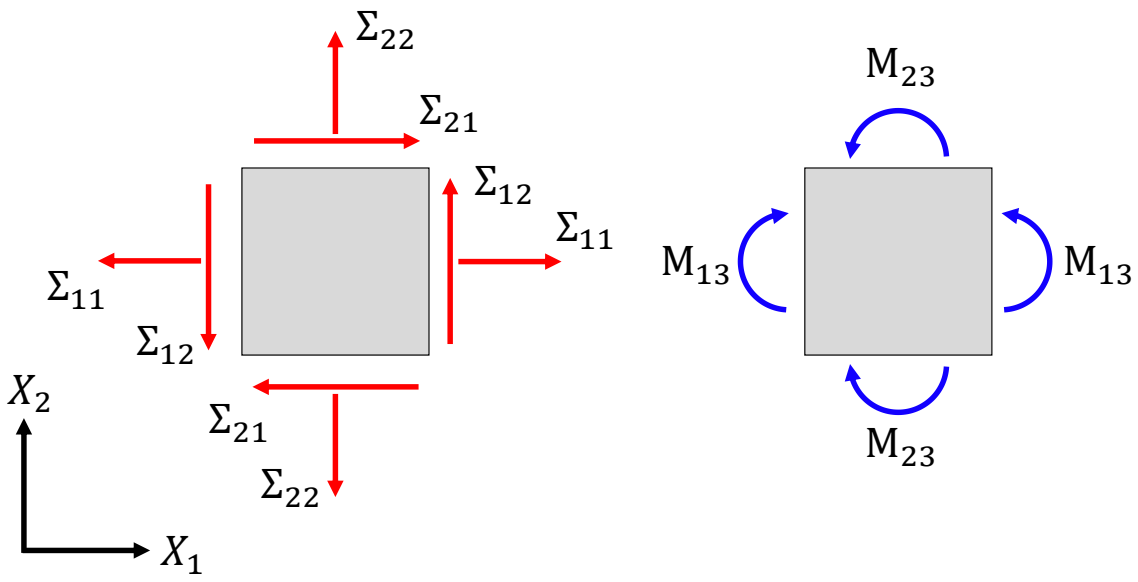

Figure 1.4: 2D micropolar volume element with asymmetric stresses Σ_{ij} and couple-stresses M_{i3}.

the force and moment equilibrium equations are

$$\Sigma_{11,1} + \Sigma_{21,2} = 0 \tag{1.7a}$$

$$\Sigma_{12,1} + \Sigma_{22,2} = 0 \tag{1.7b}$$

$$M_{13,1}+M_{23,2} + \Sigma_{12} - \Sigma_{21} = 0 \tag{1.7c}$$

It should be highlighted that the presence of couple-stresses M_{13} and M_{23} in the moment equilibrium equation (Eqn. 1.7c) results in the stress tensor to be asymmetric ($\Sigma_{12} \neq \Sigma_{21}$, or in general $\Sigma_{ij} \neq \Sigma_{ji}$). In classical elasticity, the symmetry of the stress tensor is a consequence of the absence of the couple stresses.

The kinematical difference between a micropolar continuum, compared to a Cauchy continuum, is in the additional rotational degree of freedom φ_i, which is independent of the displacement field ($\varphi_i \neq \frac{1}{2}\varepsilon_{ikj}u_{j,k}$). Thus, the field equations of micropolar theory are characterised by the displacement and rotational vectors $\boldsymbol{u} = (u_1, u_2, u_3)$ and $\boldsymbol{\varphi} = (\varphi_1, \varphi_2, \varphi_3)$, respectively. In the case of 2D planar deformation, the nonzero kinematic functions are $u_1(x_1, x_2)$, $u_2(x_1, x_2)$, and $\varphi_3(x_1, x_2)$. As shown in Fig. 1.5, the deformation of a micropolar volume element in a 2D space is analogous to a rigid body motion. Initially at position $\boldsymbol{r} = (X_1, X_2)$, it is characterized by the displacement vector $\boldsymbol{u} = (u_1, u_2)$ and an independent rotation φ_3.

The strains associated with these kinematics are

$$\Gamma_{ij} = u_{j,i} - \varepsilon_{ij3}\varphi_3 \tag{1.8a}$$

$$K_{i3} = \frac{\partial \varphi_3}{\partial x_i} \tag{1.8b}$$

for $i = 1, 2$. Γ_{ij} is referred to as the asymmetric strain tensor, ε_{ij3} is the Levi-Civita third-order tensor, and K_{i3} is the additional micropolar curvature strain. Unlike in a Cauchy continuum, the strain Γ_{ij} is no longer symmetric ($\Gamma_{ij} \neq \Gamma_{ji}$). In the

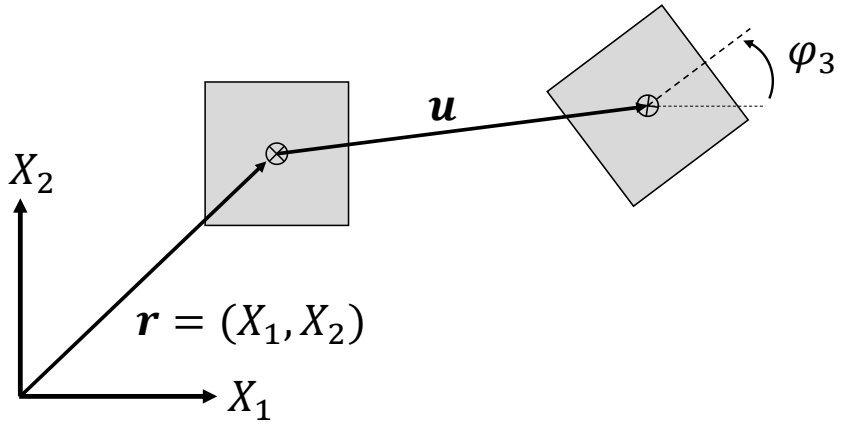

Figure 1.5: Kinematics of a 2D micropolar volume element.

expression of the strain energy, these strains are work conjugate to the stresses Σ_{ij} and M_{i3}, respectively

$$U = \frac{1}{2}\int_V (\Sigma_{ij}\Gamma_{ij})dV + \frac{1}{2}\int_V (M_{i3}K_{i3})dV \tag{1.9}$$

The corresponding constitutive relations between the stresses and the strains are,

$$\Sigma_{ij} = \mathbb{C}_{ijkl}\Gamma_{kl} \tag{1.10a}$$

$$M_{i3} = \mathbb{D}_{i3k3}K_{k3} \tag{1.10b}$$

where $\mathbb{C}_{ijkl}$ and $\mathbb{D}_{i3k3}$ are the two stiffness tensors. They posses a major symmetry, or

$$\mathbb{C}_{ijkl} = \mathbb{C}_{klij} \tag{1.11a}$$

$$\mathbb{D}_{i3k3} = \mathbb{D}_{k3i3} \tag{1.11b}$$

However, due to the asymmetry of the stress and strain tensors mentioned above, the

minor symmetry is no longer satisfied

$$\mathbb{C}_{ijkl} \neq \mathbb{C}_{jikl} \tag{1.12a}$$

$$\mathbb{C}_{ijkl} \neq \mathbb{C}_{ijlk} \tag{1.12b}$$

$$\mathbb{D}_{i3k3} \neq \mathbb{D}_{3ik3} \tag{1.12c}$$

$$\mathbb{D}_{i3k3} \neq \mathbb{D}_{i33k} \tag{1.12d}$$

For a 2D, isotropic micropolar medium, these tensors can be alternatively expressed as

$$\mathbb{C}_{ijkl} = (\mu - k)\delta_{jk}\delta_{il} + (\mu + k)\delta_{jl}\delta_{ik} + \lambda\delta_{ij}\delta_{kl} \tag{1.13a}$$

$$\mathbb{D}_{i3k3} = \gamma\delta_{ik} \tag{1.13b}$$

The material constants λ, μ correspond to the Lamé constants of classical elasticity, while k, γ are the additional micropolar constants. It should be noted, in the general 3D isotropic micropolar elasticity, 6 independent material constants are present. In order to reduce the number of material constants introduced in the formulation, the 2D simplification will be considered throughout this thesis.

In summary, the general micropolar theory introduces

- a couple-stress tensor in addition to the force-stress tensor in a Cauchy continuum,
- the stress and strain tensors are asymmetric (not symmetric),
- there are additional material constants associated with the higher order micropolar theory,
- and 2D planar micropolar theory has less micropolar material constants than the corresponding general 3D theory, which will motivate us to consider 2D

analysis for simplicity.

For reference, the complete description regarding the derivation of linear micropolar theory can be found in [1]. Some analytical results pertaining to the solution of a boundary value problem can be found in [5], [6], and [7] for the classical plate with an inclusion problem. For example, it was concluded that the stress concentration factor of a micropolar plate with a hole is below the prediction of classical elasticity. However, such analytical solutions in the linear regime often conclude the micropolar effects to be small and experimentally undetectable. Because of this, in the following thesis, we are interested in extending micropolar theory to nonlinear problems. In particular, we focus on phenomenon where the macroscopic characteristic length (such as the deformation length) of the problem is comparable with the size of the microstructure of the material. A classical example is localized deformation observed in composite materials.

1.2 Localization Phenomenon

Materials with microstructure can form intense bands of deformation, also called localization or shear banding, when under compressive loading. This is characterized by the formation of at least one narrow region in a material, where upon further continued loading, the deformation is limited inside these regions. This phenomenon has been subjected to research since the early 1900's. It has been experimentally observed in various classes of materials with a microstructure, some of which include geological materials such as granular media [8], [9] and metals [10]. Understanding how localization occurs is important for predicting the integrity of a structure, as it can lead to failure. For example, in the case of granular materials, it is crucial for civil engineering applications, and in ductile metals, the formation of the localized deformation (commonly called shear bands) is proceeded by fracture. Similarly, it

has also been observed in fiber reinforced composites (fiber kinking) and honeycomb structures (cell row collapse).

Although micromechanics models are capable of capturing this form of instability through a detailed modeling of the microstructure, due to the increase in computational time, such an approach is impractical. In literature, macromechanics methods have been discussed to characterize localization through a continuum approach [11], [12], [13]. In these models, the continuous material initially undergoes a homogeneous deformation (Fig. 1.6a), until a critical load is reached, upon which the deformation is confined to a finite region (Fig. 1.6b).

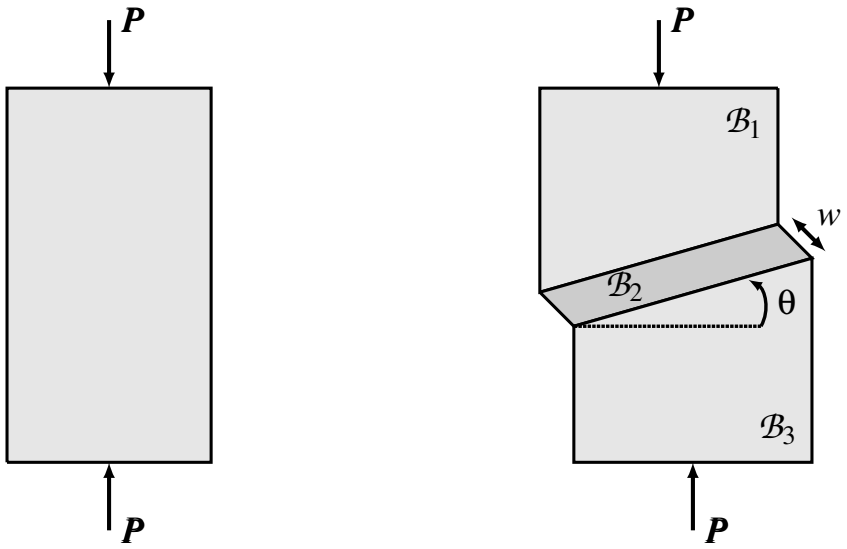

(a) Homogenous deformation (b) Localization

Figure 1.6: Formation of a localized deformation, or shear band, observed in materials with microstructure.

From a mathematical point of view, in Fig. 1.6b, the domain in two-dimensional space $\mathcal{B} \subset \mathbb{R}^2$ is now represented by three subdomains ($\mathcal{B} = \mathcal{B}_1 \bigcup \mathcal{B}_2 \bigcup \mathcal{B}_3$). The displacement field is seen to be continuous throughout the whole domain ($\mathcal{B}$), however, the gradients (strains) are discontinuous at the boundaries where the subdomains intersect.

As clearly outlined by [14], such discontinuities are a characteristic of hyperbolic partial differential equations. However, the governing equations of an initially elastic body in an equilibrium problem are elliptical, where such discontinuities are not permitted. As a result, these phenomena are associated with the loss of ellipticity of the governing equations due to nonlinearities. As discussed in detail in [15], in classical continuum theories, this transition violates the stability criterion of the constitutive relationship, in that it has to be positive definite. This violation leads to numerical mesh dependency due to the ill-posedness of the problem at the onset of localization. In addition, the predictions of the localization width w and angle θ are incorrect, with the localization width having an infinitesimal thickness ($w = 0$). In real materials, the width is finite and comparable to the characteristic size of the microstructure.

Currently, there are numerous ways of overcoming this issue by preventing a loss in ellipticity at the onset of localization. These approaches are outlined in [16], [17], [18]. These include methods such as the introduction of viscoplasticity, or by considering higher order gradients in the strain energy density. An alternative approach is through higher order continuum theories such as micropolar theory, which is adopted in this thesis. This approach increases the order of the Laplacian of the governing equations by introducing an internal length scale parameter, which in turn prevents a loss in ellipticity. The corresponding equations are well-posed at the onset of localization.

The formation of localization is commonly observed in fiber reinforced composite (Fig. 1.7a). It is also referred to as fiber kinking. This is developed when fiber reinforced composites are compressed in the directions of the fibers, and upon reaching a critical value, the fibers undergo localized kink banding inside a finite region of the material. The study of kinking was first initiated by [19], [20], who provided simple formulas for the compressive strength. However, later studies by [21], [22], [23], [24], etc. showed the importance of matrix material nonlinearity and initial fiber misalignment, in addition to geometric nonlinearity, for predicting kinking. A

review in [25] and [26] outline the mechanism for kinking as being caused by the continuous reduction of the shear stiffness of the matrix material in tandem with fiber misalignment that leads to continuously increasing microscopic fiber rotations, which evolve and increase local shear strains leading to a further reduction in shear stiffness, ultimately culminating in a limit load type instability, leading to kink banding. A snap-back is observed in the corresponding macroscopic stress-strain response.

Localized deformation zones are also found in polymeric cellular materials [27]. For example, this is shown for a hexagonally packed circular honeycomb structure in Fig. 1.7b. Under compression loading, at the microscale, local buckling of the cell walls are observed. However, macroscopically, this phenomenon can be viewed as a weak discontinuity, in that the macroscopic displacements are continuous, but their derivatives are discontinuous. Discussed in [28], this phenomenon is also governed by imperfections of the cell walls and cell shapes, along with local geometric and material nonlinearities. Early discussion of attempts to characterize this phenomenon at the continuum scale was mentioned in [29], however significant results have not been presented.

1.3 Research Objective and Thesis Outline

Although micropolar theory has a long history of development, there are underlying challenges which have not been sufficiently addressed in literature, which prevent it from further engineering applications. These include (1) the determination of the additional micropolar material constants, and (2) the extension of the theory in the nonlinear regime (both geometric and physical). This thesis attempts to address these issues. It is divided in six chapters, in which approaches are proposed for modeling fiber reinforced composites and cellular honeycomb structures. The material presented has been published in the open literature.

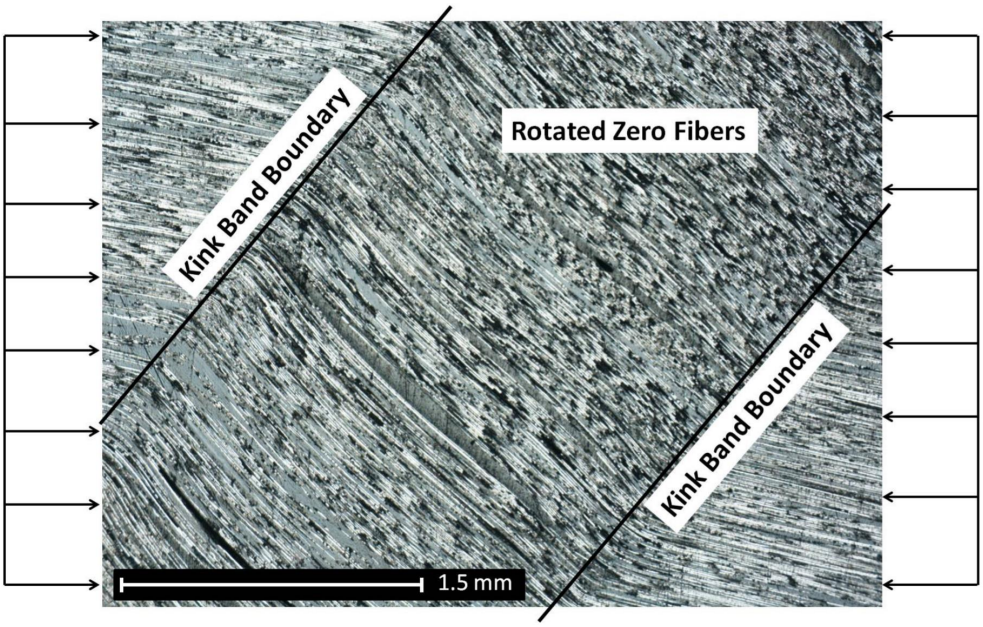

(a) Fiber kinking [30]

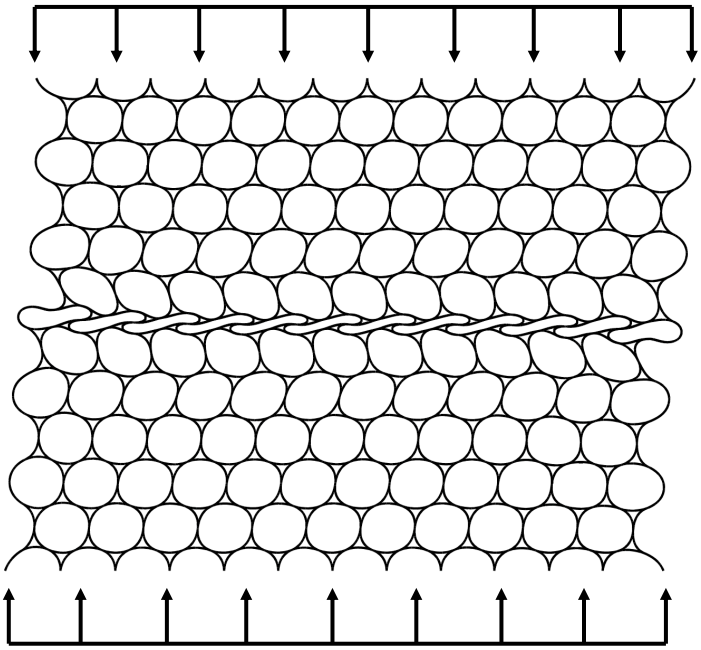

(b) Honeycomb cell buckling

Figure 1.7: Localized deformation in fiber reinforced and honeycomb composites.

In Chapter 1, the motivation for the higher order micropolar theory was discussed. The governing equations of a 2D linear medium was outlined to summarize the additional features of the theory.

In Chapter 2, a nonlinear, anisotropic micropolar theory is developed for analyzing fiber reinforced composites. Both geometric and physical nonlinearities are considered. The material nonlinearity is based on classical elastoplasticity, with an anisotropic yield criterion. The derivation of the theory and the definition of the anisotropic constitutive relationship based on a micropolar objective stress rate measure is given. Using an updated Lagrangian formulation, a nonlinear finite element code is written and implemented in a fortran based user element (UEL) subroutine for analyzing localization phenomenon in fiber reinforced composites (fiber kinking) using the commercial finite element software ABAQUS. The effects of the additional material parameters on the localization features (angle and width) are studied. In addition, it is shown that localization can be induced through the consideration of geometric and physical nonlinearity, coupled with an initial geometric imperfection. This is in contrast to previous studies on the subject, where a softening relation is introduced in the constitutive model, which is in violation of Drucker criterion for a stable continuous nonlinear medium. This work is based on the journal paper, [31].

In Chapter 3, a method for determining the micropolar material constants of a fiber reinforced composite is proposed. Based on physics-based numerical tests, physical meaning is assigned to the additional material parameters. These are used for comparing the continuum predictions of fiber kinking to an exact micromechanics model. The corresponding journal paper is [32].

In Chapter 4, the constitutive relation of structured cellular solids is determined. These include a hexagonally packed circular honeycomb, regular hexagonal honeycomb, and a grid structure. These recently proposed homogenization techniques are based on classical volume averaging methods and are applicable uniquely to cellular

media, as discussed in the thesis and also in the journal paper, [33].

In Chapter 5, the geometrically exact finite micropolar theory, with finite strain and curvature is discussed. In this chapter, the issues of the general nonlinear theory are discussed, along with the complications associated with the trigonometric strain/curvature and displacement/rotation relation. Because of the limited analytical solutions in this area, a closed form solution is obtained for a buckling of a micropolar strip of medium under compressive loading. In addition, 1D micropolar beam theory is also developed, as shown in the journal paper, [34].

Chapter 6, provides a summary and recommendations for future work, based on the findings reported in this thesis.

1.4 Contribution of Thesis

In this section, the novel contributions of this thesis are highlighted. In chapter 2, geometric and material nonlinear micropolar theory is developed for transversely-isotropic medium. The geometric nonlinearity is quasi-nonlinear, with the nonlinearity presented in the Green-Lagrange strain only (but linear in curvature), as seen in Eqn. 2.62. This simplification avoids the complications of the general finite micropolar theory. It is noted that, starting with the general finite micropolar theory, it is not possible to reduce results to the classical theory. These issues are highlighted in Chapter 5.

In chapter 2, material nonlinearity is implemented under the assumptions of elastoplasticity. A new phenomenological anisotropic micropolar yield function is introduced for the first time, which is a function of couple-stresses in addition to force-stresses. This is a generalization of the classical Hill criterion for anisotropic medium. In addition, the treatment of micropolar objective stress rates is discussed for defining the constitutive relationship.

The theoretical model is implemented in an updated Lagrangian nonlinear finite element code. For numerical analysis, a new quadrilateral element is introduced, with each node having both displacement and an independent rotational degree of freedom. In order to implement this for analysis, a fortran based user element subroutine (UEL) is developed and the commercial software ABAQUS is used for visualization. Although these are discussed for a fiber reinforced composites, it can be applied to any transversely-isotropic micropolar medium.

To determine the effective micropolar material constants of fiber reinforced composites, new physics based micromechanics tests are introduced in chapter 3. The moment-curvature relation is defined through the extension of the concentric cylinder model (CCM) and the additional shear properties are determined through newly proposed simple shear tests.

In chapters 2 and 3, the simulation of localization, or fiber kinking is discussed. In chapter 2, the effects of the additional micropolar material constants is analyzed, while in chapter 3, a comparison with a micromechanics model is made for verification of the theory. Unlike most studies in literature on localization, in this thesis, a local material softening relation is not introduced into the constitutive relation to induce a maximum load. Instead, a limit load type response is shown to be induced by geometric and material nonlinearity, coupled with fiber misalignment.

In Chapter 4, closed form solutions for the material constants of 2D honeycomb structures are reported, which are obtained through nondimensional analysis.

In Chapter 5, the general finite micropolar theory is discussed. The general theory is then applied to obtain the closed form analytical solution for the buckling load of a micropolar strip. In addition, micropolar beam theory is developed based on the general equations.

CHAPTER 2

Localization in Anisotropic Elastoplastic Micropolar Media: Application to Fiber Reinforced Composites

2.1 Introduction

In the recent decades, fiber reinforced composites have been applied to various industrial applications, most notably in the aerospace industry as lightweight material. Despite the plethora of their applications, they are still limited in use because of our limited ability to accurately predict their mechanical behavior. To overcome this, a high fidelity nonlinear micropolar model, which includes fiber rotation, curvature, and bending in the continuum formulation, is proposed.

In this section, an anisotropic elastoplastic constitutive model is formulated for fiber reinforced composites, undergoing large geometric deformation. The composite material is modeled as a micropolar continuum, which unlike a classical or a Cauchy continuum, it takes into account the higher order fiber bending and twisting modes of deformation. In micropolar theory, the rotational degree of freedom is independent of the displacement field. This is utilized to express the microrotation tensor that represents the rotation of the fibers, or the direction of anisotropy in a continuum. In literature, numerous anisotropic yield critera have been developed and extensively

used for these materials [35]. In the following formulation, we propose an anisotropic micropolar yield criterion by extending the Hill's criterion in classical elastoplasticity and including couple-stresses in the potential function. In this chapter, the details of the geometric and material nonlinear theoretical model is derived. The corresponding updated Lagrangian (UL) finite element formulation is discussed. In the past, micropolar theory has been successfully applied to problems associated with localized deformation, where classical theories fail to capture this phenomenon due to the loss of ellipticity of the governing equations. These previous analysis have been done on isotropic micropolar medium, and in order to initiate the onset of localization, a softening relationship between the equivalent stress and strain has been introduced. Since the introduction of material softening in the constitutive relation has been a topic of contention in the field of continuum mechanics, it is shown to be unnecessary. Instead it is induced by geometric and material nonlinearity, along with a global geometric imperfection that introduces axial-shear coupling. In fiber reinforced composites, localization occurring from compression loading is representative of fiber kinking, which is associated with a snap-back behavior in the macroscopic stress-strain response. At the end of the chapter, we seek to simulate the this response numerically and study the effects of the additional micropolar material constants on the global stress-strain response and the features of the localized deformation, such as localization width and angle.

Some notable works in this area include [36], where by studying fiber kinking, it was shown that the governing equations correspond to the micropolar equations. In addition, a continuum model for fiber-reinforced composites, with fiber bending and twisting effects included, was discussed by Steigmann in [37]. More recently, this has been extended to derive the general nonlinear continuum equations of fiber composites based on the assumption that the fibers behave as Kirchhoff type rods [38].

2.2 Formulation of Nonlinear Micropolar Theory

A continuum body in its undeformed state occupies a set of material points in an Euclidean space ${}^0\mathcal{B} \subset \mathbb{R}^3$. It has a volume ${}^0V$ and a boundary ${}^0S$. The coordinates of the material points of ${}^0\mathcal{B} = {}^0V \bigcup {}^0S$ are represented by $\boldsymbol{X} \in {}^0\mathcal{B}$. Under a set of externally applied loads, the material points in the undeformed state deform in their spatial position, with the new configuration n now occupying a volume ${}^nV$ and a boundary ${}^nS$. The coordinates of the spatial points ${}^n\mathcal{B} = {}^nV \bigcup {}^nS$ are represented by $\boldsymbol{x} \in {}^n\mathcal{B}$. The position of the body at these two configurations are related by the displacement $\boldsymbol{u}$.

$$\boldsymbol{x} = \boldsymbol{X} + \boldsymbol{u} \tag{2.1}$$

In addition, an infinitesimal line element in the reference frame $d\boldsymbol{X} \in {}^0\mathcal{B}$ is related to its spatial configuration $d\boldsymbol{x} \in {}^n\mathcal{B}$ by

$$d\boldsymbol{x} = \boldsymbol{F} \cdot d\boldsymbol{X} \tag{2.2}$$

where

$$\boldsymbol{F} = \frac{\partial \boldsymbol{x}}{\partial \boldsymbol{X}} \tag{2.3}$$

is called the deformation gradient. In order to ensure an admissible deformation between the reference and the spatial configuration, $0 < J = \det(\boldsymbol{F}) < \infty$ condition must be satisfied. An alternative form of the tensor $\boldsymbol{F}$ is in terms of a multiple of two tensors

$$\boldsymbol{F} = \boldsymbol{R} \cdot \boldsymbol{U} \tag{2.4}$$

In a micropolar continuum, $\boldsymbol{R}$ represents an independent microrotation tensor and $\boldsymbol{U}$ is the micropolar stretch tensor, indicating the rigid body rotation and stretch of an arbitrary line element $d\boldsymbol{X}$, respectively. The micropolar stretch tensor is unsymmetric ($\boldsymbol{U} \neq \boldsymbol{U}^T$) and the microrotation tensor is represented by an orthogonal 3D

rotational group ($\boldsymbol{R} \in SO(3)$). In a Cauchy continuum, where the rotation field is dependent on the displacement field ($\varphi = \frac{1}{2}\nabla \times \boldsymbol{u}$), Eqn. 2.4 corresponds to the polar decomposition of the deformation gradient in terms of its orthogonal rotation matrix and the symmetric stretch tensor.

In micropolar theory, the microrotation tensor $\boldsymbol{R}$ is represented in terms of $SO(3)$ exponential mapping

$$\boldsymbol{R} = e^{\boldsymbol{\Phi}(\boldsymbol{\varphi})} = \sum_{n=1}^{\infty} \frac{\boldsymbol{\Phi}^n(\boldsymbol{\varphi})}{n!} \tag{2.5}$$

Considering that a line element in a micropolar continuum is rotating about the axis of rotation of $\boldsymbol{\varphi}$ (Fig. 2.1), the exponential mapping can be simplified according to Rodrigues' rotation formula

$$\boldsymbol{R} = \boldsymbol{I} + \frac{\sin(\theta)}{\theta}\boldsymbol{\Phi}(\boldsymbol{\varphi}) + \frac{1-\cos(\theta)}{\theta^2}\boldsymbol{\Phi}^2(\boldsymbol{\varphi}) \tag{2.6}$$

where $\boldsymbol{\Phi} = -\boldsymbol{\Phi}^T$ is a skew-symmetric tensor of the microrotational vector $\boldsymbol{\varphi}$

$$\boldsymbol{\Phi} = \begin{bmatrix} 0 & -\varphi_3 & \varphi_2 \\ \varphi_3 & 0 & -\varphi_1 \\ -\varphi_2 & \varphi_1 & 0 \end{bmatrix} \tag{2.7}$$

and θ is the magnitude of $\boldsymbol{\varphi}$

$$\theta = |\boldsymbol{\varphi}| = \sqrt{\varphi_1^2 + \varphi_2^2 + \varphi_3^2} \tag{2.8}$$

For example, given an arbitrary vector $\boldsymbol{r}$ in the continuum, under a rigid body rotation $\boldsymbol{R}$, it transforms into $\hat{\boldsymbol{r}}$ ($\hat{\boldsymbol{r}} = \boldsymbol{R} \cdot \boldsymbol{r}$) as shown in Fig. 2.1. In the particular case when the rotational axis corresponds to the basis vector $\boldsymbol{g}_3$, Rodrigues' rotational

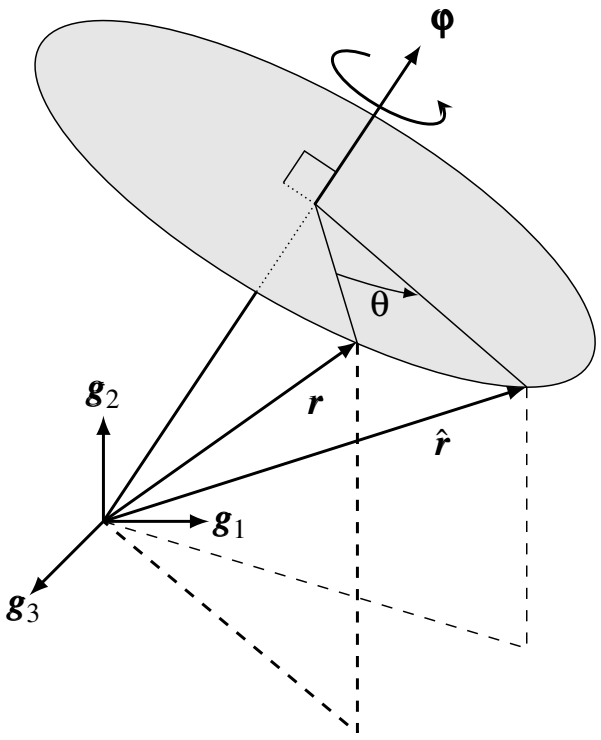

Figure 2.1: Rotation of an arbitrary vector $\boldsymbol{r}$ under microrotational tensor $\boldsymbol{R} \in SO(3)$.

formula reduces into the well known form,

$$\boldsymbol{R}(\boldsymbol{\varphi}) = \begin{bmatrix} \cos(\theta) & -\sin(\theta) & 0 \\ \sin(\theta) & \cos(\theta) & 0 \\ 0 & 0 & 1 \end{bmatrix} \tag{2.9}$$

In our formulation, we consider an arbitrary continuum body ${}^0\mathcal{B}$ at its reference state, with its microstructure composed of reinforced fibers. At each material point $\boldsymbol{X}$, an orthonormal triad of base vectors $\boldsymbol{g}_i$ is assumed to be attached to it, such that $\boldsymbol{g}_1$ is locally aligned along the fiber direction. By assuming the body is deforming under finite local rotation, but small relative straining (isochoric plastic deformation), the triad of base vectors in ${}^n\mathcal{B}$ are $\hat{\boldsymbol{g}}_i$, which remain orthonormal and attached to point $\boldsymbol{x}$, such that $\hat{\boldsymbol{g}}_1$ is aligned along the fiber direction. It is assumed that these base

vectors undergo a rigid body rotation under the microrotation tensors (Fig. 2.2)

$$\hat{\boldsymbol{g}}_i = \boldsymbol{R} \cdot \boldsymbol{g}_i \tag{2.10}$$

As seen in Fig. 2.2b, when the body deforms, the fibers at the microscale bend and twist locally. In a continuum modeling of fiber reinforced composites, the classical Cauchy continuum is unable to capture the kinematics and kinetics associated with these higher order modes of deformation. However, in a micropolar continuum, these local fiber bending and twisting effects are introduced by considering a micropolar volume element, where in addition to the stresses, couple-stresses are also assumed to be transferred from one volume element to the next, as shown in Fig. 2.3. The strain energy that takes in account these higher order deformation modes is defined as,

$$U = \frac{1}{2}\int_{{}^nV} (\boldsymbol{\Sigma} : \boldsymbol{\Gamma}) d^nV + \frac{1}{2}\int_{{}^nV} (\boldsymbol{M} : \boldsymbol{K}) d^nV \tag{2.11}$$

where $\boldsymbol{M}$ is the asymmetric Cauchy, or true couple-stress (moment per area) and its work conjugate asymmetric curvature strain is $\boldsymbol{K}$. When considering these additional stresses and strains, in order for the micropolar volume element in Fig. 2.3 to be in a moment equilibrium, the classical, or true stress tensor $\boldsymbol{\Sigma}$ and its conjugate strain tensor $\boldsymbol{\Gamma}$ are no longer symmetric ($\boldsymbol{\Sigma} \neq \boldsymbol{\Sigma}^T$ and $\boldsymbol{\Gamma} \neq \boldsymbol{\Gamma}^T$). In the absence of dynamic effects, the linear and angular equilibrium equations are,

$$\nabla \cdot \boldsymbol{\Sigma} + \boldsymbol{f}^B = 0 \quad \text{or} \quad \Sigma_{ji,j} + f_i^B = 0 \tag{2.12a}$$

$$\nabla \cdot \boldsymbol{M} + \boldsymbol{\varepsilon} : \boldsymbol{\Sigma} + \boldsymbol{C}^B = 0 \quad \text{or} \quad M_{ji,j} + \varepsilon_{ijk}\Sigma_{jk} + C_i^B = 0 \tag{2.12b}$$

respectively. The derivatives and the gradients are taken with respect to the spatial coordinates and $\boldsymbol{f}^B$ and $\boldsymbol{C}^B$ are the external body force and body couple. ε_{ijk} is the Levi-Civita third-order tensor. In addition, to complement Eqns. 2.12, the surface of

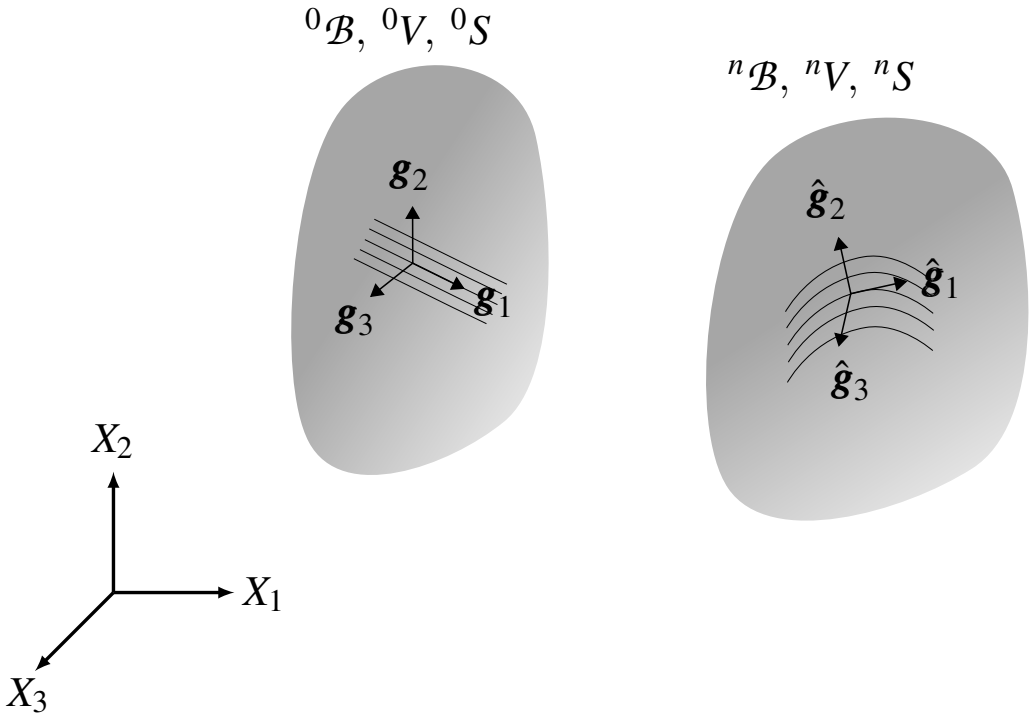

(a) Homogenous continuum at the macroscale

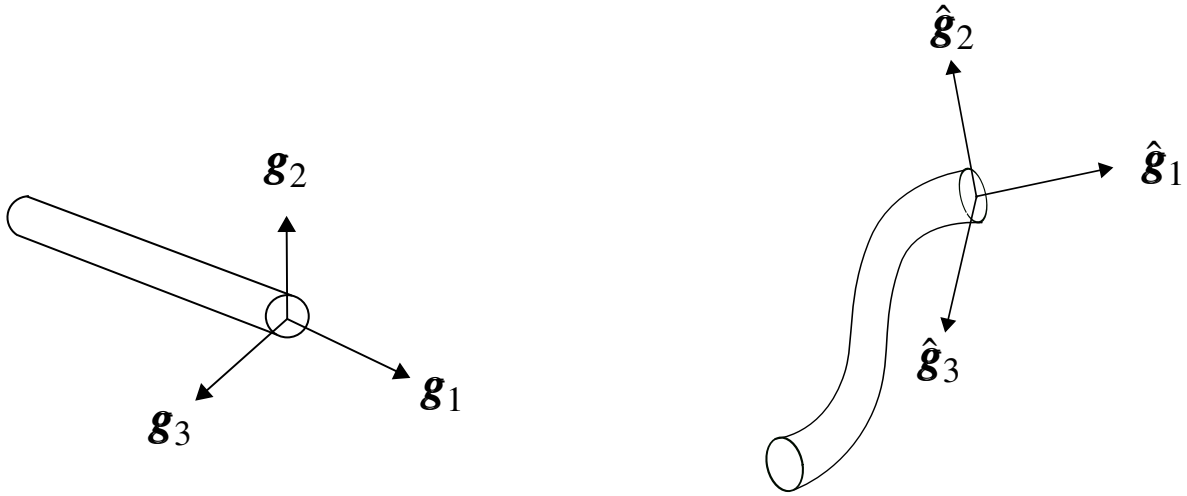

(b) Fiber bending and twisting at the microscale

Figure 2.2: Deformation of a fiber reinforced composite.

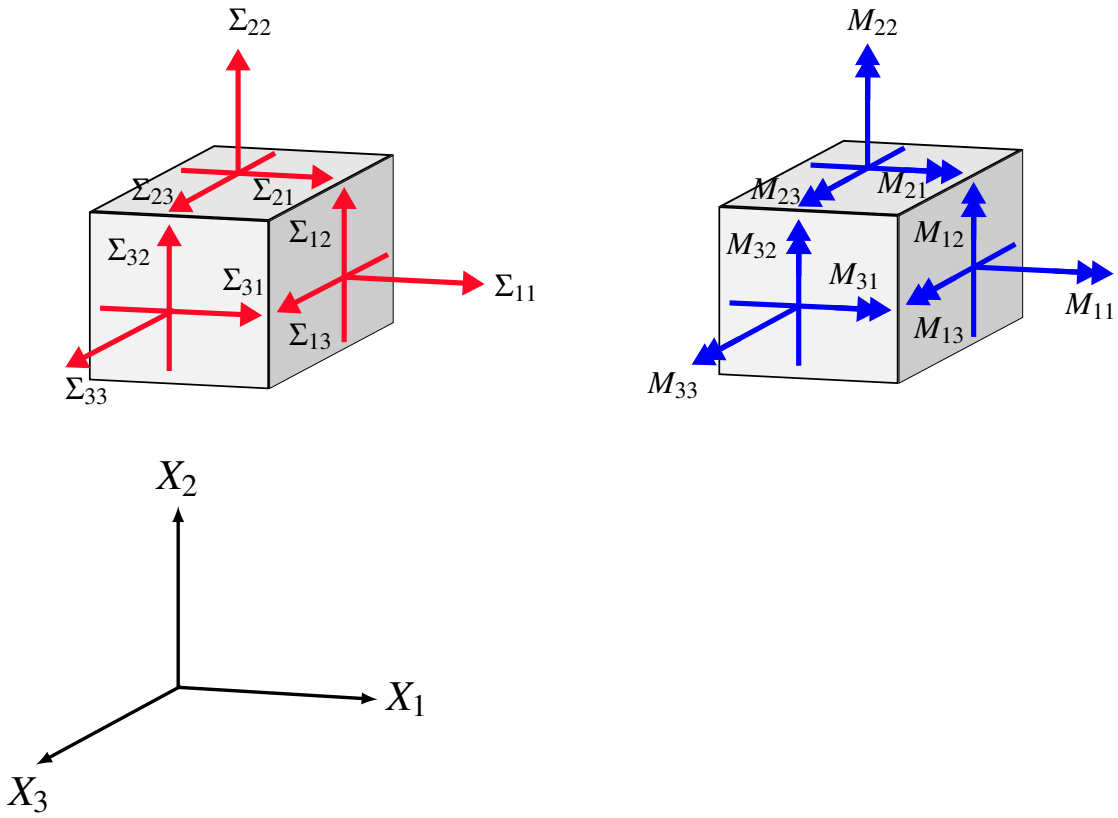

Figure 2.3: Micropolar continuum volume element with asymmetric stresses $\boldsymbol{\Sigma}$ and couple-stresses $\boldsymbol{M}$.

the body can be divided in two parts from the viewpoint of boundary conditions: the part ${}^nS_1$ over which boundary conditions are prescribed in terms of traction ($\boldsymbol{t}$) and couple-traction ($\boldsymbol{Q}$), and the part ${}^nS_2$ over which boundary conditions are prescribed in terms of displacements ($\boldsymbol{u}$) and rotations ($\boldsymbol{\varphi}$) (${}^nS = {}^nS_1 \bigcup {}^nS_2$). On ${}^nS_1$,

$$\boldsymbol{t} = \boldsymbol{\Sigma}^T \cdot \boldsymbol{n} \quad \text{and} \quad \boldsymbol{Q} = \boldsymbol{M}^T \cdot \boldsymbol{n} \tag{2.13}$$

where $\boldsymbol{n}$ denotes the normal to surface at $\boldsymbol{x} \in {}^nS_1$.

The corresponding linear strains are defined as

$$\boldsymbol{\Gamma} = (\nabla \boldsymbol{u})^T + \boldsymbol{\Phi} \quad \text{or} \quad \Gamma_{ij} = u_{j,i} - \varepsilon_{ijk}\varphi_k \tag{2.14a}$$

$$\boldsymbol{K} = (\nabla \boldsymbol{\varphi})^T \quad \text{or} \quad K_{ij} = \varphi_{j,i} \tag{2.14b}$$

where $\boldsymbol{\Gamma}$ and $\boldsymbol{K}$ are called the asymmetric micropolar strain and curvature tensors, respectively. The linear elastic anisotropic constitutive equations, relating the strains to the stresses are

$$\hat{\boldsymbol{\Sigma}} = \hat{\mathbb{C}} : \hat{\boldsymbol{\Gamma}} \quad \text{or} \quad \hat{\Sigma}_{ij} = \hat{\mathbb{C}}_{ijkl}\hat{\Gamma}_{kl} \tag{2.15a}$$

$$\hat{\boldsymbol{M}} = \hat{\mathbb{D}} : \hat{\boldsymbol{K}} \quad \text{or} \quad \hat{M}_{ij} = \hat{\mathbb{D}}_{ijkl}\hat{K}_{kl} \tag{2.15b}$$

where $\hat{(\,)}$ indicates the stresses, the strains, and the material properties are defined in the fiber-aligned coordinate system $\hat{\boldsymbol{g}}_i$. Due to the existence of U, these fourth order stiffness tensors possess major symmetry,

$$\hat{\mathbb{C}}_{ijkl} = \hat{\mathbb{C}}_{klij} \tag{2.16a}$$

$$\hat{\mathbb{D}}_{ijkl} = \hat{\mathbb{D}}_{klij} \tag{2.16b}$$

However, due to the asymmetry in the stresses and strains, the minor symmetry is no longer satisfied

$$\hat{\mathbb{C}}_{ijkl} \neq \hat{\mathbb{C}}_{jikl} \tag{2.17a}$$

$$\hat{\mathbb{D}}_{ijkl} \neq \hat{\mathbb{D}}_{jikl} \tag{2.17b}$$

The transformation of the stresses and strains from a fixed (inertial) coordinate system to a fiber-oriented coordinate system is done through the microrotation tensor

$$\hat{\boldsymbol{\Sigma}} = \boldsymbol{R}^T \cdot \boldsymbol{\Sigma} \cdot \mathbf{R} \tag{2.18a}$$

$$\hat{\mathbf{M}} = \mathbf{R}^T \cdot \mathbf{M} \cdot \mathbf{R} \tag{2.18b}$$

$$\hat{\boldsymbol{\Gamma}} = \mathbf{R}^T \cdot \boldsymbol{\Gamma} \cdot \mathbf{R} \tag{2.19a}$$

$$\hat{\mathbf{K}} = \mathbf{R}^T \cdot \mathbf{K} \cdot \mathbf{R} \tag{2.19b}$$

Substituting these relations in Eqn. 2.15, the stiffness tensors transform according to

$$\mathbb{C}_{ijkl} = R_{im} R_{jn} R_{kp} R_{lq} \hat{\mathbb{C}}_{mnpq} \tag{2.20a}$$

$$\mathbb{D}_{ijkl} = R_{im} R_{jn} R_{kp} R_{lq} \hat{\mathbb{D}}_{mnpq} \tag{2.20b}$$

2.3 Transversely Isotropic Constitutive Relationship

The 3D transversely isotropic constitutive relation of a micropolar solid contains 18 independent material constants [39]. For the purpose of reducing the number of material constants introduced in the theory, we will consider the 2D simplification in the case of a planar deformation, where the nonzero displacement and rotational fields are $\boldsymbol{u} = (u_1, u_2, 0)$, $\boldsymbol{\varphi} = (0, 0, \varphi_3)$. In that case, the constitutive relation between the nonzero stresses and strains, in vector form is [40]

$$\begin{pmatrix} \hat{\Sigma}_{11} \\ \hat{\Sigma}_{22} \\ \hat{\Sigma}_{12} \\ \hat{\Sigma}_{21} \\ \hat{M}_{13} \\ \hat{M}_{23} \end{pmatrix} = \begin{bmatrix} \hat{\mathbb{C}}_{1111} & \hat{\mathbb{C}}_{1112} & 0 & 0 & 0 & 0 \\ \hat{\mathbb{C}}_{1112} & \hat{\mathbb{C}}_{2222} & 0 & 0 & 0 & 0 \\ 0 & 0 & \hat{\mathbb{C}}_{1212} & \hat{\mathbb{C}}_{1221} & 0 & 0 \\ 0 & 0 & \hat{\mathbb{C}}_{1221} & \hat{\mathbb{C}}_{2121} & 0 & 0 \\ 0 & 0 & 0 & 0 & \hat{\mathbb{D}}_{1313} & 0 \\ 0 & 0 & 0 & 0 & 0 & \hat{\mathbb{D}}_{2323} \end{bmatrix} \begin{pmatrix} \hat{\Gamma}_{11} \\ \hat{\Gamma}_{22} \\ \hat{\Gamma}_{12} \\ \hat{\Gamma}_{21} \\ \hat{K}_{13} \\ \hat{K}_{23} \end{pmatrix} \tag{2.21}$$

In addition, the out-of-plane stress is

$$\hat{\Sigma}_{33} = \hat{\mathbb{C}}_{1112}\hat{\Gamma}_{11} + \hat{\mathbb{C}}_{2223}\hat{\Gamma}_{22} \tag{2.22}$$

In the above 2D simplification, there are 9 independent material constants that need to be considered. Although the proceeding analysis will focus on planar deformation for simplicity, the extension of it to 3D is analogous.

In order to assign a physical meaning to the material constants $\hat{\mathbb{C}}$ and $\hat{\mathbb{D}}$, it is sometimes convenient to express the constitutive relation above in terms of the symmetric and skew-symmetric components of $\hat{\boldsymbol{\Sigma}}$ and $\hat{\boldsymbol{\Gamma}}$. The asymmetric stress tensor $\hat{\boldsymbol{\Sigma}}$ can be decomposed as

$$\hat{\boldsymbol{\Sigma}} = \hat{\boldsymbol{S}} + \hat{\boldsymbol{T}} \tag{2.23a}$$

$$\hat{\boldsymbol{S}} = \frac{\hat{\boldsymbol{\Sigma}} + \hat{\boldsymbol{\Sigma}}^T}{2} = \hat{\boldsymbol{S}}^T \tag{2.23b}$$

$$\hat{\boldsymbol{T}} = \frac{\hat{\boldsymbol{\Sigma}} - \hat{\boldsymbol{\Sigma}}^T}{2} = -\hat{\boldsymbol{T}}^T \tag{2.23c}$$

where $\hat{\boldsymbol{S}}$ and $\hat{\boldsymbol{T}}$ are the symmetric and antisymmetric components of $\hat{\boldsymbol{\Sigma}}$, respectively. Similarly, the decomposition of the asymmetric strain $\hat{\boldsymbol{\Gamma}}$ is

$$\hat{\boldsymbol{\Gamma}} = \hat{\boldsymbol{e}} + \hat{\boldsymbol{A}} \tag{2.24a}$$

$$\hat{\boldsymbol{e}} = \frac{\hat{\boldsymbol{\Gamma}} + \hat{\boldsymbol{\Gamma}}^T}{2} = \hat{\boldsymbol{e}}^T = \frac{1}{2}\left(\nabla \boldsymbol{u} + (\nabla \boldsymbol{u})^T\right) \tag{2.24b}$$

$$\hat{\boldsymbol{A}} = \frac{\hat{\boldsymbol{\Gamma}} - \hat{\boldsymbol{\Gamma}}^T}{2} = -\hat{\boldsymbol{A}}^T = \boldsymbol{\Phi} - \boldsymbol{\Psi} \tag{2.24c}$$

where $\boldsymbol{\Psi}$ is a skew-symmetric tensor

$$\boldsymbol{\Psi} = \frac{1}{2}\left(\nabla \boldsymbol{u} - (\nabla \boldsymbol{u})^T\right) \tag{2.25}$$

corresponding to the global rotation (or macrorotation) vector $\boldsymbol{\psi} = \frac{1}{2}\nabla \times \boldsymbol{u}$ defined in a Cauchy continuum. The constitutive relationship, in matrix form, in terms of decomposed stress and strain tensors is

$$\begin{pmatrix} \hat{S}_{11} \\ \hat{S}_{22} \\ \hat{S}_{12} \\ \hat{T}_{12} \\ \hat{M}_{13} \\ \hat{M}_{23} \end{pmatrix} = \begin{bmatrix} \hat{C}_{11} & \hat{C}_{12} & 0 & 0 & 0 & 0 \\ \hat{C}_{12} & \hat{C}_{22} & 0 & 0 & 0 & 0 \\ 0 & 0 & \hat{C}_{33} & \hat{C}_{34} & 0 & 0 \\ 0 & 0 & \hat{C}_{34} & \hat{C}_{44} & 0 & 0 \\ 0 & 0 & 0 & 0 & \hat{C}_{55} & 0 \\ 0 & 0 & 0 & 0 & 0 & \hat{C}_{66} \end{bmatrix} \begin{pmatrix} \hat{e}_{11} \\ \hat{e}_{22} \\ 2\hat{e}_{12} \\ 2\hat{A}_{12} \\ \hat{K}_{13} \\ \hat{K}_{23} \end{pmatrix} \tag{2.26}$$

In addition, the out-of-plane nonzero stress is

$$\hat{S}_{33} = \hat{C}_{12}\hat{e}_{11} + \hat{C}_v\hat{e}_{22} \tag{2.27}$$

The material properties in Eqns. 2.26, 2.27 in terms of the constants in Eqns. 2.21, 2.22 are

$$\hat{C}_{11} = \hat{\mathbb{C}}_{1111} \tag{2.28a}$$

$$\hat{C}_{22} = \hat{\mathbb{C}}_{2222} \tag{2.28b}$$

$$\hat{C}_{12} = \hat{\mathbb{C}}_{1122} \tag{2.28c}$$

$$\hat{C}_{33} = \frac{1}{4}(\hat{\mathbb{C}}_{1212} + 2\hat{\mathbb{C}}_{1221} + \hat{\mathbb{C}}_{2121}) \tag{2.28d}$$

$$\hat{C}_{44} = \hat{\mathbb{C}}_{1212} - 2\hat{\mathbb{C}}_{1221} + \hat{\mathbb{C}}_{2121} \tag{2.28e}$$

$$\hat{C}_{34} = \frac{1}{4}(\hat{\mathbb{C}}_{1212} - \hat{\mathbb{C}}_{2121}) \tag{2.28f}$$

$$\hat{C}_{55} = \hat{\mathbb{C}}_{1313} \tag{2.28g}$$

$$\hat{C}_{66} = \hat{\mathbb{C}}_{2323} \tag{2.28h}$$

$$\hat{C}_v = \hat{\mathbb{C}}_{2223} \tag{2.28i}$$

By assuming that the symmetric stress $\hat{S}_{11}$ and $\hat{e}_{11}$ correspond to those in a Cauchy continuum, the material constants relating them are

$$\hat{C}_{11} = \frac{\hat{E}_{11}^2(\hat{v}_{23} - 1)}{\Lambda} \tag{2.29a}$$

$$\hat{C}_{12} = -\frac{\hat{E}_{11}\hat{E}_{22}\hat{v}_{12}}{\Lambda} \tag{2.29b}$$

$$\hat{C}_{22} = \frac{\hat{E}_{22}(\hat{E}_{22}\hat{v}_{12}^2 - \hat{E}_{11})}{\Lambda(1 + \hat{v}_{23})} \tag{2.29c}$$

$$\hat{C}_v = -\frac{\hat{E}_{22}(\hat{E}_{22}\hat{v}_{12}^2 + \hat{E}_{11}\hat{v}_{23})}{\Lambda(1 + \hat{v}_{23})} \tag{2.29d}$$

$$\hat{C}_{33} = \hat{G}_{12} \tag{2.29e}$$

where

$$\Lambda = 2\hat{E}_{22}\hat{v}_{12}^2 + \hat{E}_{11}(\hat{v}_{23} - 1) \tag{2.30}$$

$\hat{C}_{ij}$ is written in terms of the classical Young's modulus $\hat{E}_{ij}$, Poisson's ratio $\hat{v}_{ij}$, and the shear modulus $\hat{G}_{12}$, for a plane strain consideration.

2.4 Anisotropic Elastoplasticity Formulation: Hill's Micropolar Criterion

Fiber reinforced composites also exhibit material nonlinearity. In literature, there have been various approaches that have been proposed to capture this. In the following analysis, we will proceed by considering an orthotropic elastoplastic model, under the consideration of a flow rule. In this approach, the existence of a yield function, which determines the elastic regime of the material, is assumed and it takes the general form

$$f = f(\hat{\boldsymbol{\Sigma}}, \hat{\boldsymbol{M}}, \kappa) \tag{2.31}$$

which is in terms of fiber-oriented Cauchy stresses and couple-stresses, $\hat{\boldsymbol{\Sigma}}$ and $\hat{\boldsymbol{M}}$, respectively, so that it satisfies the frame invariance requirement for anisotropic yielding. The scalar history variable, κ, in the case of isotropic work hardening (or softening), is expressed in terms of an equivalent stress $\kappa = \sigma_e(\epsilon_p)$, which is a function of an equivalent plastic strain ϵ_p. In a general micropolar continuum, the yield function f represents an 18-dimensional stress space (9 stress and 9 couple stress components). The admissible stress states $\hat{\boldsymbol{\Sigma}}$ and $\hat{\boldsymbol{M}}$, for a fixed history κ satisfy the condition $f \leq 0$, where the inequality defines the elastic region and the equality indicates the elastic limit. For a 2D planar deformation, the yielding condition is simplified into a 7-dimensional stress space

$$\begin{aligned} f = \Bigg(& \overline{F}\left(\hat{\Sigma}_{22} - \hat{\Sigma}_{33}\right)^2 + \overline{G}\left(\hat{\Sigma}_{33} - \hat{\Sigma}_{11}\right)^2 + \overline{H}\left(\hat{\Sigma}_{11} - \hat{\Sigma}_{22}\right)^2 \\ & + \frac{\overline{N}}{2}\left(\hat{\Sigma}_{12} + \hat{\Sigma}_{21}\right)^2 + \overline{Y}\hat{M}_{13}^2 + \overline{Z}\hat{M}_{23}^2 \Bigg)^{1/2} - \sigma_e(\epsilon_p) \end{aligned} \tag{2.32}$$

where the constants $\overline{F}, \overline{G}, \overline{H}, \overline{N}, \overline{Y}$, and $\overline{Z}$ are determined experimentally, which correspond to the relative easy/difficulty of yielding in different directions due to the anisotropy of the medium. This form is the extension of the pressure independent Hill criterion in classical elastoplasticity for orthotropic medium. Based on these assumptions, the following cases can be deduced from the generalized micropolar Hill's condition presented above: (1) $\overline{Y} = \overline{Z} = 0$ corresponds into Hill's anisotropic condition in classical elastoplasticity [3], and (2) $\overline{F} = \overline{G} = \overline{H} = \frac{1}{6}$, $\overline{L} = \overline{M} = \overline{N} = \frac{1}{2}$, and $\overline{Y} = \overline{Z} = 1$ corresponds to the micropolar isotropic von Mises criterion [41].

Analogous to classical elastoplasticity, the strain and curvature strain rates are decomposed in

$$\dot{\hat{\boldsymbol{\Gamma}}} = \dot{\hat{\boldsymbol{\Gamma}}}^e + \dot{\hat{\boldsymbol{\Gamma}}}^p \tag{2.33a}$$

$$\dot{\hat{\boldsymbol{K}}} = \dot{\hat{\boldsymbol{K}}}^{e} + \dot{\hat{\boldsymbol{K}}}^{p} \tag{2.33b}$$

where $\dot{\hat{\boldsymbol{\Gamma}}}^{e}$, $\dot{\hat{\boldsymbol{K}}}^{e}$ are the elastic and $\dot{\hat{\boldsymbol{\Gamma}}}^{p}$, $\dot{\hat{\boldsymbol{K}}}^{p}$ are the plastic components of the total strains.

In this, it should be emphasized that the commonly used rate notation $\dot{(\ )}$ is employed to indicate infinitesimal changes in a continuum, despite neglecting inertial and rate-dependent effects. Under the assumption of the associative flow rule, the plastic strains in terms of the potential function are

$$\dot{\hat{\boldsymbol{\Gamma}}}^{p} = \dot{\lambda}\frac{\partial f}{\partial \hat{\boldsymbol{\Sigma}}} = \dot{\lambda}\hat{\boldsymbol{n}}^{\Sigma} \tag{2.34a}$$

$$\dot{\hat{\boldsymbol{K}}}^{p} = \dot{\lambda}\frac{\partial f}{\partial \hat{\boldsymbol{M}}} = \dot{\lambda}\hat{\boldsymbol{n}}^{M} \tag{2.34b}$$

where $\hat{\boldsymbol{n}}^{\Sigma}$ and $\hat{\boldsymbol{n}}^{M}$ are the gradients of the yield surface in stress space. The plastic multiplier $\dot{\lambda} \geq 0$ is a non-negative scalar that assumes a positive value during plastic loading, and is zero during elastic loading/unloading. Taking the constitutive relation between the stresses and elastic strains, in rate form it reduces to

$$\dot{\hat{\boldsymbol{\Sigma}}} = \hat{\mathbb{C}} : \dot{\hat{\boldsymbol{\Gamma}}}^{e} = \hat{\mathbb{C}} : \left(\dot{\hat{\boldsymbol{\Gamma}}} - \dot{\lambda}\hat{\boldsymbol{n}}^{\Sigma}\right) \tag{2.35a}$$

$$\dot{\hat{\boldsymbol{M}}} = \hat{\mathbb{D}} : \dot{\hat{\boldsymbol{K}}}^{e} = \hat{\mathbb{D}} : \left(\dot{\hat{\boldsymbol{K}}} - \dot{\lambda}\hat{\boldsymbol{n}}^{M}\right) \tag{2.35b}$$

2.4.1 Plastic Work Rate

An important concept in the formulation of plasticity is the definition of the equivalent stress (σ_e) and the plastic strain (ε_p), which relate the state of a material under multiaxial loads to a uniaxial loading state. To proceed, the plastic work rate is defined as

$$\dot{W}_p = \hat{\boldsymbol{\Sigma}} : \dot{\hat{\boldsymbol{\Gamma}}}^{p} + \hat{\boldsymbol{M}} : \dot{\hat{\boldsymbol{K}}}^{p} = \sigma_e \dot{\varepsilon}_p \tag{2.36}$$

By defining the equivalent stress in this form,

$$\begin{aligned}\sigma_e^2 = \overline{F}\left(\hat{\Sigma}_{22}-\hat{\Sigma}_{33}\right)^2 + \overline{G}\left(\hat{\Sigma}_{33}-\hat{\Sigma}_{11}\right)^2 + \overline{H}\left(\hat{\Sigma}_{11}-\hat{\Sigma}_{22}\right)^2 \\ + \frac{\overline{N}}{2}\left(\hat{\Sigma}_{12}+\hat{\Sigma}_{21}\right)^2 + \overline{Y}\hat{M}_{13}^2 + \overline{Z}\hat{M}_{23}^2\end{aligned} \tag{2.37}$$

its plastic work conjugate $\dot{\varepsilon}_p$ is determined by algebraic manipulation of Eqn. 2.36 to be

$$\dot{\varepsilon}_p = \frac{\hat{\boldsymbol{\Sigma}} : \dot{\hat{\boldsymbol{\Gamma}}}^p + \hat{\boldsymbol{M}} : \dot{\hat{\boldsymbol{K}}}^p}{\sigma_e} = \left(\frac{\hat{\boldsymbol{\Sigma}} : \hat{\boldsymbol{n}}^{\Sigma} + \hat{\boldsymbol{M}} : \hat{\boldsymbol{n}}^{M}}{\sigma_e}\right)\dot{\lambda} = \dot{\lambda} \quad (\geq 0) \tag{2.38}$$

By integrating the equivalent plastic strain rate over time, the total equivalent plastic strain is obtained

$$\varepsilon_p = \int \dot{\varepsilon}_p d\tau = \int \dot{\lambda} d\tau \tag{2.39}$$

The nonzero value of $\dot{\lambda}$ during plastic flow is determined using the consistency condition, which requires the state of stress to remain on the yield surface during plastic loading

$$\begin{aligned}\dot{f}(\hat{\boldsymbol{\Sigma}}, \hat{\boldsymbol{M}}, \sigma_e) = \frac{\partial f}{\partial \hat{\boldsymbol{\Sigma}}} : \dot{\hat{\boldsymbol{\Sigma}}} + \frac{\partial f}{\partial \hat{\boldsymbol{M}}} : \dot{\hat{\boldsymbol{M}}} + \frac{d\sigma_e}{d\varepsilon_p}\dot{\varepsilon}_p = 0 \\ \hat{\boldsymbol{n}}^{\Sigma} : (\hat{\mathbb{C}} : \dot{\hat{\boldsymbol{\Gamma}}} + \dot{\lambda}\hat{\mathbb{C}} : \hat{\boldsymbol{n}}^{\Sigma}) + \hat{\boldsymbol{n}}^{M} : (\hat{\mathbb{D}} : \dot{\hat{\boldsymbol{K}}} + \dot{\lambda}\hat{\mathbb{D}} : \hat{\boldsymbol{n}}^{M}) + E_p\dot{\varepsilon}_p = 0\end{aligned} \tag{2.40}$$

The plastic modulus $E_p = \frac{d\sigma_e}{d\varepsilon_p}$ is the tangent stiffness of the equivalent stress-strain curve, which is obtained experimentally. The corresponding expression for the plastic multiplier is simplified to

$$\dot{\lambda} = \frac{\hat{\boldsymbol{H}}^{\Sigma} : \dot{\hat{\boldsymbol{\Gamma}}} + \hat{\boldsymbol{H}}^{M} : \dot{\hat{\boldsymbol{K}}}}{h} \tag{2.41}$$

where

$$\hat{\boldsymbol{H}}^{\Sigma} = \hat{\mathbb{C}} : \hat{\boldsymbol{n}}^{\Sigma} \tag{2.42a}$$

$$\hat{\boldsymbol{H}}^{M} = \hat{\mathbb{D}} : \hat{\boldsymbol{n}}^{M} \tag{2.42b}$$

$$h = E_p + \hat{\boldsymbol{n}}^{\Sigma} : \hat{\boldsymbol{H}}^{\Sigma} + \hat{\boldsymbol{n}}^{M} : \hat{\boldsymbol{H}}^{M} > 0 \tag{2.42c}$$

Since h is a positive scalar, the numerator of $\dot{\lambda}$ is used to determine the loading/unloading conditions:

$$\hat{\boldsymbol{H}}^{\Sigma} : \dot{\hat{\boldsymbol{\Gamma}}} + \hat{\boldsymbol{H}}^{M} : \dot{\hat{\boldsymbol{K}}} \quad \begin{cases} < 0 & \text{elastic loading} \\ = 0 & \text{neutral loading} \\ > 0 & \text{plastic loading} \end{cases} \tag{2.43}$$

Next, substituting the value of $\dot{\lambda}$ in Eqn. 2.35, the stress and couple-stress rates in compact form are

$$\begin{pmatrix} \dot{\hat{\boldsymbol{\Sigma}}} \\ \dot{\hat{\boldsymbol{M}}} \end{pmatrix} = \begin{bmatrix} \hat{\mathbb{C}}^{ep} & \hat{\mathbb{B}}^{ep} \\ (\hat{\mathbb{B}}^{ep})^T & \hat{\mathbb{D}}^{ep} \end{bmatrix} : \begin{pmatrix} \dot{\hat{\boldsymbol{\Gamma}}} \\ \dot{\hat{\boldsymbol{K}}} \end{pmatrix} \tag{2.44}$$

where

$$\hat{\mathbb{C}}^{ep} = \hat{\mathbb{C}} - \frac{\hat{\boldsymbol{H}}^{\Sigma} \bigotimes \hat{\boldsymbol{H}}^{\Sigma}}{h} \quad or \quad \hat{\mathbb{C}}^{ep}_{ijkl} = \hat{\mathbb{C}}_{ijkl} - \frac{\hat{H}^{\Sigma}_{ij} \hat{H}^{\Sigma}_{kl}}{h} \tag{2.45a}$$

$$\hat{\mathbb{B}}^{ep} = -\frac{\hat{\boldsymbol{H}}^{\Sigma} \bigotimes \hat{\boldsymbol{H}}^{M}}{h} \quad or \quad \hat{\mathbb{B}}^{ep}_{ijkl} = -\frac{\hat{H}^{\Sigma}_{ij} \hat{H}^{M}_{kl}}{h} \tag{2.45b}$$

$$\hat{\mathbb{D}}^{ep} = \hat{\mathbb{D}} - \frac{\hat{\boldsymbol{H}}^{M} \bigotimes \hat{\boldsymbol{H}}^{M}}{h} \quad or \quad \hat{\mathbb{D}}^{ep}_{ijkl} = \hat{\mathbb{D}}_{ijkl} - \frac{\hat{H}^{M}_{ij} \hat{H}^{M}_{kl}}{h} \tag{2.45c}$$

The transpose over the fourth order tensors indicates transpose over the major indices $\left(\hat{\mathbb{B}}^{ep,T}_{ijkl} = (\hat{\mathbb{B}}^{ep}_{ijkl})^T = \hat{\mathbb{B}}^{ep}_{klij}\right)$. In the application of the equations above in a finite element form, which will be discussed, it is convenient to express the elastoplastic constitutive relation in terms of the symmetric and skew-symmetric stresses and strains

defined in Eqn. 2.23 and Eqn. 2.24, which results in

$$\begin{pmatrix} \dot{\hat{\boldsymbol{S}}} \\ \dot{\hat{\boldsymbol{T}}} \\ \dot{\hat{\boldsymbol{M}}} \end{pmatrix} = \begin{bmatrix} \hat{\mathbb{L}}^{ep} & \hat{\mathbb{M}}^{ep} & \hat{\mathbb{N}}^{ep} \\ (\hat{\mathbb{M}}^{ep})^T & \hat{\mathbb{H}}^{ep} & \hat{\mathbb{Q}}^{ep} \\ (\hat{\mathbb{N}}^{ep})^T & (\hat{\mathbb{Q}}^{ep})^T & \hat{\mathbb{D}}^{ep} \end{bmatrix} : \begin{pmatrix} \dot{\boldsymbol{e}} \\ \dot{\hat{\boldsymbol{A}}} \\ \dot{\hat{\boldsymbol{K}}} \end{pmatrix} \tag{2.46}$$

where

$$\hat{\mathbb{L}}^{ep}_{ijkl} = \frac{(\hat{\mathbb{C}}^{ep}_{ijkl} + \hat{\mathbb{C}}^{ep}_{jikl} + \hat{\mathbb{C}}^{ep}_{ijlk} + \hat{\mathbb{C}}^{ep}_{jilk})}{4} \tag{2.47a}$$

$$\hat{\mathbb{M}}^{ep}_{ijkl} = \frac{(\hat{\mathbb{C}}^{ep}_{ijkl} + \hat{\mathbb{C}}^{ep}_{jikl} - \hat{\mathbb{C}}^{ep}_{ijlk} - \hat{\mathbb{C}}^{ep}_{jilk})}{4} \tag{2.47b}$$

$$\hat{\mathbb{N}}^{ep}_{ijkl} = \frac{(\hat{\mathbb{B}}^{ep}_{ijkl} + \hat{\mathbb{B}}^{ep}_{jikl})}{2} \tag{2.47c}$$

$$\hat{\mathbb{H}}^{ep}_{ijkl} = \frac{(\hat{\mathbb{C}}^{ep}_{ijkl} - \hat{\mathbb{C}}^{ep}_{jikl} - \hat{\mathbb{C}}^{ep}_{ijlk} + \hat{\mathbb{C}}^{ep}_{jilk})}{4} \tag{2.47d}$$

$$\hat{\mathbb{Q}}^{ep}_{ijkl} = \frac{(\hat{\mathbb{B}}^{ep}_{ijkl} - \hat{\mathbb{B}}^{ep}_{jikl})}{2} \tag{2.47e}$$

For the 2D case, in vector form, the relevant stresses and strains are arranged in the form

$$\{\dot{\hat{\boldsymbol{\sigma}}}\} = [\hat{\boldsymbol{C}}^{ep}]\{\dot{\hat{\boldsymbol{\gamma}}}\} \tag{2.48}$$

The components of the 6×6 elastoplastic stiffness matrix $[\hat{\boldsymbol{C}}^{ep}]$ is given in Appendix A and the stress and strain vector arrangements are

$$\{\dot{\hat{\boldsymbol{\sigma}}}\}^T = \{\dot{\hat{S}}_{11} \;\; \dot{\hat{S}}_{22} \;\; \dot{\hat{S}}_{12} \;\; \dot{\hat{T}}_{12} \;\; \dot{\hat{M}}_{13} \;\; \dot{\hat{M}}_{23}\} \tag{2.49a}$$

$$\{\dot{\hat{\boldsymbol{\gamma}}}\}^T = \{\dot{\hat{e}}_{11} \;\; \dot{\hat{e}}_{22} \;\; 2\dot{\hat{e}}_{12} \;\; 2\dot{\hat{A}}_{12} \;\; \dot{\hat{K}}_{13} \;\; \dot{\hat{K}}_{23}\} \tag{2.49b}$$

In addition, for a plane strain formulation, the out-of-plane stress rate $\dot{\hat{S}}_{33}$ is nonzero, which is also given in Appendix A.

2.5 Objective Stress Rates

In the above formulations, the stresses, strains, and the material properties have been defined in an orthogonal fiber-aligned corotational coordinate system. The transformation of the stresses indicated in Eqn. 2.18 cannot be extended to the stress rates directly ($\dot{\hat{\boldsymbol{\Sigma}}} \neq \boldsymbol{R}^T \cdot \dot{\boldsymbol{\Sigma}} \cdot \mathbf{R}$, $\dot{\hat{\boldsymbol{M}}} \neq \boldsymbol{R}^T \cdot \dot{\boldsymbol{M}} \cdot \mathbf{R}$). The correct formulation is obtained by taking the time differential of Eqn. 2.18

$$\dot{\hat{\boldsymbol{\Sigma}}} = \dot{\mathbf{R}}^T \cdot \boldsymbol{\Sigma} \cdot \mathbf{R} + \mathbf{R}^T \cdot \dot{\boldsymbol{\Sigma}} \cdot \mathbf{R} + \mathbf{R}^T \cdot \boldsymbol{\Sigma} \cdot \dot{\mathbf{R}} = \mathbf{R}^T \cdot \boldsymbol{\Sigma}^{\nabla G} \cdot \mathbf{R} \tag{2.50a}$$

$$\dot{\hat{\mathbf{M}}} = \dot{\mathbf{R}}^T \cdot \mathbf{M} \cdot \mathbf{R} + \mathbf{R}^T \cdot \dot{\mathbf{M}} \cdot \mathbf{R} + \mathbf{R}^T \cdot \mathbf{M} \cdot \dot{\mathbf{R}} = \mathbf{R}^T \cdot \mathbf{M}^{\nabla G} \cdot \mathbf{R} \tag{2.50b}$$

$\boldsymbol{\Sigma}^{\nabla G}$ and $\mathbf{M}^{\nabla G}$ are new micropolar corotational stress rates, which are analogous in definition to the objective Green-Naghdi stress rate in a Cauchy continuum.

$$\boldsymbol{\Sigma}^{\nabla G} = \dot{\boldsymbol{\Sigma}} - \boldsymbol{\Omega} \cdot \boldsymbol{\Sigma} - \boldsymbol{\Sigma} \cdot \boldsymbol{\Omega}^T \tag{2.51a}$$

$$\mathbf{M}^{\nabla G} = \dot{\mathbf{M}} - \boldsymbol{\Omega} \cdot \mathbf{M} - \mathbf{M} \cdot \boldsymbol{\Omega}^T \tag{2.51b}$$

$\boldsymbol{\Omega} = \dot{\mathbf{R}} \cdot \mathbf{R}^T$ is called the skew-symmetric gyration tensor. Using the microrotation tensor in Eqn. 2.9 for 2D deformation, the gyration tensor results in

$$\boldsymbol{\Omega} = \begin{bmatrix} 0 & -\dot{\varphi}_3 & 0 \\ \dot{\varphi}_3 & 0 & 0 \\ 0 & 0 & 0 \end{bmatrix} \tag{2.52}$$

With the equations defined above, the stress rates with respect to the global coordinates are

$$\dot{\boldsymbol{\Sigma}} = \mathbf{R} \cdot \dot{\hat{\boldsymbol{\Sigma}}} \cdot \mathbf{R}^T + \boldsymbol{\Omega} \cdot \boldsymbol{\Sigma} + \boldsymbol{\Sigma} \cdot \boldsymbol{\Omega}^T \tag{2.53a}$$

$$\dot{\mathbf{M}} = \mathbf{R} \cdot \dot{\hat{\mathbf{M}}} \cdot \mathbf{R}^T + \boldsymbol{\Omega} \cdot \mathbf{M} + \mathbf{M} \cdot \boldsymbol{\Omega}^T \tag{2.53b}$$

The corresponding strain rates transform as

$$\dot{\hat{\boldsymbol{\Gamma}}} = \boldsymbol{R}^T \cdot \dot{\boldsymbol{\Gamma}} \cdot \boldsymbol{R} \tag{2.54a}$$

$$\dot{\hat{\boldsymbol{K}}} = \boldsymbol{R}^T \cdot \dot{\boldsymbol{K}} \cdot \boldsymbol{R} \tag{2.54b}$$

which is proven in [42]. With the constitutive relation defined in Eqn. 2.44, substituting these in Eqn. 2.53 results in

$$\begin{Bmatrix} \dot{\boldsymbol{\Sigma}} \\ \dot{\boldsymbol{M}} \end{Bmatrix} = \begin{bmatrix} \mathbb{C}^{ep} & \mathbb{B}^{ep} \\ (\hat{\mathbb{B}}^{ep})^T & \mathbb{D}^{ep} \end{bmatrix} : \begin{Bmatrix} \dot{\boldsymbol{\Gamma}} \\ \dot{\boldsymbol{K}} \end{Bmatrix} + \boldsymbol{\Omega} \cdot \begin{Bmatrix} \boldsymbol{\Sigma} \\ \boldsymbol{M} \end{Bmatrix} + \begin{Bmatrix} \boldsymbol{\Sigma} \\ \boldsymbol{M} \end{Bmatrix} \cdot \boldsymbol{\Omega}^T \tag{2.55}$$

where

$$\begin{bmatrix} \mathbb{C}^{ep}_{ijkl} & \mathbb{B}^{ep}_{ijkl} \\ \mathbb{B}^{ep,T}_{ijkl} & \mathbb{D}^{ep}_{ijkl} \end{bmatrix} = R_{iq}R_{jp}R_{fk}R_{ml} \begin{bmatrix} \hat{\mathbb{C}}^{ep}_{ijkl} & \hat{\mathbb{B}}^{ep}_{ijkl} \\ \hat{\mathbb{B}}^{ep,T}_{ijkl} & \hat{\mathbb{D}}^{ep}_{ijkl} \end{bmatrix} \tag{2.56}$$

Similarly, in terms of the symmetric and skew-symmetric stress and strain components, the constitutive equations are

$$\begin{Bmatrix} \dot{\boldsymbol{S}} \\ \dot{\boldsymbol{T}} \\ \dot{\boldsymbol{M}} \end{Bmatrix} = \begin{bmatrix} \mathbb{L}^{ep} & \mathbb{M}^{ep} & \mathbb{N}^{ep} \\ (\mathbb{M}^{ep})^T & \mathbb{H}^{ep} & \mathbb{Q}^{ep} \\ (\mathbb{N}^{ep})^T & (\mathbb{Q}^{ep})^T & \mathbb{D}^{ep} \end{bmatrix} : \begin{Bmatrix} \dot{\boldsymbol{e}} \\ \dot{\boldsymbol{A}} \\ \dot{\boldsymbol{K}} \end{Bmatrix} + \boldsymbol{\Omega} \cdot \begin{Bmatrix} \boldsymbol{S} \\ \boldsymbol{T} \\ \boldsymbol{M} \end{Bmatrix} + \begin{Bmatrix} \boldsymbol{S} \\ \boldsymbol{T} \\ \boldsymbol{M} \end{Bmatrix} \cdot \boldsymbol{\Omega}^T \tag{2.57}$$

where

$$\begin{bmatrix} \mathbb{L}^{ep}_{ijkl} & \mathbb{M}^{ep}_{ijkl} & \mathbb{N}^{ep}_{ijkl} \\ \mathbb{M}^{ep,T}_{ijkl} & \mathbb{H}^{ep}_{ijkl} & \mathbb{Q}^{ep}_{ijkl} \\ \mathbb{N}^{ep,T}_{ijkl} & \mathbb{Q}^{ep,T}_{ijkl} & \mathbb{D}^{ep}_{ijkl} \end{bmatrix} = R_{iq}R_{jp}R_{fk}R_{ml} \begin{bmatrix} \hat{\mathbb{L}}^{ep}_{ijkl} & \hat{\mathbb{M}}^{ep}_{ijkl} & \hat{\mathbb{N}}^{ep}_{ijkl} \\ \hat{\mathbb{M}}^{ep,T}_{ijkl} & \hat{\mathbb{H}}^{ep}_{ijkl} & \hat{\mathbb{Q}}^{ep}_{ijkl} \\ \hat{\mathbb{N}}^{ep,T}_{ijkl} & \hat{\mathbb{Q}}^{ep,T}_{ijkl} & \hat{\mathbb{D}}^{ep}_{ijkl} \end{bmatrix} \tag{2.58}$$

In a 2D finite element implementation, the preferred vector form is

$$\{\dot{\boldsymbol{\sigma}}\} = [\boldsymbol{C}^{ep}]\{\dot{\boldsymbol{\gamma}}\} + \dot{\varphi}_3\{\boldsymbol{\sigma}_\Omega\} \tag{2.59}$$

where the arrangement of $\{\dot{\boldsymbol{\sigma}}\}$ and $\{\dot{\boldsymbol{\gamma}}\}$ are according to Eqn. 2.49 and

$$[\boldsymbol{C}^{ep}] = [\boldsymbol{T}_e]^T[\hat{\boldsymbol{C}}^{ep}][\boldsymbol{T}_e] \tag{2.60a}$$

$$\{\boldsymbol{\sigma}_\Omega\}^T = \{-2S_{12} \;\; 2S_{12} \;\; (S_{11} - S_{22}) \;\; 0 \;\; -M_{23} \;\; M_{13}\} \tag{2.60b}$$

The 6×6 matrix $[\boldsymbol{C}^{ep}]$ is the elastoplastic stiffness matrix with respect to a global coordinate system. In addition, the transformation matrix is

$$[\boldsymbol{T}_e] = \begin{bmatrix} m^2 & n^2 & mn & 0 & 0 & 0 \\ n^2 & m^2 & -mn & 0 & 0 & 0 \\ -2mn & 2mn & (m^2 - n^2) & 0 & 0 & 0 \\ 0 & 0 & 0 & 1 & 0 & 0 \\ 0 & 0 & 0 & 0 & m & n \\ 0 & 0 & 0 & 0 & -n & m \end{bmatrix} \tag{2.61}$$

with $m = \cos(\varphi_3)$ and $n = \sin(\varphi_3)$.

2.6 Updated Lagrangian Formulation

In nonlinear micropolar theory, the geometric exact strain measures are the unsymmetric stretch tensor $\boldsymbol{U}$ and the general curvature tensor, which is discussed, for example in [42] and [43], etc. Unlike the Green-Lagrange strain in a Cauchy continuum, where the strain measure is second order nonlinear, in micropolar theory, the higher order nonlinearity introduced are of infinite order. In the general finite micropolar theory, the issue that is encountered is that when the additional material constants are neglected, the strain measure does not reduce to the classical Green-Lagrange strain tensor. Thus, results from finite classical elasticity are not deduced from the general finite micropolar theory. This is discussed more in detail in [44],

[45], which needs further study. In order to circumvent these complications for practical engineering application, we consider a micropolar continuum, undergoing finite symmetric strain, while the micropolar skew-symmetric strain and the curvature are linear in displacement and rotation. For example, this assumption was employed by [46] for analyzing localization in granular materials, with a softening constitutive relation. Due to the isotropy of the material, their yield criterion is only a function of the invariants of the stress tensors and the consideration of the local coordinate system is unnecessary. This assumption cannot be applied to anisotropic fiber reinforced composites, as seen in Eqn. 2.31.

Under an updated Lagrangian (UL) formulation, where the reference frame is taken as the previous calculated configuration at time t_n, the principle of virtual displacement for a micropolar medium, in terms of the symmetric and antisymmetric stress and strain measures is

$$\int_{{}^{n}V} ({}^{n+1}_{n}\boldsymbol{S} : \delta {}^{n+1}_{n}\boldsymbol{G} + {}^{n+1}_{n}\boldsymbol{T} : \delta {}^{n+1}_{n}\boldsymbol{A} + {}^{n+1}_{n}\boldsymbol{M} : \delta {}^{n+1}_{n}\boldsymbol{K}) d^{n}V = {}^{n+1}\Re \qquad (2.62)$$

In this thesis, only the static response of the material is considered. Within this context, the deformation is considered in discrete fictitious time steps, from the configuration at time t_n to t_{n+1}. These time increments merely denote the load level. ${}^{n}V$ is the volume of the body at a known configuration n, ${}^{n+1}_{n}\boldsymbol{S}$, ${}^{n+1}_{n}\boldsymbol{T}$, and ${}^{n+1}_{n}\boldsymbol{M}$ are the symmetric stress, micropolar skew-symmetric stress, and couple-stress at time $n+1$, referred to the configuration at time n (the second Piola-Kirchoff stresses or PK2 stresses). The strain measures considered are the geometrically nonlinear Green-Lagrange strain ${}^{n+1}_{n}\boldsymbol{G}$, the linear micropolar skew-symmetric strain ${}^{n+1}_{n}\boldsymbol{A}$, and the linear curvature strain ${}^{n+1}_{n}\boldsymbol{K}$. In the expression above, we have used the notation introduced by Bathe [47].

The right hand side of Eqn. 2.62, or the external virtual work is

$$
\begin{aligned}
{}^{n+1}\mathfrak{R} = \int_{{}^{n+1}V} (\, {}^{n+1}\boldsymbol{f}^B \cdot \delta\boldsymbol{u} + \, {}^{n+1}\boldsymbol{C}^B \cdot \delta\boldsymbol{\varphi}) d^{n+1}V \\
+ \int_{{}^{n+1}S} (\, {}^{n+1}\boldsymbol{f}^S \cdot \delta\boldsymbol{u}^S + \, {}^{n+1}\boldsymbol{C}^S \cdot \delta\boldsymbol{\varphi}^S) d^{n+1}S
\end{aligned}
\tag{2.63}
$$

where ${}^{n+1}\boldsymbol{f}^B$, ${}^{n+1}\boldsymbol{C}^B$ are the external body forces and body couple-forces per unit volume at step $n+1$, and ${}^{n+1}\boldsymbol{f}^S$, ${}^{n+1}\boldsymbol{C}^S$ are the externally applied surface traction and couple-traction per unit surface area at step $n+1$.

In the UL formulation, the position of a point, displacement, and rotations at step $n+1$ are expressed as the sum of the last known configuration at step n and the incremental change

$$
{}^{n+1}\boldsymbol{x} = \, {}^{n}\boldsymbol{x} + \boldsymbol{x} \tag{2.64a}
$$

$$
{}^{n+1}\boldsymbol{u} = \, {}^{n}\boldsymbol{u} + \boldsymbol{u} \tag{2.64b}
$$

$$
{}^{n+1}\boldsymbol{\varphi} = \, {}^{n}\boldsymbol{\varphi} + \boldsymbol{\varphi} \tag{2.64c}
$$

where $\boldsymbol{u}$ and $\boldsymbol{\varphi}$ are the incremental change in displacement and local rotation, respectively, from the configuration at time n to $n+1$. Consequently, the variation of the total displacement and rotations at time $n+1$ are

$$
\delta \, {}^{n+1}\boldsymbol{u} = \delta(\, {}^{n}\boldsymbol{u} + \boldsymbol{u}) = \delta\boldsymbol{u} \tag{2.65a}
$$

$$
\delta \, {}^{n+1}\boldsymbol{\varphi} = \delta(\, {}^{n}\boldsymbol{\varphi} + \boldsymbol{\varphi}) = \delta\boldsymbol{\varphi} \tag{2.65b}
$$

where because step n is assumed to be known, the variation of the displacements and local rotations at frame n is $\delta \, {}^{n}\boldsymbol{u} = \delta \, {}^{n}\boldsymbol{\varphi} = 0$. Similarly, the strains are

$$
\delta \, {}^{n+1}_{n}G_{ij} = \delta \, {}_{n}G_{ij} = \delta \, {}_{n}e_{ij} + \delta \, {}_{n}\eta_{ij}, \;\; {}_{n}e_{ij} = \frac{1}{2}\left(\frac{\partial u_i}{\partial \, {}^{n}x_j} + \frac{\partial u_j}{\partial \, {}^{n}x_i} \right),
$$

$$ {}_n\eta_{ij} = \frac{1}{2}\left(\frac{\partial u_k}{\partial\ {}^n x_i}\frac{\partial u_k}{\partial\ {}^n x_j}\right) \tag{2.66a} $$

$$ \delta\ {}^{n+1}_{n}A_{ij} = \delta\ {}_nA_{ij} = \varepsilon_{ijk}\delta(\ {}_n\psi_k - \varphi_k), \qquad {}_n\psi_k = \frac{1}{2}\varepsilon_{ijk}\frac{\partial u_j}{\partial\ {}^n x_i} \tag{2.66b} $$

$$ \delta\ {}^{n+1}_{n}K_{ij} = \delta\ {}_nK_{ij}, \qquad {}_nK_{ij} = \frac{\partial \varphi_j}{\partial\ {}^n x_i} \tag{2.66c} $$

where ${}_n\boldsymbol{e}$ and ${}_n\boldsymbol{\eta}$ are the increments of the geometrically linear and nonlinear components of the symmetric Green-Lagrange strain, respectively, and ${}_n\boldsymbol{\psi}$ is the incremental change in global rotation, or the rotation definition of a point in a Cauchy continuum. Similarly, the PK2 stresses can be expressed

$$ {}^{n+1}_{n}\boldsymbol{S} = {}^n\boldsymbol{S} + {}_n\boldsymbol{S} \tag{2.67a} $$

$$ {}^{n+1}_{n}\boldsymbol{T} = {}^n\boldsymbol{T} + {}_n\boldsymbol{T} \tag{2.67b} $$

$$ {}^{n+1}_{n}\boldsymbol{M} = {}^n\boldsymbol{M} + {}_n\boldsymbol{M} \tag{2.67c} $$

where ${}^n\boldsymbol{S}$, ${}^n\boldsymbol{T}$, and ${}^n\boldsymbol{M}$ are the Cauchy stresses (forces and moments per deformed area) at configuration n and ${}_n\boldsymbol{S}$, ${}_n\boldsymbol{T}$, and ${}_n\boldsymbol{M}$ are the incremental change in PK2 stresses and couple stress from the configuration at n to $n+1$. Substituting these in the principle of virtual displacement results in

$$ \begin{aligned} \int_{{}_nV} (\ {}_n\boldsymbol{S} : \delta\ {}_n\boldsymbol{G} + {}_n\boldsymbol{T} : \delta\ {}_n\boldsymbol{A} + {}_n\boldsymbol{M} : \delta\ {}_n\boldsymbol{K})d^nV + \int_{{}_nV} (\ {}^n\boldsymbol{S} : \delta\ {}_n\boldsymbol{\eta})d^nV \\ = {}^{n+1}\mathfrak{R} - \int_{{}_nV} (\ {}^n\boldsymbol{S} : \delta_n\boldsymbol{e} + {}^n\boldsymbol{T} : \delta_n\boldsymbol{A} + {}^n\boldsymbol{M} : \delta_n\boldsymbol{K})d^nV \end{aligned} \tag{2.68} $$

In this expression, the first integral term on the left of the equality sign corresponds to the stiffness, the second integral term to the geometrically nonlinear stiffness contribution. Inside the second integral term on the right hand side of the equality sign are the residual Cauchy stresses from the time step n. Since ${}_n\boldsymbol{S}$, ${}_n\boldsymbol{T}$, and ${}_n\boldsymbol{M}$ are first order linear in strain increments, and the Cauchy stresses and couple stress are known at time n, the term corresponding to ${}_n\boldsymbol{S} : \delta\ {}_n\boldsymbol{G}$ is the only nonlinear

contribution to of incremental displacement and rotation. Linearizing in terms of $\boldsymbol{u}$ and $\boldsymbol{\varphi}$, the above equations can be represented as

$$\begin{aligned}\int_{{}^{n}V} \left(\{\delta_n \boldsymbol{E} \quad \delta_n \boldsymbol{A} \quad \delta_n \boldsymbol{K}\} : \left\{ \begin{array}{c} {}_{n}\boldsymbol{S} \\ {}_{n}\boldsymbol{T} \\ {}_{n}\boldsymbol{M} \end{array} \right\} \right) d\,{}^{n}V + \int_{{}^{n}V} (\delta\ {}_{n}\boldsymbol{\eta} :\ {}^{n}\boldsymbol{S}) d^{n}V \\ = {}^{n+1}\mathfrak{R} - \int_{{}^{n}V} \left(\{\delta_n \boldsymbol{e} \quad \delta_n \boldsymbol{A} \quad \delta_n \boldsymbol{K}\} : \left\{ \begin{array}{c} {}^{n}\boldsymbol{S} \\ {}^{n}\boldsymbol{T} \\ {}^{n}\boldsymbol{M} \end{array} \right\} \right) d\,{}^{n}V \end{aligned} \tag{2.69}$$

In 2D, this can also be represented in simplified form as

$$\begin{aligned}\int_{{}^{n}V} \left(\{\delta_n \boldsymbol{\gamma}\}^T \{\ {}_{n}\boldsymbol{\sigma}\} \right) d\,{}^{n}V + \int_{{}^{n}V} (\{\delta_n \boldsymbol{\eta}\}^T \{\ {}^{n}\boldsymbol{\sigma}\} d^{n}V = {}^{n+1}\mathfrak{R} \\ - \int_{{}^{n}V} \left(\{\delta_n \boldsymbol{\gamma}\}^T \{\ {}^{n}\boldsymbol{\sigma}\} \right) d\,{}^{n}V \end{aligned} \tag{2.70}$$

where $\{\delta_n \boldsymbol{\eta}\}^T = \{\delta_n \eta_{11} \quad \delta_n \eta_{22} \quad 2\delta_n \eta_{12} \quad 0 \quad 0 \quad 0\}$ and the arrangements of stresses and strains are according to Eqn. 2.49.

In the derivation of the elastoplastic constitutive relationship, we considered the corotational stress and strain rates. In order to introduce the correct constitutive relation discussed earlier, we consider the relation between the PK2 stresses and the Cauchy stress

$${}^{n+1}_{n}\boldsymbol{S} = {}^{n+1}_{n}J\ {}^{n+1}_{n}\boldsymbol{F}^{-1} \cdot {}^{n+1}\boldsymbol{S} \cdot {}^{n+1}_{n}\boldsymbol{F}^{-T} \tag{2.71a}$$

$${}^{n+1}_{n}\boldsymbol{T} = {}^{n+1}_{n}J\ {}^{n+1}_{n}\boldsymbol{F}^{-1} \cdot {}^{n+1}\boldsymbol{T} \cdot {}^{n+1}_{n}\boldsymbol{F}^{-T} \tag{2.71b}$$

$${}^{n+1}_{n}\boldsymbol{M} = {}^{n+1}_{n}J\ {}^{n+1}_{n}\boldsymbol{F}^{-1} \cdot {}^{n+1}\boldsymbol{M} \cdot {}^{n+1}_{n}\boldsymbol{F}^{-T} \tag{2.71c}$$

where the Jacobian from frame n to $n+1$ is

$$ {}^{n+1}_{n}J = \det\left({}^{n+1}_{n}\boldsymbol{F}\right) > 0 \tag{2.72} $$

and the deformation gradient is

$$ {}^{n+1}_{n}\boldsymbol{F} = \frac{\partial\ {}^{n+1}\boldsymbol{x}}{\partial\ {}^{n}\boldsymbol{x}} \tag{2.73} $$

Considering the following relation from continuum mechanics,

$$ {}^{n+1}_{n}\dot{J} = {}^{n+1}_{n}J\ \mathrm{div}(\ {}^{n+1}\boldsymbol{L}) = {}^{n+1}_{n}J\ {}^{n+1}L_{kk} \tag{2.74} $$

where the velocity gradient ${}^{n+1}\boldsymbol{L}$ is

$$ {}^{n+1}\boldsymbol{L} = \frac{\partial\ {}^{n+1}\dot{\boldsymbol{u}}}{\partial\ {}^{n+1}\boldsymbol{x}} \qquad \text{and} \qquad {}^{n+1}_{n}\dot{\boldsymbol{F}}^{-1} = -\ {}^{n+1}_{n}\boldsymbol{F}^{-1}\ {}^{n+1}\boldsymbol{L} \tag{2.75} $$

the rate form of Eqn. 2.71 results in

$$ {}^{n+1}_{n}\dot{\boldsymbol{S}} = {}^{n+1}_{n}J\ {}^{n+1}_{n}\boldsymbol{F}^{-1}\cdot\ {}^{n+1}\boldsymbol{S}^{\nabla\ T}\cdot\ {}^{n+1}_{n}\boldsymbol{F}^{-T} \tag{2.76a} $$

$$ {}^{n+1}_{n}\dot{\boldsymbol{T}} = {}^{n+1}_{n}J\ {}^{n+1}_{n}\boldsymbol{F}^{-1}\cdot\ {}^{n+1}\boldsymbol{T}^{\nabla\ T}\cdot\ {}^{n+1}_{n}\boldsymbol{F}^{-T} \tag{2.76b} $$

$$ {}^{n+1}_{n}\dot{\boldsymbol{M}} = {}^{n+1}_{n}J\ {}^{n+1}_{n}\boldsymbol{F}^{-1}\cdot\ {}^{n+1}\boldsymbol{M}^{\nabla\ T}\cdot\ {}^{n+1}_{n}\boldsymbol{F}^{-T} \tag{2.76c} $$

The notation $(\ \ )^{\nabla\ T}$ indicates the Truesdell rate of Cauchy stresses

$$ {}^{n+1}\boldsymbol{S}^{\nabla\ T} = {}^{n+1}\dot{\boldsymbol{S}} + \mathrm{div}(\ {}^{n+1}\boldsymbol{L})\ {}^{n+1}\boldsymbol{S} - {}^{n+1}\boldsymbol{L}\cdot\ {}^{n+1}\boldsymbol{S} - {}^{n+1}\boldsymbol{S}\cdot\ {}^{n+1}\boldsymbol{L}^{T} \tag{2.77a} $$

$$ {}^{n+1}\boldsymbol{T}^{\nabla\ T} = {}^{n+1}\dot{\boldsymbol{T}} + \mathrm{div}(\ {}^{n+1}\boldsymbol{L})\ {}^{n+1}\boldsymbol{T} - {}^{n+1}\boldsymbol{L}\cdot\ {}^{n+1}\boldsymbol{T} - {}^{n+1}\boldsymbol{T}\cdot\ {}^{n+1}\boldsymbol{L}^{T} \tag{2.77b} $$

$$ {}^{n+1}\boldsymbol{M}^{\nabla\ T} = {}^{n+1}\dot{\boldsymbol{M}} + \mathrm{div}(\ {}^{n+1}\boldsymbol{L})\ {}^{n+1}\boldsymbol{M} - {}^{n+1}\boldsymbol{L}\cdot\ {}^{n+1}\boldsymbol{M} - {}^{n+1}\boldsymbol{M}\cdot\ {}^{n+1}\boldsymbol{L}^{T} \tag{2.77c} $$

Next we consider the constitutive relationship defined in Eqn. 2.57 to be in terms of the corotational rate of Cauchy stresses. Substituting this into Eqn. 2.77 results in

$$\begin{Bmatrix} {}^{n+1}\boldsymbol{S}^{\nabla\ T} \\ {}^{n+1}\boldsymbol{T}^{\nabla\ T} \\ {}^{n+1}\boldsymbol{M}^{\nabla\ T} \end{Bmatrix} = \begin{bmatrix} \mathbb{L}^{ep} & \mathbb{M}^{ep} & \mathbb{N}^{ep} \\ (\mathbb{M}^{ep})^T & \mathbb{H}^{ep} & \mathbb{Q}^{ep} \\ (\mathbb{N}^{ep})^T & (\mathbb{Q}^{ep})^T & \mathbb{D}^{ep} \end{bmatrix} : \begin{Bmatrix} {}^{n+1}\dot{\boldsymbol{e}} \\ {}^{n+1}\dot{\boldsymbol{A}} \\ {}^{n+1}\dot{\boldsymbol{K}} \end{Bmatrix}$$
$$+\mathrm{div}({}^{n+1}\boldsymbol{L}) \begin{Bmatrix} {}^{n+1}\boldsymbol{S} \\ {}^{n+1}\boldsymbol{T} \\ {}^{n+1}\boldsymbol{M} \end{Bmatrix} - ({}^{n+1}\boldsymbol{L} - {}^{n+1}\boldsymbol{\Omega}) \cdot \begin{Bmatrix} {}^{n+1}\boldsymbol{S} \\ {}^{n+1}\boldsymbol{T} \\ {}^{n+1}\boldsymbol{M} \end{Bmatrix} \tag{2.78}$$
$$- \begin{Bmatrix} {}^{n+1}\boldsymbol{S} \\ {}^{n+1}\boldsymbol{T} \\ {}^{n+1}\boldsymbol{M} \end{Bmatrix} \cdot ({}^{n+1}\boldsymbol{L}^T - {}^{n+1}\boldsymbol{\Omega}^T)$$

In the linearized principle of virtual displacement expression (Eqn. 2.69 or 2.70), the incremental change in PK2 stresses and couple stresses can be expressed as

$${}_n\boldsymbol{S} = \Delta\boldsymbol{S} = \int_{t_n}^{t_{n+1}} {}^{\tau}_{n}\dot{\boldsymbol{S}} d\tau = \int_{t_n}^{t_{n+1}} \left({}^{\tau}_{n}J\ {}^{\tau}_{n}\boldsymbol{F}^{-1} \cdot\ {}^{\tau}\boldsymbol{S}^{\nabla\ T} \cdot\ {}^{\tau}_{n}\boldsymbol{F}^{-T} \right) d\tau \approx\ {}^{n}\boldsymbol{S}^{\nabla\ T}\Delta t \tag{2.79a}$$

$${}_n\boldsymbol{T} = \Delta\boldsymbol{T} = \int_{t_n}^{t_{n+1}} {}^{\tau}_{n}\dot{\boldsymbol{T}} d\tau = \int_{t_n}^{t_{n+1}} \left({}^{\tau}_{n}J\ {}^{\tau}_{n}\boldsymbol{F}^{-1} \cdot\ {}^{\tau}\boldsymbol{T}^{\nabla\ T} \cdot\ {}^{\tau}_{n}\boldsymbol{F}^{-T} \right) d\tau \approx\ {}^{n}\boldsymbol{T}^{\nabla\ T}\Delta t \tag{2.79b}$$

$${}_n\boldsymbol{M} = \Delta\boldsymbol{M} = \int_{t_n}^{t_{n+1}} {}^{\tau}_{n}\dot{\boldsymbol{M}} d\tau = \int_{t_n}^{t_{n+1}} \left({}^{\tau}_{n}J\ {}^{\tau}_{n}\boldsymbol{F}^{-1} \cdot\ {}^{\tau}\boldsymbol{M}^{\nabla\ T} \cdot\ {}^{\tau}_{n}\boldsymbol{F}^{-T} \right) d\tau \approx\ {}^{n}\boldsymbol{M}^{\nabla\ T}\Delta t \tag{2.79c}$$

where for a sufficiently small subinterval $\Delta t = t_{n+1} - t_n$, the integrals are approximated

with a single left hand integration point. Similarly,

$$ {}_n\boldsymbol{e} = \Delta\boldsymbol{e} = \int_{t_n}^{t_{n+1}} {}_n^{\tau}\dot{\boldsymbol{e}} dt \approx {}^n\dot{\boldsymbol{e}}\Delta t \tag{2.80a} $$

$$ {}_n\boldsymbol{A} = \Delta\boldsymbol{A} = \int_{t_n}^{t_{n+1}} {}_n^{\tau}\dot{\boldsymbol{A}} dt \approx {}^n\dot{\boldsymbol{A}}\Delta t \tag{2.80b} $$

$$ {}_n\boldsymbol{K} = \Delta\boldsymbol{K} = \int_{t_n}^{t_{n+1}} {}_n^{\tau}\dot{\boldsymbol{K}} dt \approx {}^n\dot{\boldsymbol{K}}\Delta t \tag{2.80c} $$

As a result, in 2D, the incremental PK2 stresses can be represented as

$$ \{\ {}_n\boldsymbol{\sigma}\} = ([\ {}_n\boldsymbol{C}^{ep}] + [\ {}_n\boldsymbol{C}^{\sigma}])\,\{\ {}_n\boldsymbol{\gamma}\} \tag{2.81} $$

where

$$ [\ {}_n\boldsymbol{C}^{\sigma}] = \begin{bmatrix} -{}^nS_{11} & {}^nS_{11} & -{}^nS_{12} & {}^nS_{12} & 0 & 0 \\ {}^nS_{22} & -{}^nS_{22} & -{}^nS_{12} & -{}^nS_{12} & 0 & 0 \\ 0 & 0 & -\frac{1}{2}\left({}^nS_{11} + {}^n\,S_{22}\right) & -\frac{1}{2}\left({}^nS_{11} - {}^n\,S_{22}\right) & 0 & 0 \\ 0 & 0 & 0 & 0 & 0 & 0 \\ 0 & {}^nM_{13} & -\frac{1}{2}{}^nM_{23} & \frac{1}{2}{}^nM_{23} & 0 & 0 \\ {}^nM_{23} & 0 & -\frac{1}{2}{}^nM_{13} & -\frac{1}{2}{}^nM_{13} & 0 & 0 \end{bmatrix} \tag{2.82} $$

and $[\ {}_n\boldsymbol{C}^{ep}]$ corresponds to the micropolar elastoplastic stiffness at time step n. The corresponding principle of virtual displacement is

$$ \begin{aligned} \int_{{}^nV} \{\delta_n\boldsymbol{\gamma}\}^T ([\ {}_n\boldsymbol{C}^{ep}] + [\ {}_n\boldsymbol{C}^{\sigma}])\,\{\ {}_n\boldsymbol{\gamma}\} d\ {}^nV + \int_{{}^nV} (\{\delta_n\boldsymbol{\eta}\}^T\{\ {}^n\boldsymbol{\sigma}\} d^nV = \ {}^{n+1}\mathfrak{R} \\ - \int_{{}^nV} \left(\{\delta_n\boldsymbol{\gamma}\}^T\{\ {}^n\boldsymbol{\sigma}\}\right) d\ {}^nV \end{aligned} \tag{2.83} $$

where it will be reduced into a finite element form.

2.7 Finite Element Discretization

In this section, the finite element discretization of the micropolar nonlinear equations is discussed. Again, restricting our attention to a 2D deformation in the (x_1, x_2) plane, the displacement and rotation increments in Eqn. 2.64b,c are expressed as

$$u_1 = \sum_{j=1}^{4} N_j u_1^{(j)} \tag{2.84a}$$

$$u_2 = \sum_{j=1}^{4} N_j u_2^{(j)} \tag{2.84b}$$

$$\varphi_3 = \sum_{j=1}^{4} N_j \varphi_3^{(j)} \tag{2.84c}$$

where

$$N_1(r,s) = \frac{1}{4}(1+r)(1+s) \tag{2.85a}$$

$$N_2(r,s) = \frac{1}{4}(1-r)(1+s) \tag{2.85b}$$

$$N_3(r,s) = \frac{1}{4}(1-r)(1-s) \tag{2.85c}$$

$$N_4(r,s) = \frac{1}{4}(1+r)(1-s) \tag{2.85d}$$

are the element shape functions defined in the isoparametric coordinates (r, s) and they assume a value of 1 at node (j) and a value of 0 at the remaining nodes. $u_1^{(j)}, u_1^{(j)}$, and $\varphi_3^{(j)}$ are the corresponding nodal displacements and rotations. In the above representation, a 4-noded quadrilateral element, with 4 Gauss integration points is considered, as shown in Fig. 2.4. In this formulation, each node in the micropolar continuum has both displacement and rotational degrees of freedom.

In finite element form, the strain increment vector is defined as

$$\{ {}_n\boldsymbol{\gamma}\} = [{}^n_n\boldsymbol{B}_L]\{\boldsymbol{q}\} \tag{2.86}$$

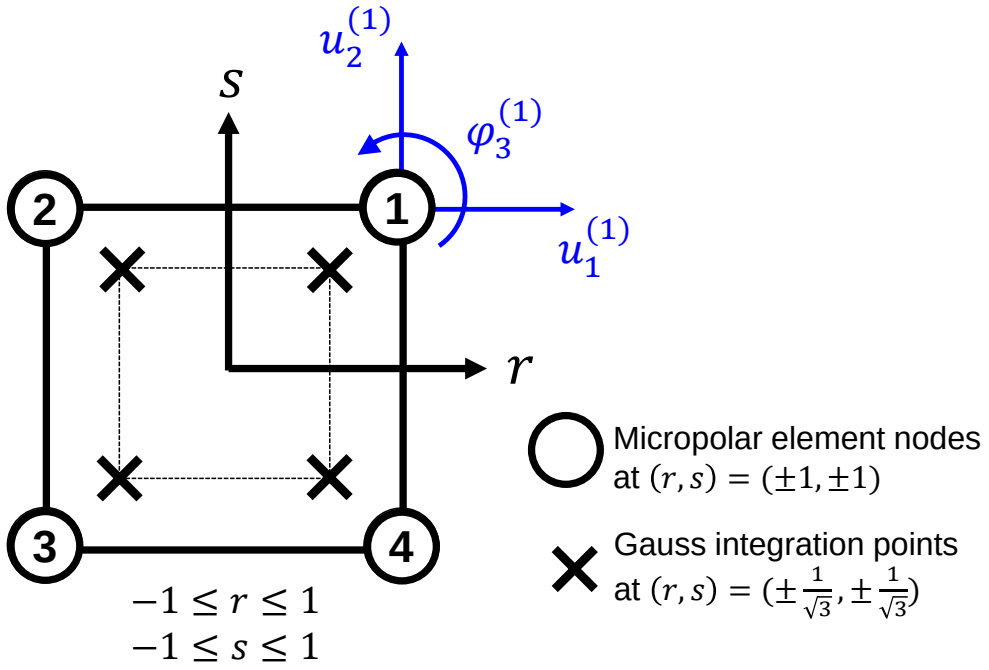

Figure 2.4: Isoparametric representation of a 4-noded micropolar quadrilateral element.

where $[\,{}^{n}_{n}\boldsymbol{B}_L]$, defined in Appendix B, is the transformation matrix relating the incremental strains to the incremental changes in nodal displacements and the rotations $\{\boldsymbol{q}\}$, which is arranged as

$$\{\boldsymbol{q}\} = \{u_1^{(1)} \quad u_2^{(1)} \quad \varphi_3^{(1)} \quad \cdots \quad u_1^{(4)} \quad u_2^{(4)} \quad \varphi_3^{(4)}\}^T \tag{2.87}$$

Under this discretization, the principle of virtual displacement in Eqn. 2.83 simplifies in a finite element form

$$([\,{}^{n}_{n}\boldsymbol{K}_L] + [\,{}^{n}_{n}\boldsymbol{K}_{NL}])\,\{\boldsymbol{q}\} = \{\,{}^{n+1}\boldsymbol{R}\} - \{\,{}^{n}_{n}\boldsymbol{F}\} \tag{2.88}$$

where $\{\,{}^{n+1}\boldsymbol{R}\}$ is the vector of externally applied nodal point loads at step $n+1$ and $\{\,{}^{n}_{n}\boldsymbol{F}\}$ is the vector of nodal forces equivalent to the element stresses (or residual stresses) at time n. In the above expressions, $[\,{}^{n}_{n}\boldsymbol{K}_L]$ is the incremental stiffness matrix corresponding to the linear part of the strain $\{{}_n\boldsymbol{\gamma}\}$ and $[\,{}^{n}_{n}\boldsymbol{K}_{NL}]$ is the contribution to

the stiffness from the geometric nonlinear part $\{{}_n\boldsymbol{\eta}\}$. The expressions of each of these stiffness matrices and force vectors defined are given in Appendix B. The solution to the linear algebraic equations is the vector $\{\boldsymbol{q}\}$. In this analysis, we assume the micropolar continuum is subjected to a proportionally varying load. In this case, the equations to be solved are

$$([\,{}^{n}_{n}\boldsymbol{K}_L] + [\,{}^{n}_{n}\boldsymbol{K}_{NL}])\,\{\boldsymbol{q}\} = {}^{n+1}\lambda\{\,{}^{n+1}\boldsymbol{R}\} - \{\,{}^{n}_{n}\boldsymbol{F}\} \tag{2.89}$$

where ${}^{n+1}\lambda$ is the load factor that describes the intensity of the reference load vector $\{\,{}^{n+1}\boldsymbol{R}\}$ to be applied at step $n+1$. The solution scheme is based on an incremental implicit arc-length method (Riks method) in order to capture unstable equilibrium paths, such as a snap-back response, which is associated with fiber kinking. After solving for $\{\boldsymbol{q}\}$, the total nodal displacements and rotation are updated as

$$\{\,{}^{n+1}\boldsymbol{q}\} = \{\,{}^{n}\boldsymbol{q}\} + \{\boldsymbol{q}\} \tag{2.90}$$

where $\{\,{}^{n}\boldsymbol{q}\}$ is the total nodal unknowns at step n. In addition, at the end of the increment Δt, the Cauchy stresses and couple-stress at step $n+1$ are updated as

$${}^{n+1}\boldsymbol{S} \approx {}^{n}\boldsymbol{S} + {}^{n+1}\dot{\boldsymbol{S}}\Delta t \tag{2.91a}$$

$${}^{n+1}\boldsymbol{T} \approx {}^{n}\boldsymbol{T} + {}^{n+1}\dot{\boldsymbol{T}}\Delta t \tag{2.91b}$$

$${}^{n+1}\boldsymbol{M} \approx {}^{n}\boldsymbol{M} + {}^{n+1}\dot{\boldsymbol{M}}\Delta t \tag{2.91c}$$

which are stored as state variables to be utilized in the next time increment. The finite element formulation is implemented in a Fortran based user element (UEL) subroutine, with the commercial software ABAQUS.

2.8 Results and Discussion

Based on the nonlinear formulation above, the utility of the continuum model is demonstrated by simulating the kinking behavior of a homogenized fiber reinforced composite. In proceeding, the micromechanics boundary value problem in [48], of a unidirectional fiber composite is considered. The homogenized boundary value problem is shown in Fig 2.5. The anisotropic domain has dimensions $L_x = 2.0mm$ and $L_y = 0.9mm$, with the fibers assumed to be aligned along the x_1-direction, with an initial geometric imperfection of 1-degree. Both geometric and material nonlinearity are included in the analysis and due to the presence of the initial imperfection, the compressive load induces an axial-shear coupling. This leads to a limit point structural instability.

This is in contrast to previous studies of localization ([41], [46], etc.), where a softening (negative tangent stiffness) is introduced in the constitutive relation. When the stiffness ceases to be positive definite at the descending stress-strain curve, instabilities and bifurcations arise, which lead to localization. However, this abstraction of a material model is in violation of Drucker stability criterion (positive definite constitutive relation) for a nonlinear continuous material. Although a softening relation is sufficient for localization to be induced, it will be shown to be unnecessary. Instead, its formation can be modeled as a structural instability at the micropolar continuum scale.

The boundary conditions are: (a) on $x_1 = 0$, $u_1 = 0$ while being unconstrained along x_2-direction, (b) the inclined edges along $x_2 = 0,\ L_y$ are traction and couple-traction free, or $\boldsymbol{t} = 0$ and $\boldsymbol{Q} = 0$, respectively, and (c) compression load $u_1 = -\Delta$ is applied along the edge $x_1 = L_x$, while unconstrained along u_2-direction. (d) The origin $x_1 = x_2 = 0$ is set $u_1 = u_2 = 0$ to avoid rigid body rotation. In literature, the these boundary conditions have been shown to best be representative of the infinite-domain assumption for fiber kinking, while minimizing the influence of the boundary.

Because the topic of the this study is the effect of micropolarity and the additional material constants that are introduced, convergence studies demonstrating the validity of the boundary conditions will not be discussed. In addition, the micromechanics analysis and the determination of these micropolar material constants of fiber reinforced composites are discussed in the next section, which are presently ignored. The classical, effective linear anisotropic material properties considered are shown in Table 2.1, where the corresponding values of $\hat{C}_{ij}$ can be found from Eqn. 2.29.

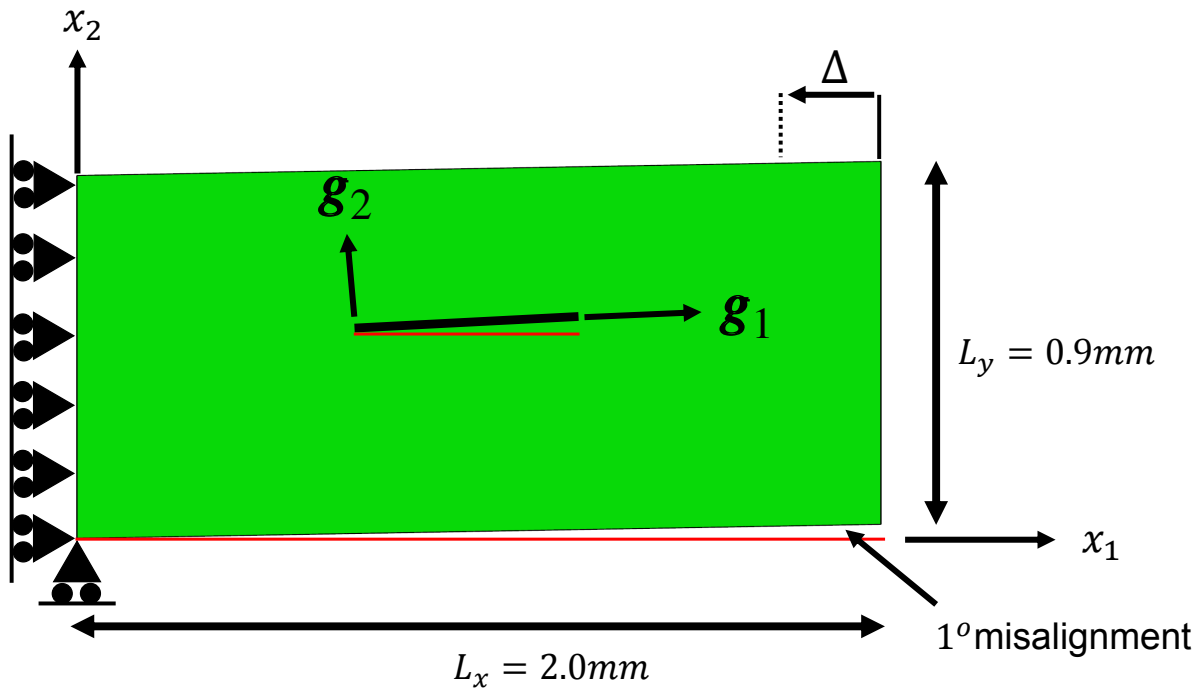

Figure 2.5: Schematic of the equivalent micropolar continuum boundary value problem.

Table 2.1: Effective elastic composite properties.

$\hat{E}_{11}$ (GPa)	$\hat{E}_{22}$ (GPa)	$\hat{E}_{33}$ (GPa)	$\hat{G}_{12}$ (GPa)	$\hat{G}_{13}$ (GPa)	$\hat{G}_{23}$ (GPa)	$\hat{v}_{12}$	$\hat{v}_{13}$	$\hat{v}_{23}$
120.43	7.50	7.50	2.40	2.40	2.07	0.40	0.40	0.76

Because the fibers are locally aligned along the $\hat{\boldsymbol{g}}_1$-direction, the bending resistance perpendicular to it is neglected $\left(\hat{C}_{66} = 0\right)$. Since the micropolar length scale

is introduced through the constant $\hat{C}_{55}$, which has a dimension of $stress \times length^2$, it is convenient to express it as $\hat{C}_{55} = 2\hat{G}_{12}l^2$, where l is the characteristic length of the microstructure of the composite, which will be considered to be the fiber diameter. Because in this boundary value problem the yielding is dominated by compression and shearing, for simplicity, the relevant nonzero coefficients in the yielding criterion Eqn. 2.32 are chosen $\overline{F} = 1$ and $\overline{N} = 4.17$. The hardening relation between the equivalent stress and strain is shown in Fig. 2.6. It should be noted that a softening relation is not introduced, which is in contrast to localization studies commonly found in literature, such as in [41], [46], etc.

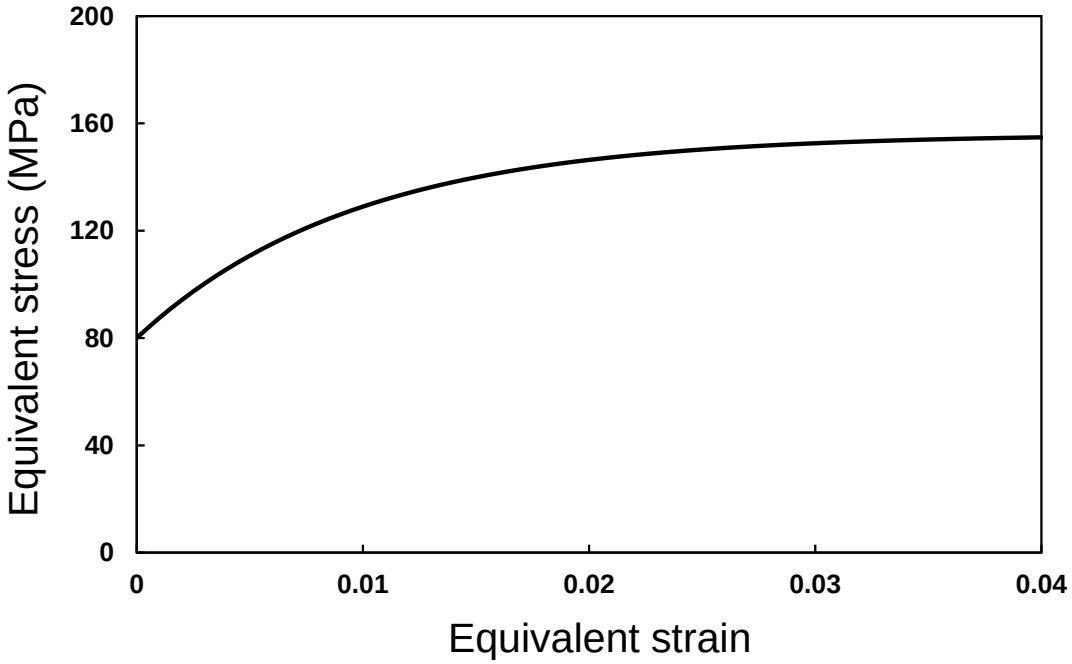

Figure 2.6: Equivalent stress (σ_e) vs equivalent strain (ε_p) relation.

In order to clarify the effects of the micropolar constants $\hat{C}_{34}, \hat{C}_{44}, \hat{C}_{55}$, we will consider the two cases: (1) $\hat{C}_{34} = \hat{C}_{44} = 0$, and $\hat{C}_{55} \neq 0$ for analyzing the effect of the characteristic length l and (2) $\hat{C}_{34}, \hat{C}_{44}, \hat{C}_{55} \neq 0$, in order to bring about the effect of the additional shear moduli. It should be noted that in case (1), because the shear moduli are neglected, this corresponds to the results of the well known

couple-stress theory, where the stress and strain tensors are symmetric [40]. Fig. 2.7 shows the results for different fiber diameter along with different mesh sizes (9×21 and 18×41). The characteristic lengths chosen are $l = 0\mu m$, which corresponds to classical elasticity, $l = 6\mu m$, which is a realistic value of the fiber diameter that is found in engineering manufactured fiber composites, and in the extreme case of $l = 100\mu m$. In the macroscopic stress-strain response of the structure, it is observed that as the fiber diameter is increased, the peak load also increases. Physically, this is due to the local increase of the bending stiffness of the fibers, which in turn increases the microbuckling load. This is a so-called length scale effect not captured in the classical macroscopic models. In addition, the formation of localization of the plastic strain ε_p in the snap-back region is shown in (a)-(f). In the Cauchy model (green), in the post-peak region, the localization is mesh-dependent and the plastic deformation is limited to only a single column of elements (localization angle is zero). The localization width is seen to be proportional to the magnitude of the characteristic length. As a result, the degree to which the model is mesh-independent is a function of the characteristic length l, or $\hat{C}_{55}$. As mentioned earlier, this parameter increases the order of the Laplacian operator of the governing equations, which prevents a loss in ellipticity.

Next, the effects of the shear moduli $\hat{C}_{34}$ and $\hat{C}_{44}$ are analyzed. The values considered for them are $\hat{C}_{34} = \hat{G}_{12}/24$ and $\hat{C}_{44} = \hat{G}_{12}/8$. In the micropolar theory discussed above, the presence of these moduli introduces asymmetry in the stress and strain tensors. In an anisotropic microstructure, since the fibers are aligned along a single direction, when a simple shear load is applied perpendicular to the fibers, the resistance is expected to be stiffer compared to the shear load applied parallel to the fibers. In a Cauchy continuum, these higher order shear effect of anisotropic materials is not captured and further details regarding the physical meaning of these additional moduli is discussed in the later chapter of the thesis.

The results of localization with nonzero shear moduli is shown in Fig. 2.8. Unlike the micropolar characteristic length l (or $\hat{C}_{55}$), the shear moduli have a knockdown factor on the peak load. In addition, compared to the Cauchy continuum results in Fig. 2.7, the localization is again not limited to a single element. These material constants are also observed to have an effect on the localization angle.

2.9 Conclusion

This chapter focused on the development of an anisotropic nonlinear micropolar theory, for application to fiber reinforced composites. Both geometric and physical nonlinearities were considered. The material nonlinearity was based on the anisotropic elastoplastic Hill's criterion. In addition, the nonlinear finite element formulation of the these equations was discussed. To demonstrate the advantage of micropolar theory in capturing length scale effects, it was applied towards studying localization, or fiber kinking. Unlike previous works in this area, a softening relation in the equivalent stress-strain relation was not introduced. The effects of the additional micropolar material constants were analyzed. The material property $\hat{C}_{55}$ was shown to influence the localization width, while the additional micropolar shear moduli had an effect on the localization angle. In the next section, the determination of these material constants is discussed, along with comparison of the results to an exact micromechanics based Cauchy continuum model.

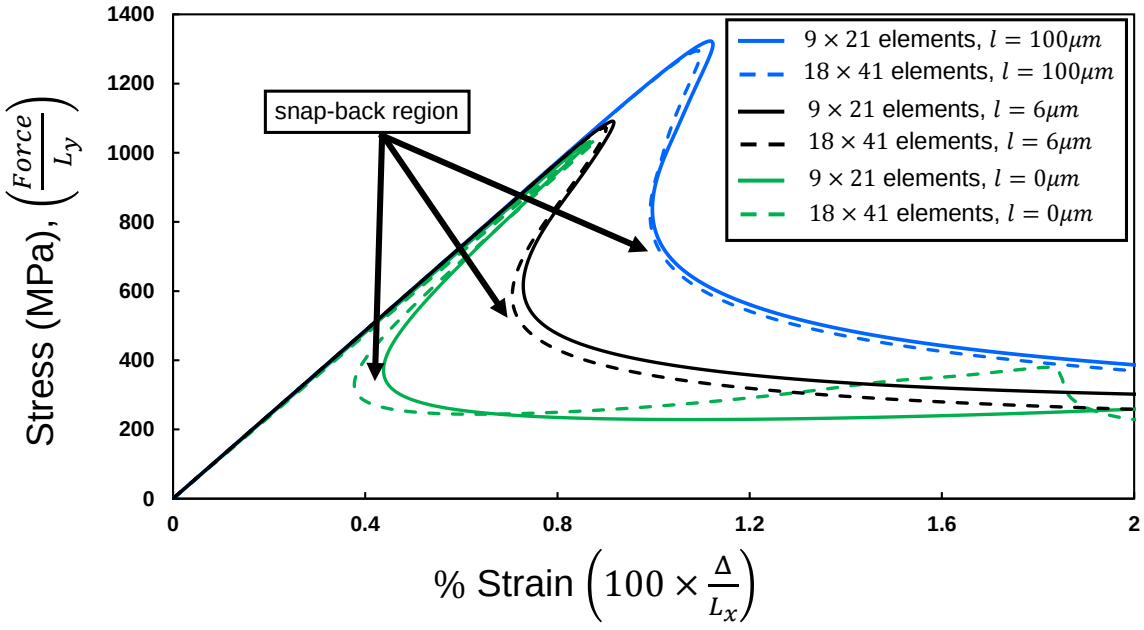

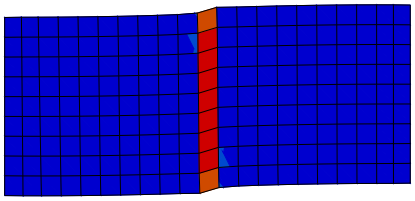

(a) 9×21 element, $l = 0\mu m$

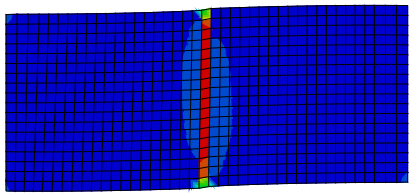

(b) 18×41 element, $l = 0\mu m$

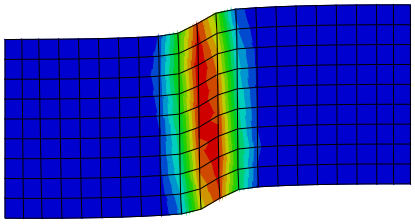

(c) 9×21 element, $l = 6\mu m$

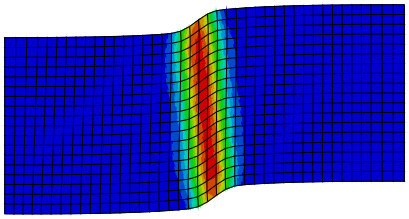

(d) 18×41 element, $l = 6\mu m$

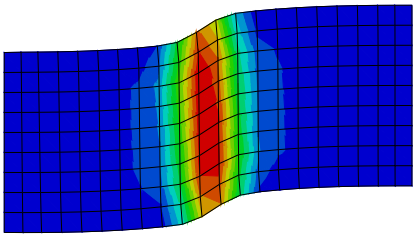

(e) 9×21 element, $l = 100\mu m$

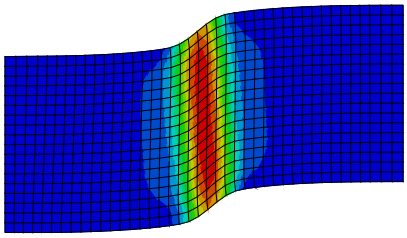

(f) 18×41 element, $l = 100\mu m$

Figure 2.7: Effects of the parameter $\hat{C}_{55}$, or l, on the macroscopic stress-strain response and the formation of localization for different meshes.

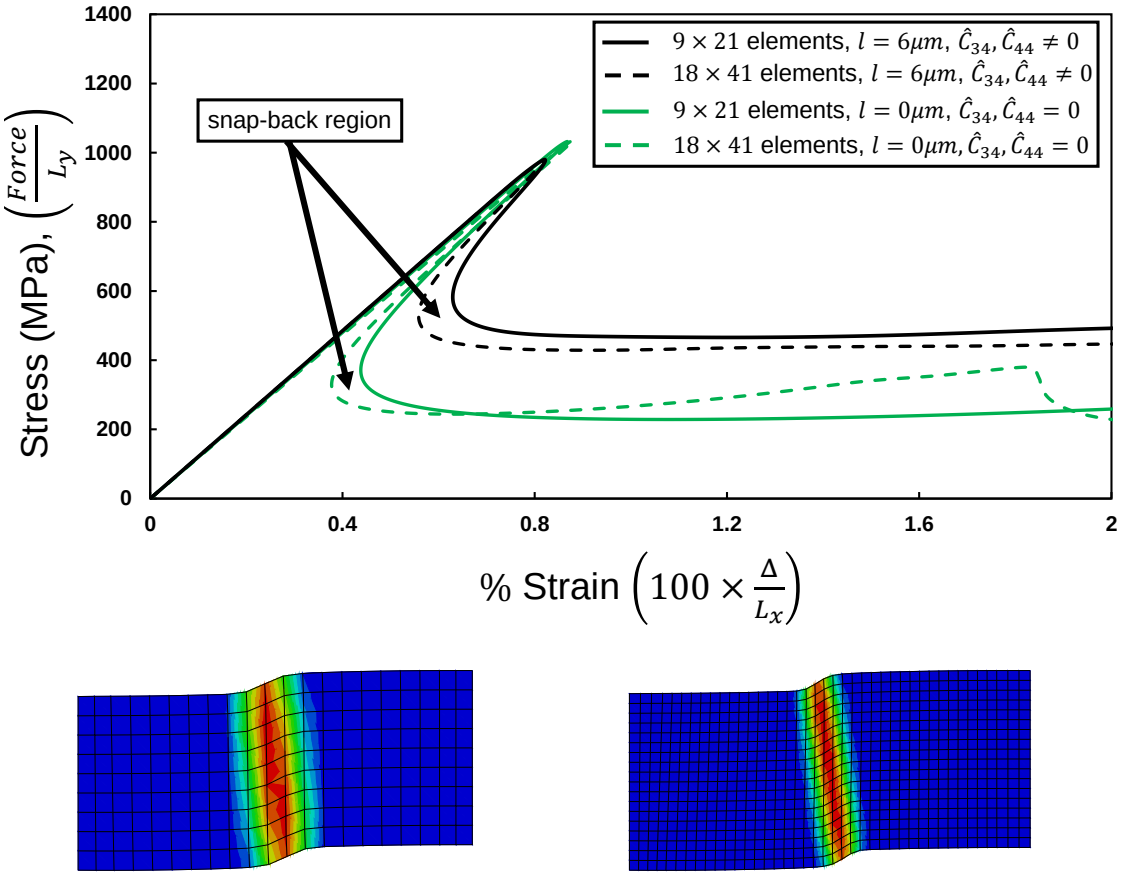

(a) 9×21 element, $l = 6\mu m$, $\hat{C}_{34}, \hat{C}_{44} \neq 0$ (b) 18×41 element, $l = 6\mu m$, $\hat{C}_{34}, \hat{C}_{44} \neq 0$

Figure 2.8: Effects of the shear moduli $\hat{C}_{34}, \hat{C}_{44}$ on the macroscopic stress-strain response and the formation of localization for different meshes.

CHAPTER 3

Micromechanics vs Micropolar Continuum Comparison

3.1 Introduction

In general, fiber reinforced composites consist of transversely-isotropic fibers, surrounded by an isotropic polymer matrix material. The interaction of these micro-constituents exhibit complex mechanical behavior at the macroscale. The analysis of these composites has often relied on modeling these materials by treating the constituents as effective materials (macromechanics approach). However, in this approach, details regarding the geometric and structural features of the constituents are lost. This becomes problematic when attempting to analyze and predict failure mechanisms, where the geometry of the microstructure and the imperfections associated with them have significant effect on the load bearing capacity of the material [22]. For accurate predictions, the most reliable models are those that explicitly consider fiber and matrix constituents of the composite (micromechanics approach) [49]. Unlike the macromechanics approach, these models provide more physical insight regarding the failure of the fiber and the matrix, as well as the load transfer between the two [50], [51]. The micromechanics approach is advantageous in accurately predicting the behavior of the composite, but is costly in computational time due to the large number of degrees of freedom associated with the model. Because of this, resorting to

continuum models is often more practical. In the previous section, it was shown that in modeling strain localization, the classical continuum approach is limited due to the absence of an appropriate internal "length scale." This causes a loss in ellipticity of the governing equations at the onset of failure, which leads to results that are a function of the mesh size. A higher order micropolar theory was shown to remedy this.

In this chapter, we proceed with the nonlinear micropolar model developed to compare the continuum predictions with the exact, micromechanics model. In literature, one of the challenges of micropolar theory has been the determination of these additional material constants. With the introduction of couple-stresses and curvatures, new material properties are introduced. In this section, new physics based methods of determining these additional constants is discussed, which provides insight to their physical meaning.

The constitutive relationship of a 2D transversely-isotropic micropolar material is restated below for convenience

$$\begin{Bmatrix} \hat{\Sigma}_{11} \\ \hat{\Sigma}_{22} \\ \hat{\Sigma}_{12} \\ \hat{\Sigma}_{21} \\ \hat{M}_{13} \\ \hat{M}_{23} \end{Bmatrix} = \begin{bmatrix} \hat{\mathbb{C}}_{1111} & \hat{\mathbb{C}}_{1122} & 0 & 0 & 0 & 0 \\ \hat{\mathbb{C}}_{1122} & \hat{\mathbb{C}}_{2222} & 0 & 0 & 0 & 0 \\ 0 & 0 & \hat{\mathbb{C}}_{1212} & \hat{\mathbb{C}}_{1221} & 0 & 0 \\ 0 & 0 & \hat{\mathbb{C}}_{1221} & \hat{\mathbb{C}}_{2121} & 0 & 0 \\ 0 & 0 & 0 & 0 & \hat{\mathbb{D}}_{1313} & 0 \\ 0 & 0 & 0 & 0 & 0 & \hat{\mathbb{D}}_{2323} \end{bmatrix} \begin{Bmatrix} \hat{\Gamma}_{11} \\ \hat{\Gamma}_{22} \\ \hat{\Gamma}_{12} \\ \hat{\Gamma}_{21} \\ \hat{K}_{13} \\ \hat{K}_{23} \end{Bmatrix} \tag{3.1}$$

The out-of-plane nonzero stress associated with planar deformation (plane strain) is

$$\hat{\Sigma}_{33} = \hat{\mathbb{C}}_{1122}\hat{\Gamma}_{11} + \hat{\mathbb{C}}_{2233}\hat{\Gamma}_{22} \tag{3.2}$$

In terms of the symmetric and skew-symmetric stress and strain components, the

constitutive relationship is expressed as

$$\begin{Bmatrix} \hat{S}_{11} \\ \hat{S}_{22} \\ \hat{S}_{12} \\ \hat{T}_{12} \\ \hat{M}_{13} \\ \hat{M}_{23} \end{Bmatrix} = \begin{bmatrix} \hat{C}_{11} & \hat{C}_{12} & 0 & 0 & 0 & 0 \\ \hat{C}_{12} & \hat{C}_{22} & 0 & 0 & 0 & 0 \\ 0 & 0 & \hat{C}_{33} & \hat{C}_{34} & 0 & 0 \\ 0 & 0 & \hat{C}_{34} & \hat{C}_{44} & 0 & 0 \\ 0 & 0 & 0 & 0 & \hat{C}_{55} & 0 \\ 0 & 0 & 0 & 0 & 0 & \hat{C}_{66} \end{bmatrix} \begin{Bmatrix} \hat{e}_{11} \\ \hat{e}_{22} \\ 2\hat{e}_{12} \\ 2\hat{A}_{12} \\ \hat{K}_{13} \\ \hat{K}_{23} \end{Bmatrix} \tag{3.3}$$

with the out-of-plane stress being

$$\hat{S}_{33} = \hat{C}_{12}\hat{e}_{11} + \hat{C}_v\hat{e}_{22} \tag{3.4}$$

The $\hat{C}_{ij}$ constants in terms of $\hat{\mathbb{C}}_{ijkl}$ and $\hat{\mathbb{D}}_{ijkl}$ are

$$\hat{C}_{11} = \hat{\mathbb{C}}_{1111} \tag{3.5a}$$

$$\hat{C}_{22} = \hat{\mathbb{C}}_{2222} \tag{3.5b}$$

$$\hat{C}_{12} = \hat{\mathbb{C}}_{1122} \tag{3.5c}$$

$$\hat{C}_{33} = \frac{1}{4}(\hat{\mathbb{C}}_{1212} + 2\hat{\mathbb{C}}_{1221} + \hat{\mathbb{C}}_{2121}) \tag{3.5d}$$

$$\hat{C}_{44} = \hat{\mathbb{C}}_{1212} - 2\hat{\mathbb{C}}_{1221} + \hat{\mathbb{C}}_{2121} \tag{3.5e}$$

$$\hat{C}_{34} = \frac{1}{4}(\hat{\mathbb{C}}_{1212} - \hat{\mathbb{C}}_{2121}) \tag{3.5f}$$

$$\hat{C}_{55} = \hat{\mathbb{D}}_{1313} \tag{3.5g}$$

$$\hat{C}_{66} = \hat{\mathbb{D}}_{2323} \tag{3.5h}$$

$$\hat{C}_v = \hat{\mathbb{C}}_{2223} \tag{3.5i}$$

As discussed, these constants can be expressed in terms of the classical Young's moduli

$\hat{E}_{ij}$, Poisson's ratios $\hat{v}_{ij}$, and the shear modulus $\hat{G}_{12}$

$$\hat{C}_{11} = \frac{\hat{E}_{11}^2(\hat{v}_{23} - 1)}{\Lambda} \tag{3.6a}$$

$$\hat{C}_{12} = -\frac{\hat{E}_{11}\hat{E}_{22}\hat{v}_{12}}{\Lambda} \tag{3.6b}$$

$$\hat{C}_{22} = \frac{\hat{E}_{22}(\hat{E}_{22}\hat{v}_{12}^2 - \hat{E}_{11})}{\Lambda(1 + \hat{v}_{23})} \tag{3.6c}$$

$$\hat{C}_v = -\frac{\hat{E}_{22}(\hat{E}_{22}\hat{v}_{12}^2 + \hat{E}_{11}\hat{v}_{23})}{\Lambda(1 + \hat{v}_{23})} \tag{3.6d}$$

$$\hat{C}_{33} = \hat{G}_{12} \tag{3.6e}$$

where

$$\Lambda = 2\hat{E}_{22}\hat{v}_{12}^2 + \hat{E}_{11}(\hat{v}_{23} - 1) \tag{3.7}$$

It should be reiterated that the material constants are defined in a fiber-aligned coordinate system shown in Fig. 3.1. Following that, new material properties are in-

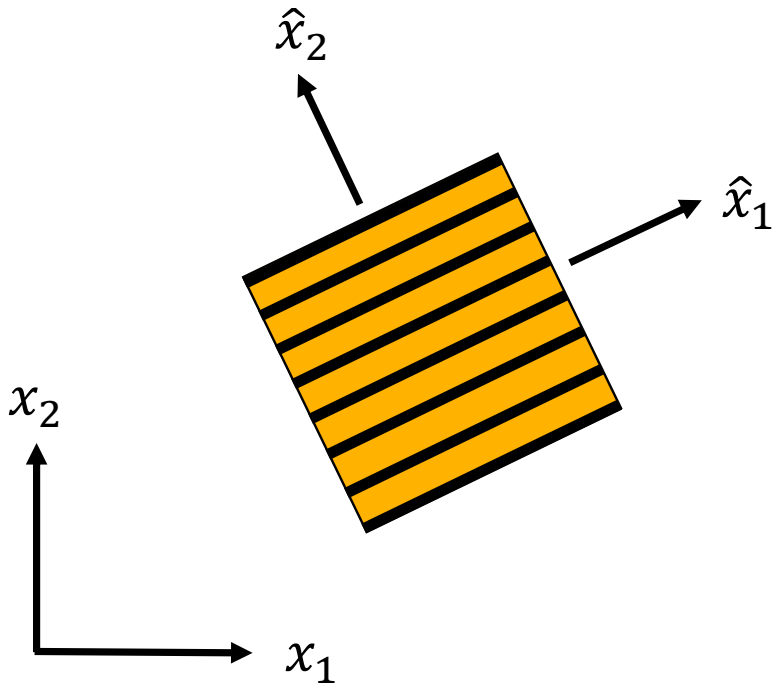

Figure 3.1: Fiber-aligned coordinates $\hat{x}_i$.

troduced. Unlike a classical continuum, there are 3 independent shear moduli present

($\hat{C}_{33},\ \hat{C}_{34},\ \hat{C}_{44}$ or $\hat{\mathbb{C}}_{1212},\ \hat{\mathbb{C}}_{1221},\ \hat{\mathbb{C}}_{2121}$). Physical meaning will be provided for these material constants and numerical tests are proposed to determine them, based on the application of simple shear along and perpendicular to the fiber directions. This differentiation of the shear deformation modes of a fiber reinforced composite is absent in a Cauchy continuum. In addition, 2 material constants are introduced from the moment-curvature relation ($\hat{\mathbb{C}}_{1313},\ \hat{\mathbb{C}}_{2323}$ or $\hat{C}_{55},\ \hat{C}_{66}$), which will be determined by generalizing the well known concentric cylinder model (CCM), by introducing the bending mode of the fibers. The effective linear and material nonlinear properties are determined based on the transversely-isotropic fiber and matrix properties provided in [3]. Based on these, the fiber-matrix kinking predictions will be compared to that of the micromechanics model.

3.2 Effective Properties of a Fiber Reinforced Composite

3.2.1 Concentric Cylinder Model (CCM)

In this section, the effective properties of a carbon fiber reinforced polymer matrix (CFRP) are discussed. The composite under consideration pertains of transversely-isotropic fibers and an isotropic matrix. The constituent materials are assumed to be Cauchy materials, however, the effective composite is modeled as a micropolar continuum. The fiber and matrix elastic properties reported in [3] will be considered. The fiber properties are given in Table 3.1.

Table 3.1: Transversely-isotropic fiber properties [3].

$\hat{E}^f_{11}$ (GPa)	$\hat{E}^f_{22}$ (GPa)	$\hat{E}^f_{33}$ (GPa)	$\hat{G}^f_{12}$ (GPa)	$\hat{G}^f_{13}$ (GPa)	$\hat{G}^f_{23}$ (GPa)	$\hat{v}^f_{12}$	$\hat{v}^f_{13}$	$\hat{v}^f_{23}$
276.0	8.76	8.76	12.0	12.0	3.24	0.35	0.35	0.35

The $\hat{x}_1$-direction is taken to be the fiber-aligned coordinate axes. The matrix

elastic modulus and Poisson's ratio are $E^m = 3.01$GPa and $v^m = 0.48$. Because the matrix layer is isotropic (properties independent of direction), the $\hat{(\,)}$ notation is disregarded.

With the given fiber and matrix properties, the effective classical properties are evaluated using the concentric cylinder model (CCM). In this approach, the fiber reinforced composite is assumed to be represented by concentric cylindrical fibers, surrounded by an outer cylindrical matrix layer. The radius of the outer matrix layer is taken so that the concentric cylinder has the same volume fraction as the composite under consideration. Based on a set of loading conditions on the concentric cylinders, the effective material constants are evaluated. The details of the CCM can be found in [52], and further application of it to fiber reinforced composites, in [53], [54]. The advantage of this approach is that it provides closed form expressions for the effective properties in terms of the fiber and the matrix properties, and the volume fraction. These closed form expressions are given in the Appendix C. By considering a fiber volume fraction $V^f = 0.50$ and the linear fiber and matrix properties mentioned earlier, the elastic properties of the composite are given in Table 3.2.

Table 3.2: Effective elastic composite properties.

$\hat{E}_{11}$ (GPa)	$\hat{E}_{22}$ (GPa)	$\hat{E}_{33}$ (GPa)	$\hat{G}_{12}$ (GPa)	$\hat{G}_{13}$ (GPa)	$\hat{G}_{23}$ (GPa)	$\hat{v}_{12}$	$\hat{v}_{13}$	$\hat{v}_{23}$
139.54	5.44	5.44	2.51	2.51	1.73	0.42	0.42	0.57

The values of $\hat{C}_{ij}$ can be found by direct substitution of the properties expressed above into Eqn. 3.6.

3.2.2 Micropolar Shear Properties

One of the challenges of higher order continuum theories, such as micropolar theory, is the determination of the addition material constants. In the recent decades, volume averaging methods have been developed for this purpose. For discrete cellular solids

and two-phase micropolar continuum medium, the determination of the effective micropolar properties using the generalized Hill-Mandel condition has been discussed in [55] and [56], respectively. However, for two-phase Cauchy continuum medium, these methods are inapplicable due to the inability to locally enforce an independent rotation degrees of freedom on the boundary of a representative volume element (RVE). For these systems, an approach by Forest and Sab [57] was proposed for periodic, heterogenous volume elements. As pointed out in [58], with the introduction of the higher order deformation modes, there is a loss of direct relation between the applied kinematic loads on the RVE and the macroscopic strains when volume averaging is applied. In the following analysis, to avoid these issues, we propose a physics-based approach to determining the micropolar constants of a fiber reinforced composite. The constants $\hat{C}_{34}$ and $\hat{C}_{44}$ are found by applying simple shear loads. Because the shear stress and strain tensors are asymmetric in a micropolar continuum, this fact is exploited by quantifying the difference in the simple shear responses of a fibreous volume element to determine these constants. In Eqn. 3.1, the constitutive relation relating the shear stresses $\hat{\Sigma}_{12}, \hat{\Sigma}_{21}$ to the strains $\hat{\Gamma}_{12}, \hat{\Gamma}_{21}$, shows that there are 3 independent material constants, $\hat{\mathbb{C}}_{1212}, \hat{\mathbb{C}}_{1221}, \hat{\mathbb{C}}_{2121}$. The shear stress-strain relation can also be written in compliance form in terms of $\hat{C}_{33}, \hat{C}_{34}, \hat{C}_{44}$

$$\begin{Bmatrix} \hat{\Gamma}_{12} \\ \hat{\Gamma}_{21} \end{Bmatrix} = \begin{bmatrix} \frac{\hat{C}_{33}-2\hat{C}_{34}+\hat{C}_{44}}{4(\hat{C}_{33}\hat{C}_{44}-\hat{C}_{34}^2)} & -\frac{\hat{C}_{33}-\hat{C}_{44}}{4(\hat{C}_{33}\hat{C}_{44}-\hat{C}_{34}^2)} \\ -\frac{\hat{C}_{33}-\hat{C}_{44}}{4(\hat{C}_{33}\hat{C}_{44}-\hat{C}_{34}^2)} & \frac{\hat{C}_{33}+2\hat{C}_{34}+\hat{C}_{44}}{4(\hat{C}_{33}\hat{C}_{44}-\hat{C}_{34}^2)} \end{bmatrix} \begin{Bmatrix} \hat{\Sigma}_{12} \\ \hat{\Sigma}_{21} \end{Bmatrix} \tag{3.8}$$

To determine the 3 independent shear moduli, the response of the composite, under the application of simple shear stress (a) $\hat{\Sigma}_{12} = \Sigma$, $\hat{\Sigma}_{21} = 0$, (b) $\hat{\Sigma}_{12} = 0$, $\hat{\Sigma}_{21} = \Sigma$, and a pure shear stress (c) $\hat{\Sigma}_{12} = \hat{\Sigma}_{21} = \Sigma$ is analyzed. Due to the presence of the fibers and the direction at which they are aligned, the response of the composite under the these loading cases will result in different shear responses. Numerical tests are proposed to determine these shear moduli. Because a closed form expression

for $\hat{C}_{33} = \hat{G}_{12}$ is given by the CCM from applying a pure shear stress, only the numerical tests (a) and (b) will be shown to determine the shear moduli $\hat{C}_{34}$ and $\hat{C}_{44}$. These correspond to applying shear stress perpendicular and parallel to the fibers, respectively. As shown in Fig. 3.2, under the application of identical shear stress Σ for both cases, the angle of rotation (or shear strain) of the volume element will not be the same. For these boundary value problems, on each surface ($S_1 \bigcup S_2 \bigcup S_3 \bigcup S_4 = S$) of the volume element, either the displacement $\hat{u}_i^S$ or the force traction $\hat{f}_i^S = \hat{\Sigma}_{ji}\hat{n}_j^S$ is specified, where $\hat{n}_j^S$ is the surface normal.

These tests are conducted numerically using a finite element approach. The fibers are assumed to be arranged in a hexagonal pattern in 3D-space. Under this assumption, an equivalent 2D layered representation is considered for simplicity. The representation of a 3D fiber reinforced composite as an equivalent 2D layered structure is discussed in [23], [59]. In Fig. 3.2a, the boundary conditions are: (1) on surface S_1, the displacement along $\hat{x}_1$ direction is constrained, or $\hat{u}_1^S = 0$, and the traction $\hat{f}_2^S = \hat{\Sigma}_{12} = \Sigma$ is specified, (2) on surface S_3, $\hat{u}_1^S = 0$ and the traction $\hat{f}_2^S = -\hat{\Sigma}_{12} = -\Sigma$ is specified, and (3) surfaces S_2 and S_4 are traction free ($\hat{f}_i^S = 0$) so that $\hat{\Sigma}_{21} = 0$. Similarly, in Fig. 3.2b, (1) on surface S_4, the displacement along $\hat{x}_2$ direction is constrained, or $\hat{u}_2^S = 0$ and the traction $\hat{f}_1^S = \hat{\Sigma}_{21} = \Sigma$ is specified, (2) on surface S_2, $\hat{u}_2^S = 0$ and the traction $\hat{f}_1^S = -\hat{\Sigma}_{21} = -\Sigma$ is specified, and (3) surfaces S_1 and S_3 are traction free ($\hat{f}_i^S = 0$) so that $\hat{\Sigma}_{12} = 0$.

In Fig. 3.2a, the volume element is more resistant to shearing because the stiffer fibers carry the shear load, but in Fig. 3.2b the fibers are parallel to the loading directions, in which case the soft matrix layer predominantly carries the load. As a result, the rotation angle $\hat{\theta}_{21} > \hat{\theta}_{12}$. In these configurations, the rotation of the volume element is constrained ($\varphi_3 = 0$) and under small shear deformation, the asymmetric

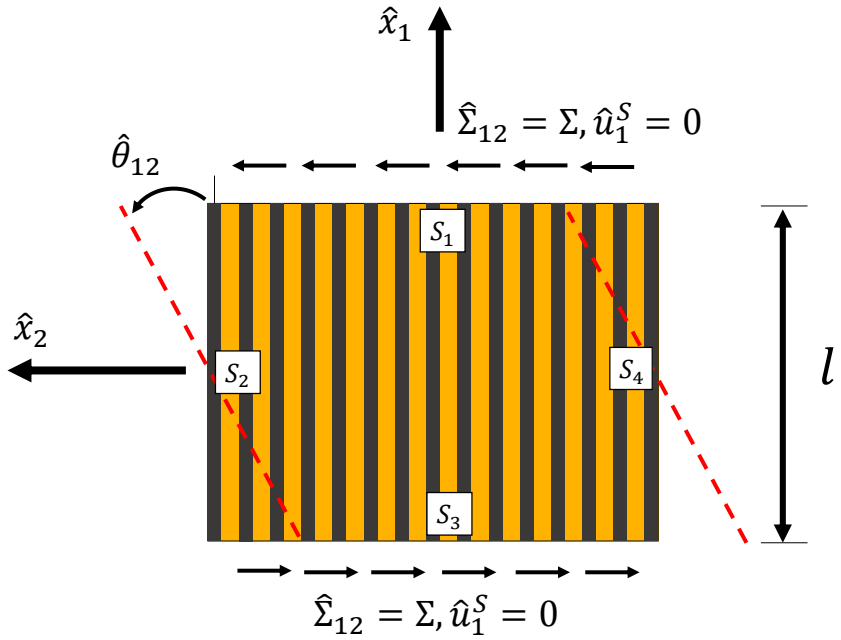

(a) Shear stress applied perpendicular to fibers

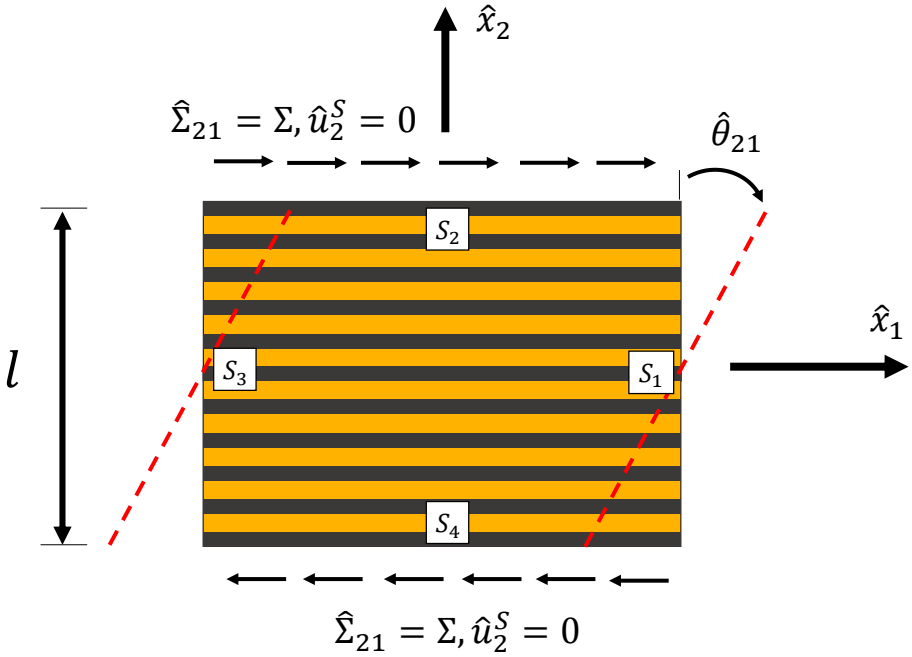

(b) Shear stress applied parallel to fibers

Figure 3.2: Schematic of an externally applied shear load on a fiber (black) and matrix (orange) layered composite.

shear strains defined in Eqn. 2.14 simplify in

$$\hat{\Gamma}_{12} = \hat{u}_{2,1} \approx \hat{\theta}_{12} \tag{3.9a}$$

$$\hat{\Gamma}_{21} = \hat{u}_{1,2} \approx \hat{\theta}_{21} \tag{3.9b}$$

where the shear rotation angles are defined $\hat{\theta}_{12} = 2\frac{\hat{u}_2(\hat{x}_1=l/2,\hat{x}_2=0)}{l}$ and $\hat{\theta}_{21} = 2\frac{\hat{u}_1(\hat{x}_1=0,\hat{x}_2=l/2)}{l}$. For the given applied loads in cases (a) and (b), these boundary value problems are solved numerically using a commercial finite element software, ABAQUS, where the corresponding angles of rotations are extracted. Using the constitutive relation in Eqn. 3.8, the relation between the external applied shear load and the shear deformation angle for case (a) is

$$\hat{\theta}_{12} = \left(\frac{\hat{C}_{33} - 2\hat{C}_{34} + \hat{C}_{44}}{4(\hat{C}_{33}\hat{C}_{44} - \hat{C}_{34}^2)} \right) \Sigma \tag{3.10}$$

Similarly, in case (b),

$$\hat{\theta}_{21} = \left(\frac{\hat{C}_{33} + 2\hat{C}_{34} + \hat{C}_{44}}{4(\hat{C}_{33}\hat{C}_{44} - \hat{C}_{34}^2)} \right) \Sigma \tag{3.11}$$

From these 2 algebraic equations, the 2 unknown properties, $\hat{C}_{34}, \hat{C}_{44}$ are evaluated. In the following analysis, the layered composite is assumed with a volume fraction of $V^f = 0.50$, fiber layer thickness of $2r_a = 6\mu m$ (r_a is fiber radius), and an external applied load $\Sigma = 0.1GPa$. Using this approach, 6 different volume element sizes are considered to minimize domain-size effects and to obtain the best approximation of the material properties. Square domains of length l are analyzed, with $6, 12, 18$, 24, 30, and 36 fibers. The deformation modes of cases (I)-(IV) obtained numerically is shown in Fig. 3.3. In Table 3.3, the micropolar shear properties are approximated $\hat{C}_{34} = 0.30GPa$ and $\hat{C}_{44} = 0.49GPa$.

(a) $\hat{\Sigma}_{12} = \Sigma$ applied on a 6 fiber volume element

(b) $\hat{\Sigma}_{21} = \Sigma$ applied on a 6 fiber volume element

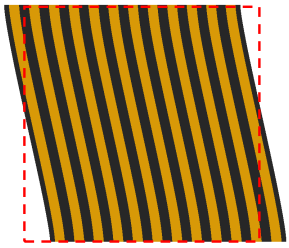

(c) $\hat{\Sigma}_{12} = \Sigma$ applied on a 12 fiber volume element

(d) $\hat{\Sigma}_{21} = \Sigma$ applied on a 12 fiber volume element

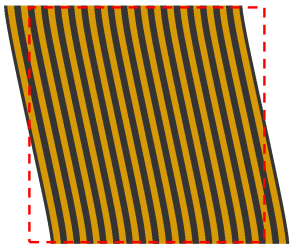

(e) $\hat{\Sigma}_{12} = \Sigma$ applied on a 18 fiber volume element

(f) $\hat{\Sigma}_{21} = \Sigma$ applied on a 18 fiber volume element

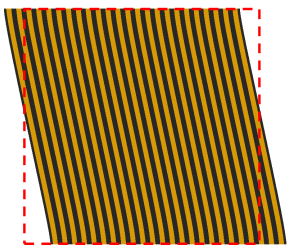

(g) $\hat{\Sigma}_{12} = \Sigma$ applied on a 24 fiber volume element

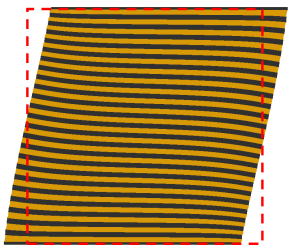

(h) $\hat{\Sigma}_{21} = \Sigma$ applied on a 24 fiber volume element

Figure 3.3: Numerical results of the deformation modes of the representative volume elements.

Table 3.3: Volume elements under external load $\Sigma = 0.1$GPa.

Case	Number of Fibers	$\hat{\theta}_{12}/\Sigma$ (1/GPa)	$\hat{\theta}_{21}/\Sigma$ (1/GPa)	$\hat{C}_{34}$ (GPa)	$\hat{C}_{44}$ (GPa)
(I)	6	0.41	0.78	0.48	0.62
(II)	12	0.48	0.79	0.36	0.53
(III)	18	0.51	0.79	0.32	0.50
(IV)	24	0.52	0.80	0.31	0.49
(V)	30	0.53	0.80	**0.30**	**0.49**
(VI)	36	0.53	0.80	**0.30**	**0.49**

3.2.3 Couple-stress and Curvature Relation

Next, the constants $\hat{C}_{55}$ and $\hat{C}_{66}$, relating the couple-stresses to curvatures, are analyzed. These material constants are assumed to correspond to the bending stiffness of the fibers. To evaluate them, we refer to the concentric cylinder model and treat it as a one-dimensional slender rod under an external bending moment $\hat{M}_3$ (Fig. 3.4).

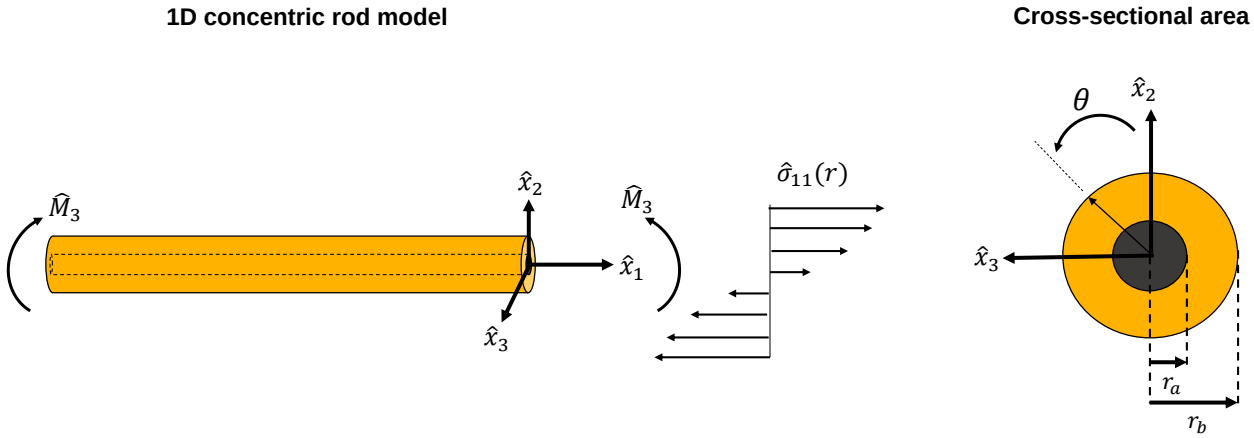

Figure 3.4: Concentric fiber-matrix cylinder under bending moment.

Under the assumptions of Timoshenko beam theory, the kinematic relation for the rod structure, under a bending moment $\hat{M}_3$ is

$$\hat{u}_1(\hat{x}_1, \hat{x}_2, \hat{x}_3) = -\hat{x}_2 \varphi_3(\hat{x}_1) \tag{3.12a}$$

$$\hat{u}_2(\hat{x}_1, \hat{x}_2, \hat{x}_3) = \hat{u}_2(\hat{x}_1) \tag{3.12b}$$

φ_3 is the independent rotational degree of freedom of the rod, which corresponds to the local rotation field in the micropolar continuum. The relevant normal strain $\hat{\varepsilon}_{11}$ for the structure is

$$\hat{\varepsilon}_{11} = \frac{\partial \hat{u}_1}{\partial \hat{x}_1} = -\hat{x}_2 \frac{d\varphi_3}{d\hat{x}_1} \tag{3.13}$$

From the definition of bending moment,

$$\hat{M}_3 = \int_A -\hat{x}_2 \hat{\sigma}_{11} dA \tag{3.14}$$

where $\hat{\sigma}_{11}$ is the nonuniform distribution of axial stress, on the cross-sectional area of the cylinder. Because the properties of the fiber and the matrix cylinders are dissimilar, the integration of Eqn. 3.14 can be expressed as

$$\hat{M}_3 = \int_{A^f} -\hat{x}_2 \hat{\sigma}^f_{11} dA^f + \int_{A^m} -\hat{x}_2 \hat{\sigma}^m_{11} dA^m \tag{3.15}$$

where $\hat{\sigma}^f_{11}$ and $\hat{\sigma}^m_{11}$ are the stresses in the fiber and the matrix layers of the rod, respectively, integrated over the cross sectional area of the fiber (A^f) and the matrix (A^m) layers. These stresses can be expressed in terms of strain,

$$\hat{\sigma}^f_{11} = \hat{E}^f_{11} \hat{\varepsilon}_{11} \tag{3.16a}$$

$$\hat{\sigma}^m_{11} = E^m \hat{\varepsilon}_{11} \tag{3.16b}$$

By substituting the constitutive relation above into Eqn. 3.15 and integrating, it results in

$$\begin{aligned} \hat{M}_3(\hat{x}_1) &= -\int_{r=0}^{r=r_a} \int_{\theta=0}^{\theta=2\pi} \left(r^2 \cos(\theta) \hat{E}^f_{11} \hat{\varepsilon}_{11} \right) d\theta dr - \int_{r=r_a}^{r=r_b} \int_{\theta=0}^{\theta=2\pi} \left(r^2 \cos(\theta) E^m \hat{\varepsilon}_{11} \right) d\theta dr \\ &= \pi \frac{r_a^4}{4} \left(\hat{E}^f_{11} - E^m \left(1 - (V^f)^{-2} \right) \right) \frac{d\varphi_3(\hat{x}_1)}{d\hat{x}_1} \end{aligned} \tag{3.17}$$

Normalizing this by the cross-sectional area $A = \pi r_b^2$, we arrive at the couple-stress and curvature relation

$$\hat{M}_{13} = \frac{\hat{M}_3}{A} = \frac{1}{4}\left(\hat{E}_{11}^f V^f - E^m(V^f - (V^f)^{-1})\right) r_a^2 \frac{d\varphi_3}{d\hat{x}_1} \tag{3.18}$$

From this, the material constant $\hat{C}_{55}$ is

$$\hat{C}_{55} = \frac{1}{4}\left(\hat{E}_{11}^f V^f - E^m(V^f - (V^f)^{-1})\right) r_a^2 \tag{3.19}$$

In the above expression, the fiber radius r_a should be emphasized. This is the so-called "length scale" introduced in the constitutive relation by considering micropolar theory.

Similarly, in a general 3D deformation state, the concentric rod model can be extended to obtain the relation of bending moment and rod twisting, along the $\hat{x}_2$ and $\hat{x}_1$ directions, respectively, which will not be considered in the 2D planar assumption. In addition, since the fibers are aligned along the $\hat{x}_1$-direction, the couple-stress $\hat{M}_{23}$ is negligible. Thus, $\hat{C}_{55} >> \hat{C}_{66}$, or $\hat{C}_{66} = 0$.

3.3 Material Nonlinear Behavior: Micropolar Elasto-plasticity

The load bearing capacity of the composite under compression is recognized to be strongly influenced by the matrix nonlinearity. At the microscale, with an increase in external loading, the matrix stiffness degrades due to the onset of plasticity. This causes the matrix material surrounding the fibers to loose its shear resistance with continued macroscopic loading, until a critical point when the fibers start to rotate locally. This is the onset of fiber kinking, as lucidly illustrated in Davidson and

Waas [24]. Since material nonlinearity is crucial for modeling this phenomenon, the nonlinearity at the microscale will be treated as an effective material nonlinearity at the macroscale. This is modeled under the basis of a flow rule, generalized to a micropolar continuum. Under the assumption of small strain, the total strain rates are expressed in terms of their elastic and plastic components

$$\dot{\hat{\Gamma}}_{ij} = \dot{\hat{\Gamma}}^e_{ij} + \dot{\hat{\Gamma}}^p_{ij} \tag{3.20a}$$

$$\dot{\hat{K}}_{i3} = \dot{\hat{K}}^e_{i3} + \dot{\hat{K}}^p_{i3} \tag{3.20b}$$

where by assuming the associative flow rule, the plastic strain rates are

$$\dot{\hat{\Gamma}}^p_{ij} = \dot{\lambda}\frac{\partial f}{\partial \hat{\Sigma}_{ij}} \tag{3.21a}$$

$$\dot{\hat{K}}^p_{i3} = \dot{\lambda}\frac{\partial f}{\partial \hat{M}_{i3}} \tag{3.21b}$$

The scalar $\dot{\lambda} \geq 0$ is the non-negative plastic multiplier. In literature, the formulation of an isotropic micropolar yield surface, based on the generalization of the von Mises criterion, with the presence of couple-stresses has been discussed by various authors, such as by de Borst [41]. Similar to Hill's yield criterion, which generalizes the isotropic von Mises criterion to orthotropic materials in a Cauchy continuum, the following pressure-independent criterion for orthotropic micropolar medium is proposed for a plane strain condition, by generalizing the yield surface in [41]

$$\begin{aligned} f = \Bigg(& \overline{F}\left(\hat{S}_{22} - \hat{S}_{33}\right)^2 + \overline{G}\left(\hat{S}_{33} - \hat{S}_{11}\right)^2 + \overline{H}\left(\hat{S}_{11} - \hat{S}_{22}\right)^2 \\ & + 2\overline{N}\hat{S}^2_{12} + \overline{Y}\hat{M}^2_{13} + \overline{Z}\hat{M}^2_{23} \Bigg)^{1/2} - \sigma_e(\epsilon_p) \end{aligned} \tag{3.22}$$

The yield criterion in Eqn. 3.22 is simply reduced from Eqn. 2.32, by replacing the asymmetric stresses with its symmetric and skew-symmetric decomposed components.

The equivalent plastic strain ε_p and the equivalent stress σ_e are defined from the definition of plastic work increment. Their relationship is determined experimentally. The relative ease/difficulty of yielding, along the different loading directions is taken in account by the constants $\overline{F}, \overline{G}, \overline{H}, \overline{N}, \overline{Y}$, and $\overline{Z}$ appearing in the plastic potential Eqn. 3.22. For simplicity, yielding due to couple stresses will be neglected, i.e, $\overline{Y} = \overline{Z} = 0$. In our analysis, it was determined that their effects were negligible on the localization (kinking) boundary value problem, which has also been verified by [41]. As a result, Eqn. 3.22 reduces to Hill's criterion. In addition, because of symmetry of the unidirectional fiber-reinforced composite, $\overline{G} = \overline{H}$. The remaining coefficients are obtained by performing numerical tests on a fiber-matrix layered micromechanics model. To do this, the 36 fiber volume element is considered. The isotropic matrix nonlinear equivalent stress-strain relation is shown in Fig. 3.5. This is the in-situ

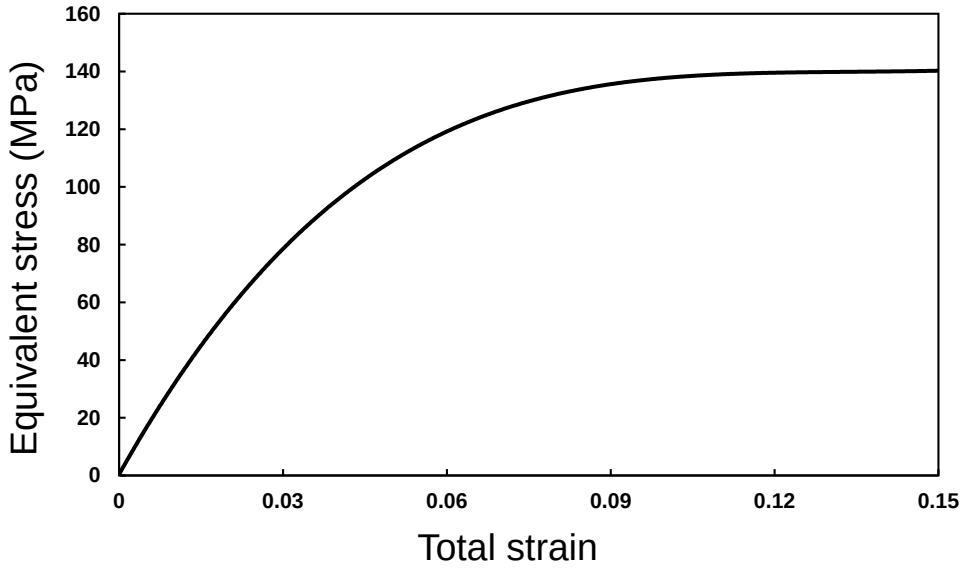

Figure 3.5: Isotropic matrix material nonlinearity [2].

matrix nonlinear response reported in [2]. It is implemented in the ABAQUS volume element model for the matrix layer. The transversely-isotropic fibers are assumed to be linear. The effective stress-strain response corresponding to the different loading directions are shown in Fig. 3.6. These results are also verified by [3], where the same

equivalent nonlinear responses are reported. By considering the relative yielding ratios

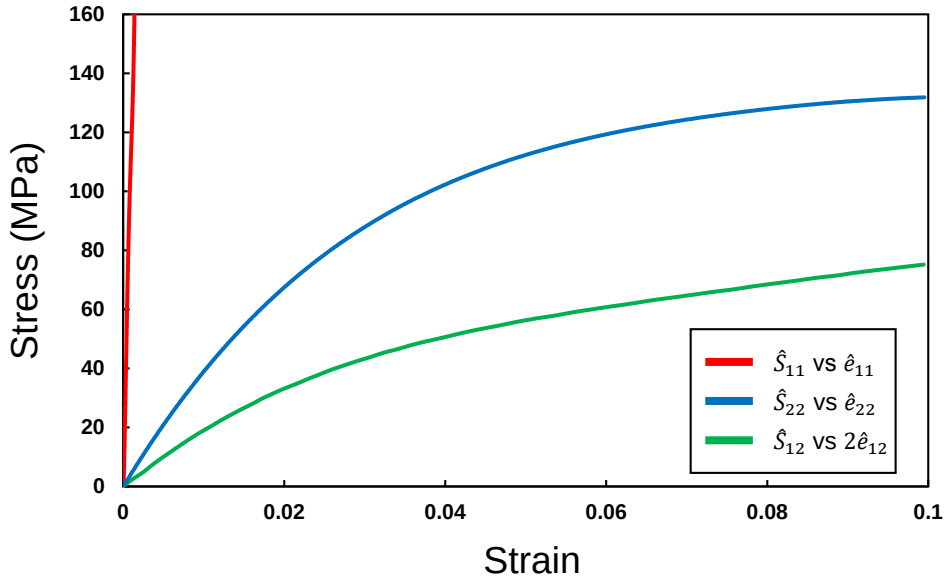

Figure 3.6: Equivalent nonlinear material nonlinearity under different symmetric loading conditions [3].

of each response, Hill's anisotropic constants are determined (Table 3.4). These values

Table 3.4: Hill's plasticity constants.

$\overline{F}$	$\overline{G}$	$\overline{H}$	$\overline{N}$	$\overline{Y}$	$\overline{Z}$
1.0	0.0	0.0	1.67	0.0	0.0

characterize the composite yielding under macroscopic shear and compression.

3.4 Fiber Kinking: Micromechanics and Micropolar Continuum

To verify the results of the homogenized micropolar continuum model, it will be compared with a layered micromechanics model, which considers the fiber and matrix layers, explicitly. In the micromechanics model, the transversely-isotropic fiber and isotropic matrix material properties presented earlier will be considered. The layered model has a volume fraction $V^f = 0.50$, with 75 fiber layers. The schematic (not

drawn to scale) of the boundary value problem is shown in Fig. 3.7. The horizontal

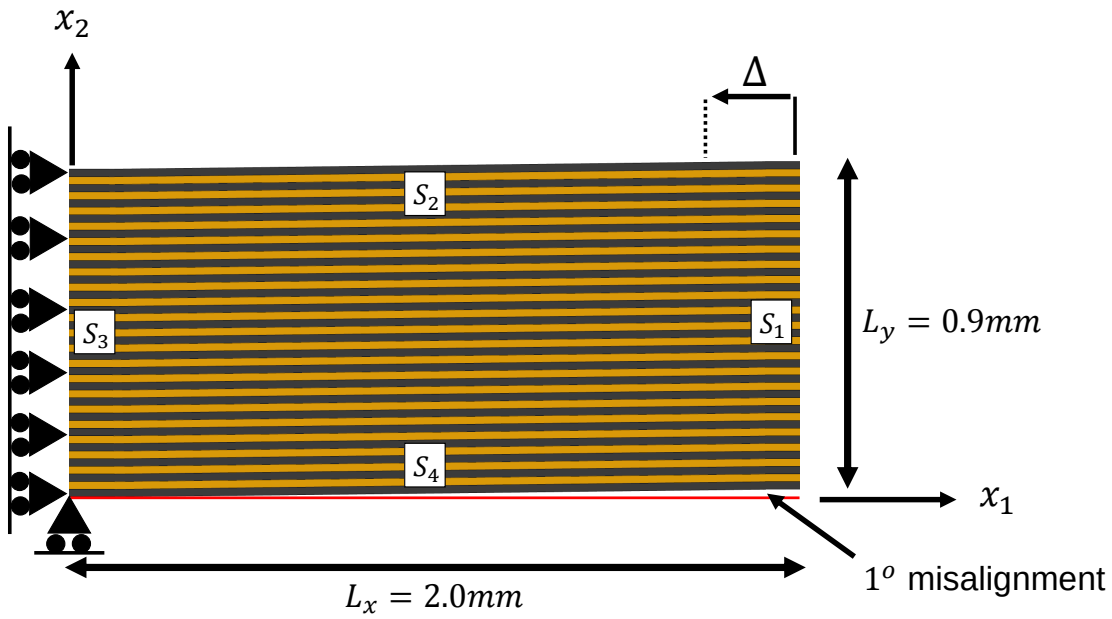

Figure 3.7: Schematic of the micromechanics boundary value problem.

and vertical dimensions of the domain are $L_x = 2.0mm$ and $L_y = 0.9mm$, respectively. In the micromechanics model, the displacement u_i^S or the force traction f_i^S is specified on each boundary ($S_1 \bigcup S_2 \bigcup S_3 \bigcup S_4 = S$). The boundary conditions are: (1) on S_1, the displacement $u_1^S = -\Delta$ (where $\Delta > 0$) is specified and $f_2^S = 0$, (2) on S_3, the displacement $u_1^S = 0$ is constrained and $f_2^S = 0$, (3) and surfaces S_2 and S_4 are traction free ($f_1^S = 0$ and $f_2^S = 0$). To prevent rigid body motion, (4) the node at the origin ($x_1 = 0$, $x_2 = 0$) is constrained $u_2 = 0$. For axial-shear coupling to be present, a geometric imperfection is introduced by misaligning the fibers by a 1-degree angle. Similarly, the equivalent micropolar continuum model is shown in Fig. 3.8. The geometric dimensions of the continuum domain are the same as the discrete model. In the micropolar continuum, the displacement u_i^S or the force traction f_i^S, and the rotation φ_3^S or the couple traction C_3^S are specified on each boundary ($S_1 \bigcup S_2 \bigcup S_3 \bigcup S_4 = S$). The boundary conditions are: (1) on S_1, the displacement $u_1^S = -\Delta$ (where $\Delta > 0$) is specified and $f_2^S = 0$, $C_3^S = 0$, (2) on S_3, the

displacement $u_1^S = 0$ is constrained and $f_2^S = 0$, $C_3^S = 0$, (3) and surfaces S_2 and S_4 are traction free ($f_1^S = 0$, $f_2^S = 0$, and $C_3^S = 0$). To prevent a rigid body translation, (4) the node at the origin ($x_1 = 0$, $x_2 = 0$) is constrained $u_2 = 0$. In addition, the same imperfection is also considered by perturbing the configuration by a 1-degree angle. The equivalent linear and nonlinear material properties determined earlier are used in the micropolar continuum model. The results of 3 meshes are presented,

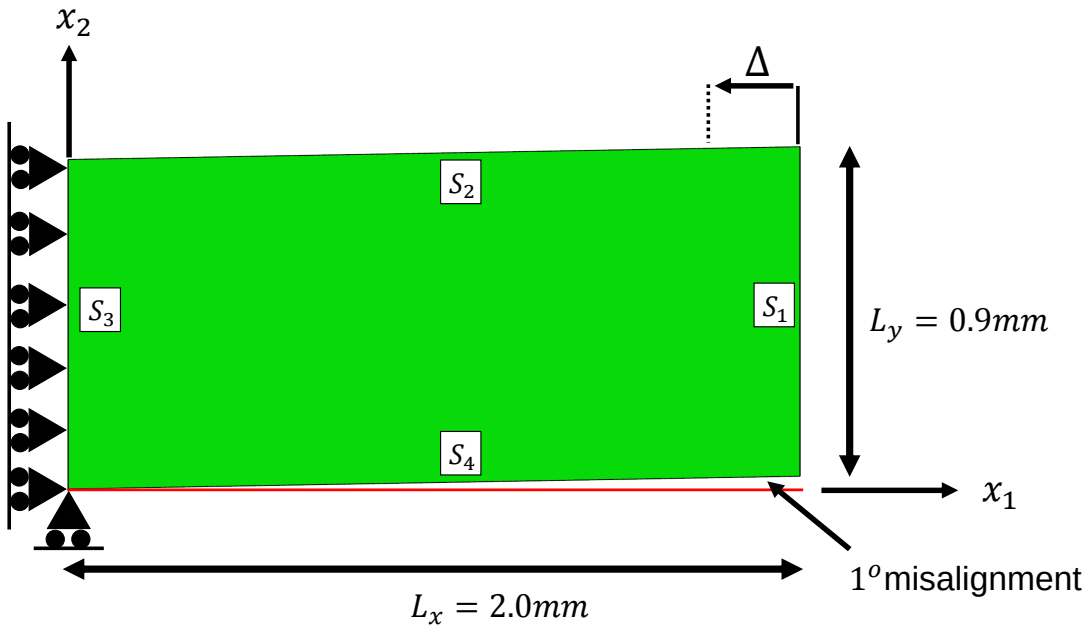

Figure 3.8: Schematic of the equivalent micropolar continuum boundary value problem.

a coarse mesh of 9×21 elements, an intermediate mesh of 14×31 elements, and a fine mesh of 18×41 elements. In obtaining the numerical solution for both the micromechanics and the equivalent micropolar models, an implicit arc-length solution scheme (Riks method) is used to capture the unstable equilibrium path of the snap-back response. This is shown in Fig. 3.9. The response of the problems is characterized by 4 regions, (a) a linear region, where the macroscopic stress-strain response of the structure is linear, (b) a limit-load, where the load bearing capability of the structure starts to drop, (c) the unstable unloading region, where localization develops, and

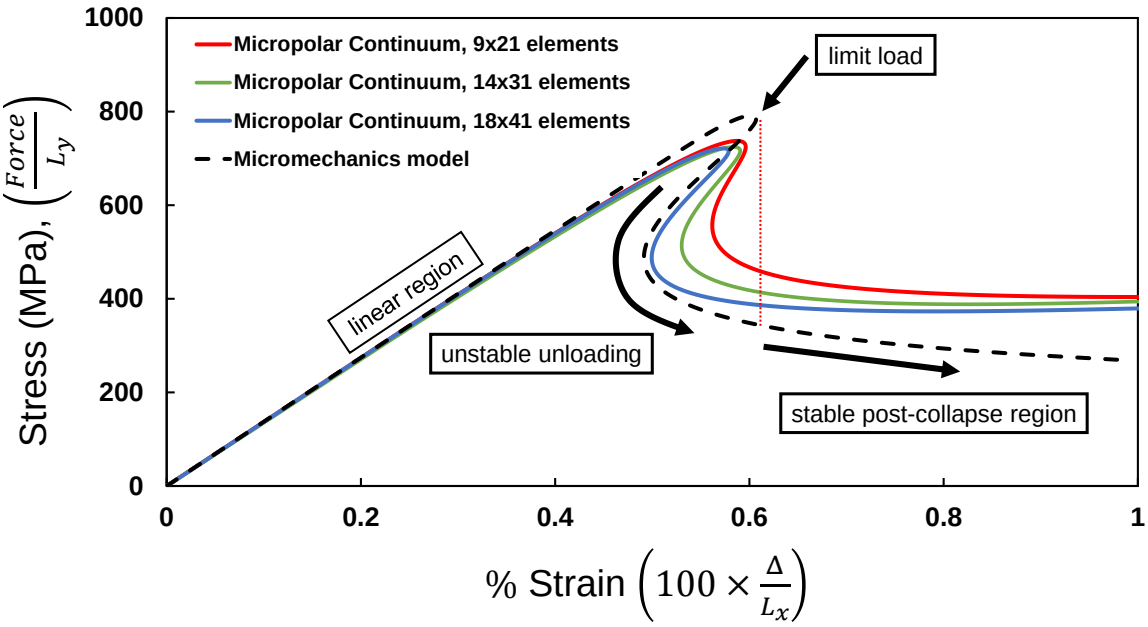

Figure 3.9: Stress response of the micromechanics and micropolar continuum models.

(d) continual stable loading of the structure. In this comparison, the micromechanics model is used to determine the validity of the micropolar continuum results. The response of the micromechanics and the continuum models are comparable up to the limit load. In the micromechanics model, the limit load is $\sigma_{cr} = 791MPa$. In the micropolar continuum, the limit load predictions are $\sigma_{cr} = 737MPa$, $\sigma_{cr} = 724MPa$, and $\sigma_{cr} = 721MPa$ for the 9×21, 14×31, and 18×41 element meshes, respectively. These predictions are within 9.7% error.

In the continuum model, as the mesh size is refined, the results tend to converge. In the coarse $9x21$ element mesh, due to the element size being larger than the localization width, there is a discrepancy with the $18x41$ element mesh in the unstable region (c), where localization starts to develop. However, in the stable region (d), the results of the responses of the 3 mesh sizes converge as the magnitude of the macroscopic load increases. At 1% strain, the difference between the three meshes is within 6% error. The length of time of the computations were 23min, 48min, and

86min for the 9×21, 14×31, and 18×41 element meshes, respectively, as apposed to 205min for the micromechanics simulation. In the stable post-collapse region, the load increases with applied compression in the continuum models, as apposed to the micromechanics model. This is attributed to the smearing of the fiber-matrix layers, which cause the elements to stiffen as they rotate.

In addition, and more importantly, the width of the localized band is captured in the continuum model. The deformation history of the micromechanics model is shown in Fig. 3.10. The contours show the accumulation of an equivalent plastic strain in the localized region. Based on geometry, the width of the kink band in the micromechanics model is about $w = 31.7d_f$, where d_f is the fiber diameter. Similarly, the deformation history of the continuum simulations are shown in Fig. 3.11, Fig. 3.12, and Fig. 3.13 for the 9×21, 14×31, and 18×41 element meshes, respectively. In the 18×41 element model, where the mesh size is much smaller than the localization width of the micromechanics model, the width of the kink band is $w = 33.6d_f$, which is in a very good agreement with the micromechanics model. From literature, it is reported that the width of the kink-band in typical carbon fiber composites is on the order of about $w = 10d_f$ to $30d_f$ [25], which is comparable to the continuum results.

The micropolar model also gives the ability to analyze the details of the microstructure of the composite from a continuum view. For example, Fig. 3.14a, b shows the micropolar couple-stress and curvature strain contours, respectively. These are representative of the local fiber bending and curvature at the microscale. As seen, the magnitudes of couple stress $\hat{M}_{13}$ and the curvature strain $\hat{K}_{13}$ are maximum at the horizontal edges of the boundaries of the localized region. From experimental observation, due to the presence of large fiber bending and curvature, at the onset of localization, the brittle fibers are observed to break at these locations, which correspond to the failure of the composite material. The details of fiber breakage due to localization and the empirical observation of it is discussed by Schultheisz and Waas

[25].

In Fig. 3.15a the contour plots of the micropolar rotation degrees of freedom is displayed. This corresponds to the local rotations of the fibers at the microscale. In a finite element analysis, the rotation φ_3 is a nodal degrees of freedom, which is a maximum at the center of the localized region. This characterizes the localization angle, which is 20.1-degree. As stated earlier, this is an independent kinematic degrees of freedom, which is in contrast to the classical definition of rotation in a Cauchy continuum, where it is dependent on the displacement field. For 2D finite deformation, this is defined

$$\psi_3 = \int \dot{\psi}_3 dt, \qquad \dot{\psi}_3 = \frac{1}{2}\left(\frac{\partial \dot{\hat{u}}_2}{\partial \hat{x}_1} - \frac{\partial \dot{\hat{u}}_1}{\partial \hat{x}_2}\right) \tag{3.23}$$

which is approximated using time integration. As shown in Fig. 3.15b, this corresponds to 18.3-degree.

3.5 Conclusion

In this chapter, the nonlinear micropolar model for fiber reinforced composites was used to compare the predictions of fiber kinking with an exact micromechanics model.

For these composites, physical meaning was first assigned to the anisotropic micropolar shear moduli, and virtual micromechanics tests were proposed to calibrate them. In addition, a closed form solution was determined for the couple stress-curvature relation. The linear and material nonlinear properties were used in the updated Lagrangian nonlinear micropolar finite element model to compute the compressive strength and kink band width of a fiber reinforced composite. In order to verify the continuum results, a discrete micromechanics model was also studied. The continuum model was seen to be within 9.7% agreement for the peak load, while predicting the details of kink band formation and the width of the localized band. The differences between the continuum model and the discrete model are also hinged

on the choice of the yield function adopted. In addition, information regarding the microstructure of the material, such as local fiber bending, curvature, and rotation, are a natural outcome of the theory.

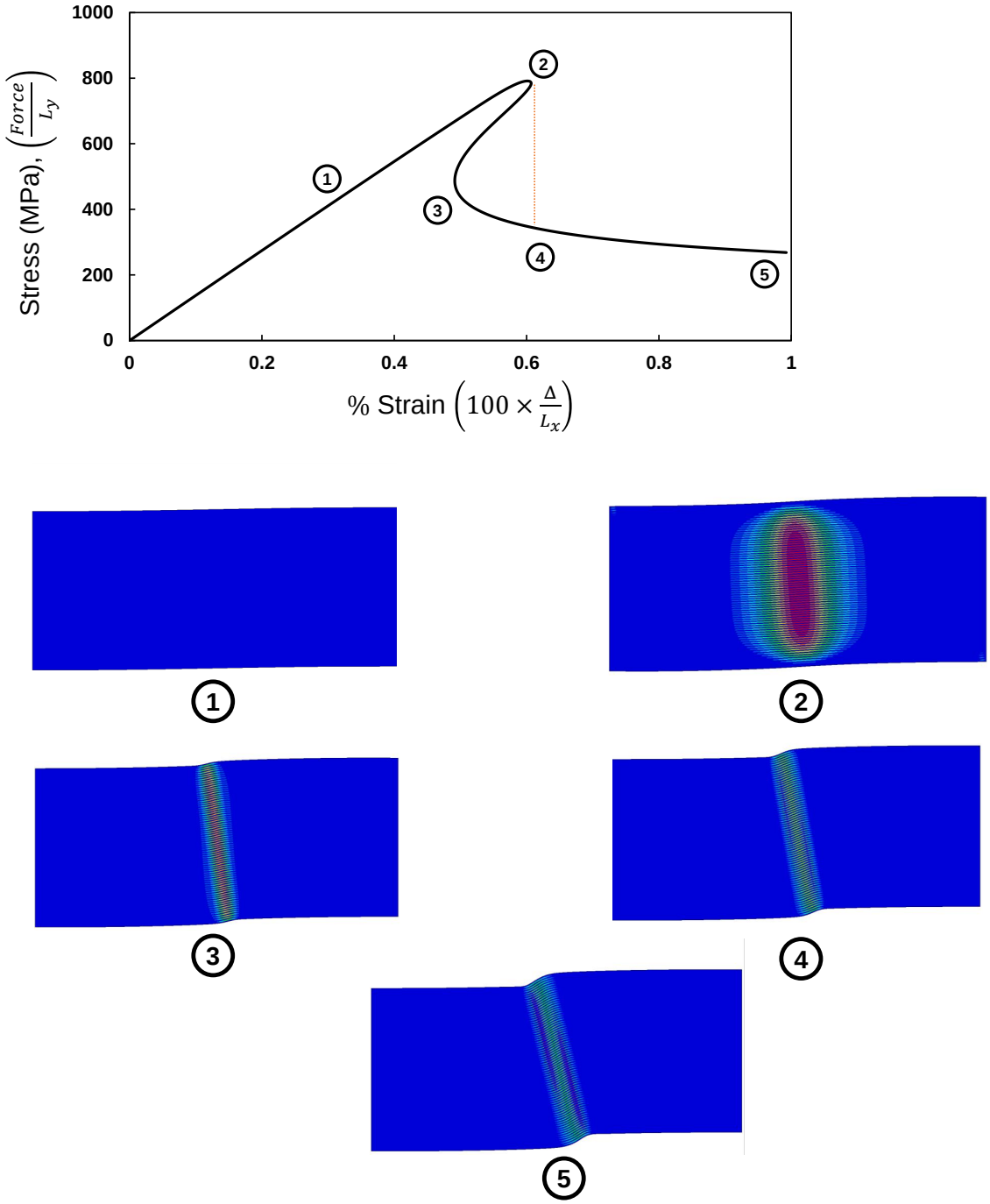

Figure 3.10: Deformation history of the micromechanics model.

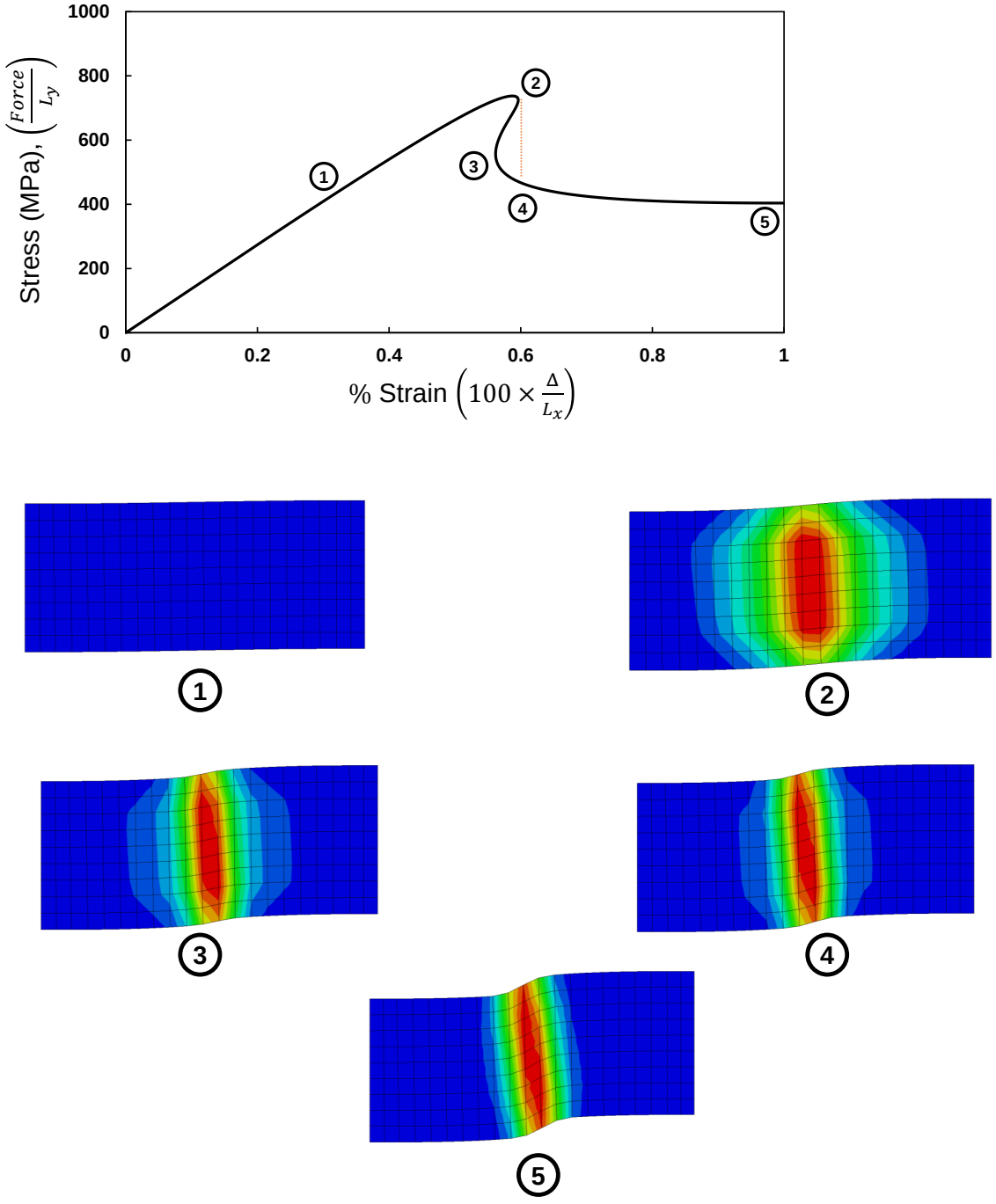

Figure 3.11: Deformation history of the 9×21 element mesh of the continuum model.

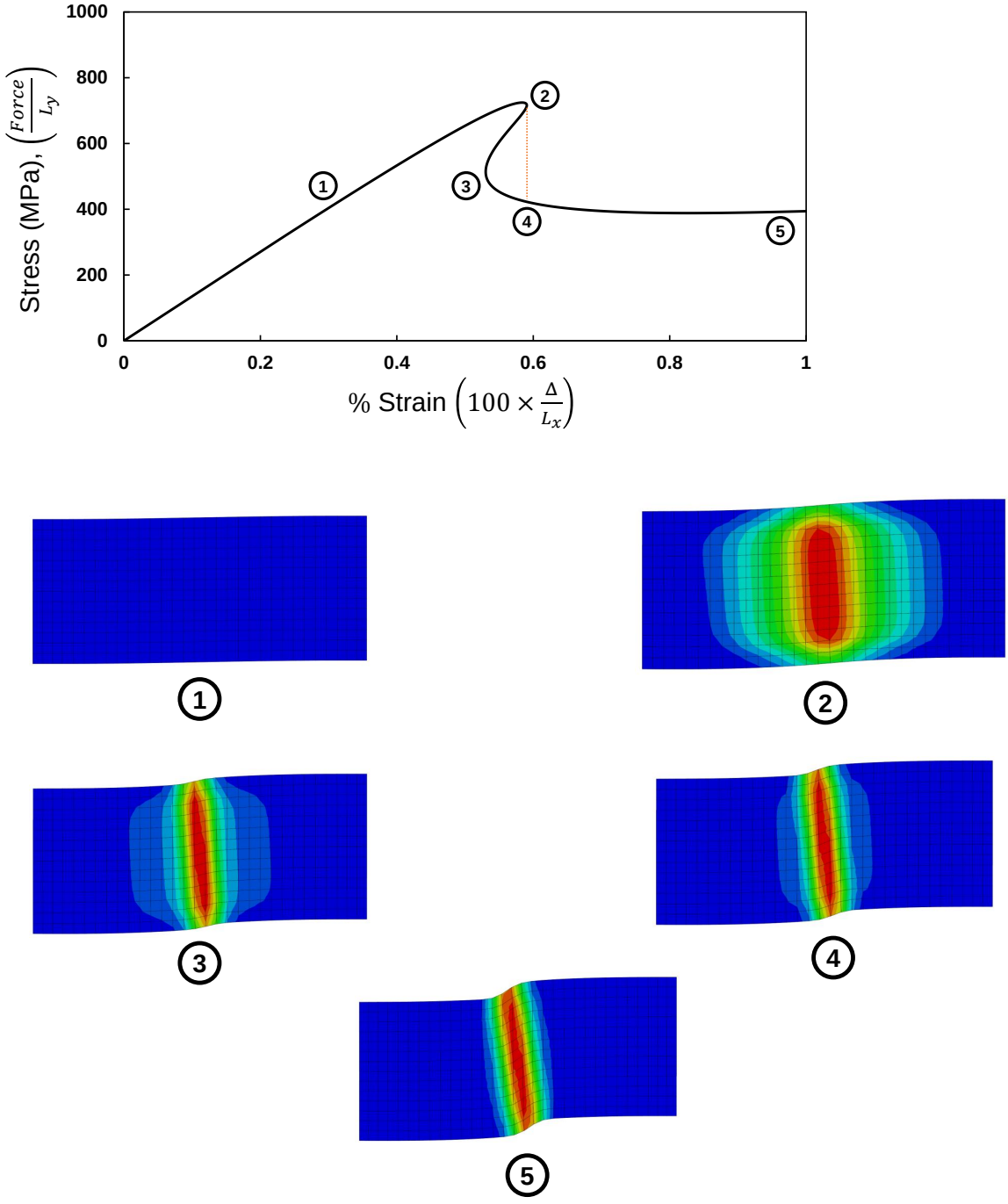

Figure 3.12: Deformation history of the 14×31 element mesh of the continuum model.

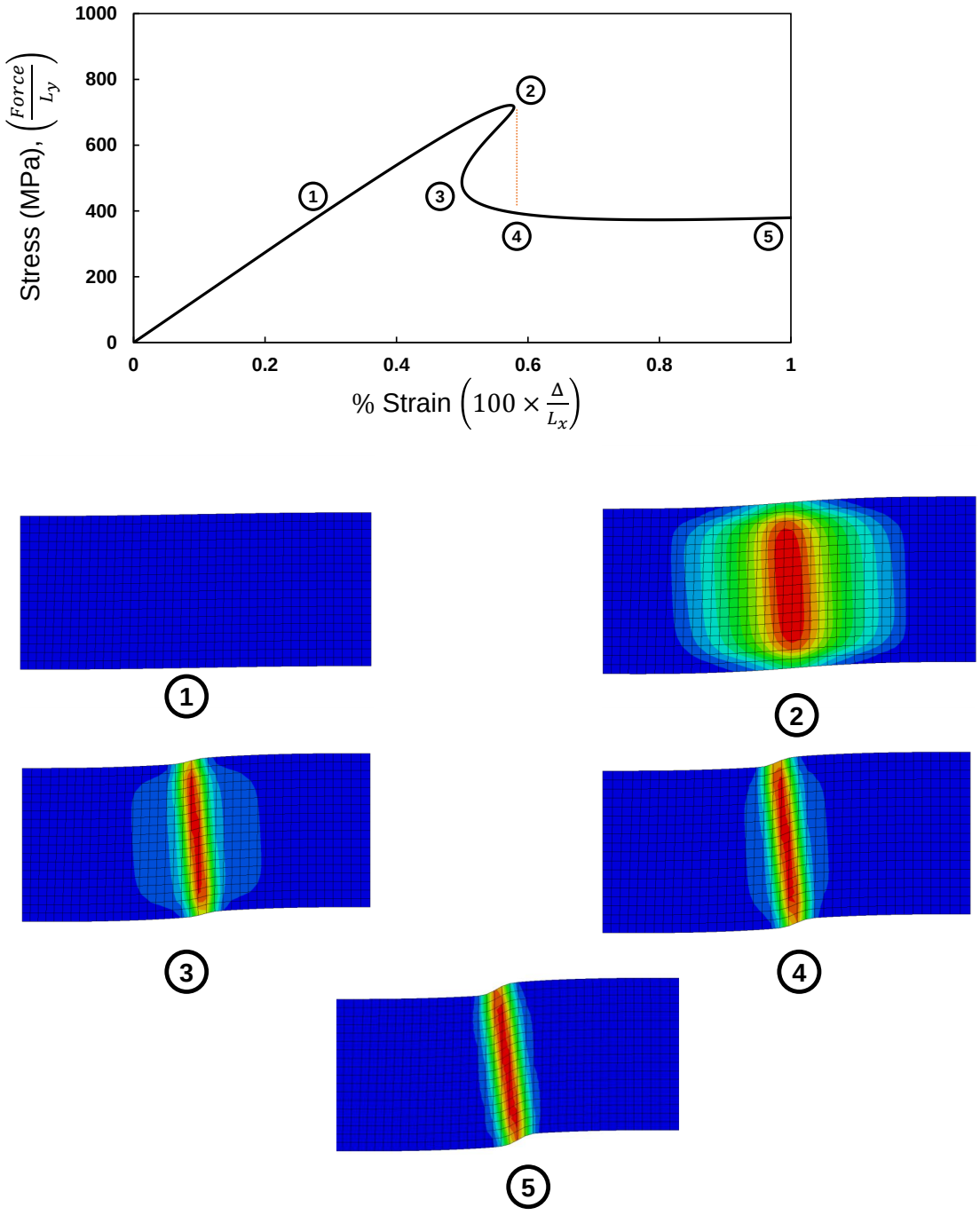

Figure 3.13: Deformation history of the 18×41 element mesh of the continuum model.

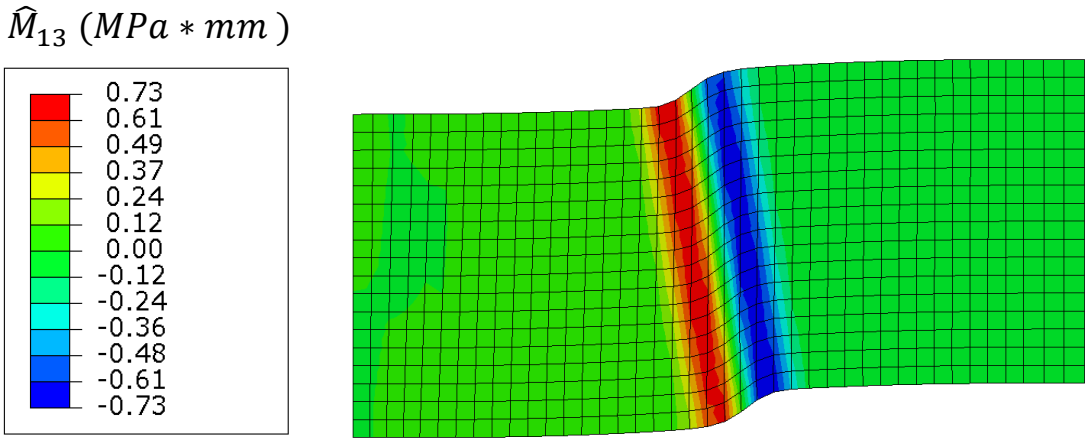

(a) Couple stress $\hat{M}_{13}$.

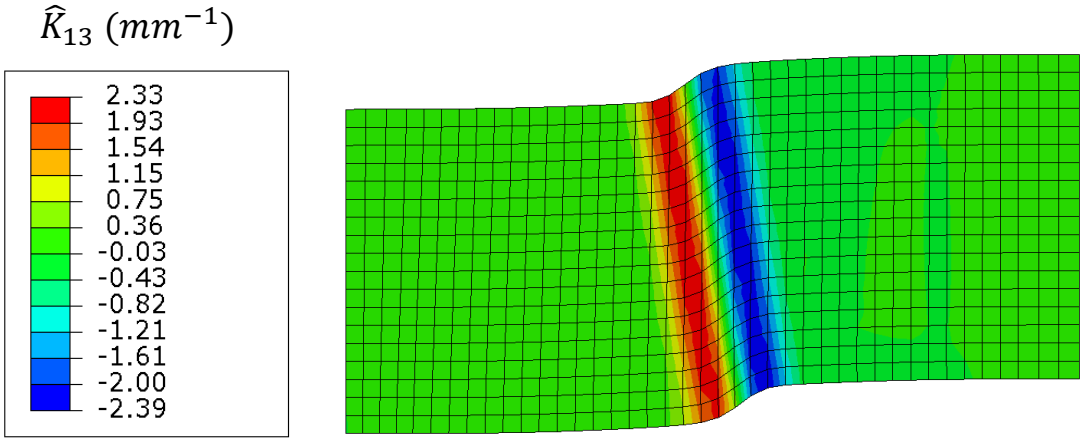

(b) Curvature strain $\hat{K}_{13}$.

Figure 3.14: Contour plots of (a) the micropolar couple-stress and (b) curvature strain at 1% strain (frame 5), for 18×41 element mesh.

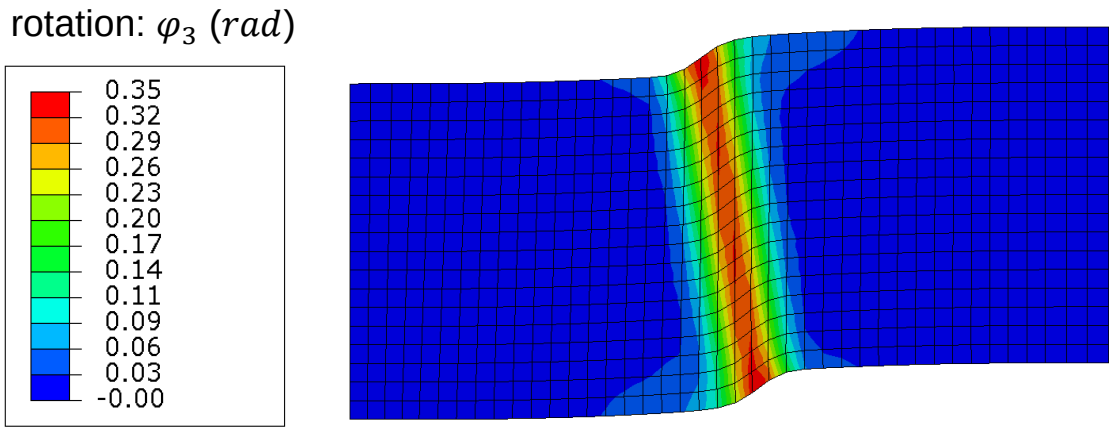

(a) Micropolar rotation φ_3.

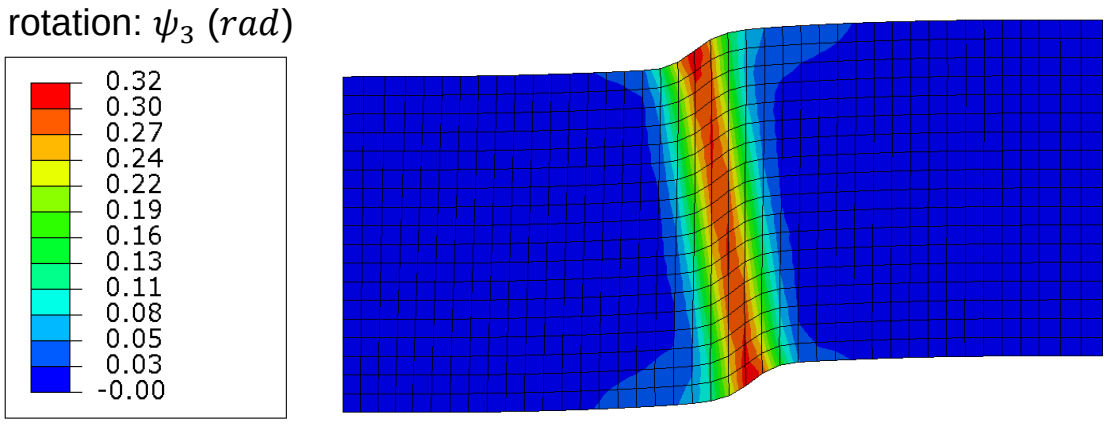

(b) Curvature strain ψ_3.

Figure 3.15: Contour plots of (a) micropolar rotation and (b) classical rotation in a Cauchy continuum, at 1% strain (frame 5), for 18×41 element mesh.

CHAPTER 4

Micropolar Constitutive Relations of Cellular Solids

4.1 Introduction

In the design of lightweight materials, a variety of cellular microstructures have emerged as a cost effective means of replacing traditional bulk solids. Among many examples, these cellular solids are used as the core of sandwich structures, energy absorbing devices, and acoustic barriers. Regular hexagonal cell honeycomb structures have been the most popular choice for sandwich structure applications, mainly because of the relative ease of production and simplicity in analyzing and determining their properties. With the advent of 3D printing, the field is wide open to optimize the design of cellular solids for specific applications. Early research on the mechanical response of cellular solids can be found in [27], where a strength of materials approach was used to determine the constitutive relation of a homogenized solid. However, past research studies have shown the possibility of enhancing the material properties of a regular hexagonal honeycomb by re-configuring its topology. For example, the stiffness, the brittle crushing strength, and the plastic yielding strength of circular cell honeycombs are higher than those of the same relative-density, regular hexagonal cell honeycombs [60]. Because of this, various experimental investigations have been done in [61], [62], and [63] to better understand these materials for application purposes.

In order to model this structure analytically, a strength of materials approach has been applied, similar to [27], for a regular hexagonal cell honeycomb to determine the constitutive relationship. This attempt was first initiated by [63], which used the modeling done in [64] on circular pipe bundles, to estimate the elastic moduli of a hexagonally packed circular honeycomb, and later [65] extended this approach to obtain the full constitutive relationship for this material in addition to the pre-stressed (elliptical honeycomb) properties. In literature, this method has been further extended to approximate the material properties based on the inclusion of axial and transverse shear deformation for circular [60] and elliptical cell honeycombs [66].

Despite the effort to determine the classical properties of these cellular solids, the analytical modeling of the deformation of these materials is not complete without the consideration of higher order effects. These include the higher order bending and rotation of the beam-like microstructure, which is crucial for modeling localization. In the following chapter, the determination of the additional micropolar material constants of these structures will be discussed.

One of the present challenges of micropolar theory has been the determination of the additional material constants in the constitutive relationship. This has been a subject of much research since the 1950's, as shown by the analytical methods reported in [67] for grid structures, and later extensions, [68], [69] to other simple beam structures. These methods also present a paradox in the calculation of the material constants, where an application of a Taylor series to approximate discrete displacement and rotation fields as a continuum, leads to non-convergent values of the constitutive relationship when higher order terms are kept in the expansion. A simple analytical approach was developed in [70], which is based on applying traction on a volume element in order to estimate the compliance matrix. However, this approach has also been limited to simple structures, and its extension to circular celled honeycomb has been found to pose a challenge.

Numerical estimates of the micropolar material constants have also been reported. For circular cell honeycombs, early attempts were initiated by [71]. In this work, the micropolar constants were determined numerically based on the analytical solution of a micropolar solid with a rigid inclusion. Later, [72] attempted to obtain simple closed form expressions for these constants through nondimensional analysis after numerically analyzing the deformation modes of a repeat unit of the material's microstructure. This micromechanics approach, however, resulted in symmetric stress and strain tensors and the moment and curvature relation displayed an anisotropy, which for a hexagonally packed honeycomb cell, has been proven to be isotropic by [70]. These discrepancies resulted from incorrectly incorporating the micropolar modes of deformation. First, the application of the asymmetric strains were incorrect by ignoring the local rotation, which resulted in a pseudo-Cosserat assumption (local rotation is equal to the global rotation). Second, when subjecting the repeating microstructure (or the representative volume element (RVE)) to a pure bending condition to obtain the curvature-couple stress relationship, its deformation was restricted to a classical-beam bending (Euler-Bernoulli assumptions). This assumption produced an anisotropy in the constitutive relationship.

To resolve this, [55] has proposed the correct way to incorporate the micropolar modes of deformation on a volume element in order to approximate the micropolar constitutive relationship. This method uses the generalization of Hill-Mandel condition for a micropolar continuum in order to approximate the constitutive relationship as an average over the RVE. It has been applied by [73] and [58] to estimate the material constants for foams and masonry structures, respectively. [56] has also generalized this method to model a random two-phase micropolar composite, with a random distribution of inclusion on matrix. Further details of this homogenization method can also be found in [40]. However, the application of this method has not yet been applied to periodic cellular materials, which is the subject of the present

analysis.

In this chapter, we will first present the micromechanics homogenization method for micropolar medium, based on the Hill-Mandel condition. This will then be applied to evaluate the constitutive relationship of a hexagonally packed circular honeycomb and the closed form solution will be determined using nondimensional analysis. These closed form guessed expressions for the material constants will then be verified by comparing them to numerical predictions of the material constants, which will be used as a benchmark. In addition, this method will also be applied to a grid structure and a regular hexagon honeycomb with uniform as well as non-uniform thickness. Our evaluated material constants will them be compared with various reported values in literature.

4.2 Problem Formulation

Our main goal is to determine the micropolar constitutive relationship of a hexagonally packed circular celled honeycomb shown in Fig. 4.1a. This structure has 3 different length scales present, some global length L describing the size of the material, the radius R of each circular cell, and their thickness t. These will correspond to the macroscopic, mesoscopic (intermediate), and microscopic length scales, respectively, described by [40]. It is important to identify these length scales, since their relative magnitude shows the best approach to apply to model a material. For a sample with relatively small number of cells (L comparable to R), the deformation of the structure can be analyzed by modeling each cell discretely. However, this can be cumbersome for structures with large number of cells ($L >> R$). A common approach to overcome this is to approximate (homogenize) the structure as a continuum. In such a case, each material point on the continuum corresponds to a representative volume element (RVE), whose dimensions are in the same order as the mesoscale.

For the circular honeycomb, the RVE is shown in Fig. 4.1b.

When resorting to homogenization of the RVE as a classical continuum, it is assumed that the fluctuation of stresses and strains about their mean values across the RVE are small, and they are approximated to be uniform. This is indeed the case when the microscale of the structure is much smaller than the mesoscale ($L >> R >> t$). In most cases, this is not always true and these two length scales can be comparable ($L >> R > t$), such as in the cases where local deformations occur. In such situations, the non-uniformity of stresses and strains in the RVE are accounted for by modeling these materials using higher order theories. Micropolar theory is the most popular due to its relative simplicity [74]. In addition, in micropolar theory, the interaction between neighboring material points (RVE) are governed not only by a force vector from classical continuum theory, but also through a moment vector. Because many cellular materials, (Fig. 4.1a for example), are modeled as a connection of beams or arches, bending is often a prominent deformation mechanism, and at the microscale, both displacements and rotations need to be present [55].

4.3 Micropolar Constitutive Relationship

Because of the limitations of classical elasticity, micropolar theory is the ideal continuum theory to represent cellular materials. In this generalization, a material point is not only characterized by a displacement vector, but also through an independent microrotational vector φ_i, which is different from the global rotation, $\Omega_i = \frac{1}{2} e_{ikj} u_{j,k}$ ($i = 1, 2, 3$ and e_{ikj} is the permutation tensor). For a 2D micropolar solid, with the 3-direction corresponding to the out of plane direction, the constitutive relationship

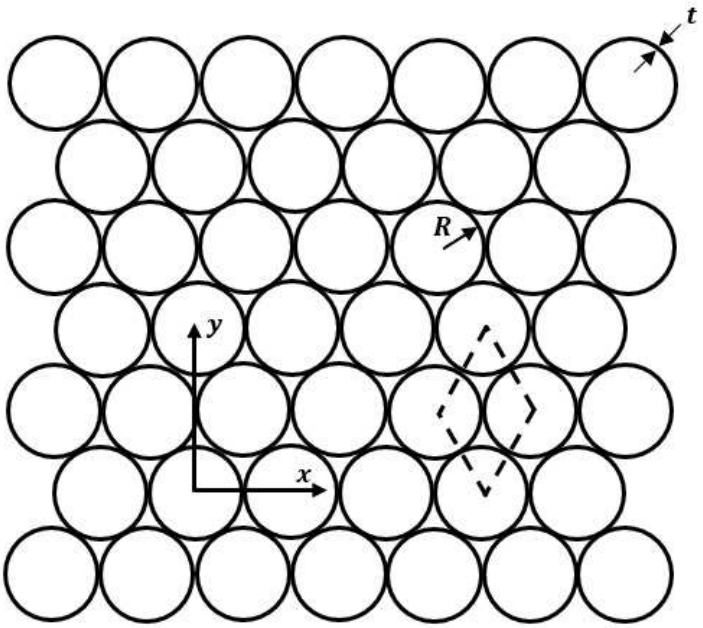

(a) In-plane view of a hexagonally packed circular cell honeycomb

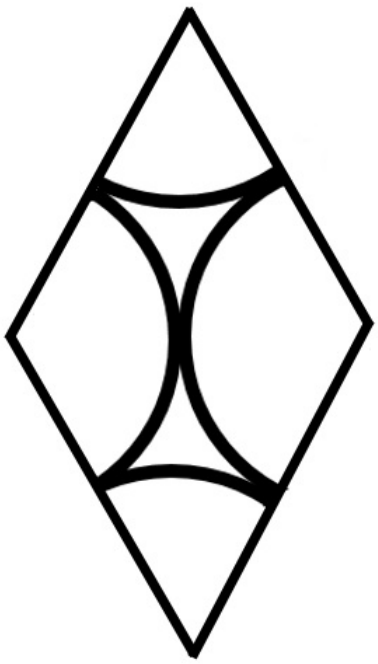

(b) Diamond shape RVE of the honeycomb

Figure 4.1: Configuration of a honeycomb at the global and local scales.

for a linear, isotropic solid is represented as

$$\begin{bmatrix} \Sigma_{11} \\ \Sigma_{22} \\ \Sigma_{12} \\ \Sigma_{21} \\ M_{13} \\ M_{23} \end{bmatrix} = \begin{bmatrix} 2\mu_E + \lambda_E + k_E & \lambda_E & 0 & 0 & 0 & 0 \\ \lambda_E & 2\mu_E + \lambda_E + k_E & 0 & 0 & 0 & 0 \\ 0 & 0 & \mu_E + k_E & \mu_E & 0 & 0 \\ 0 & 0 & \mu_E & \mu_E + k_E & 0 & 0 \\ 0 & 0 & 0 & 0 & \gamma_E & 0 \\ 0 & 0 & 0 & 0 & 0 & \gamma_E \end{bmatrix} \begin{bmatrix} \Gamma_{11} \\ \Gamma_{22} \\ \Gamma_{12} \\ \Gamma_{21} \\ K_{13} \\ K_{23} \end{bmatrix} \tag{4.1}$$

where μ_E, k_E, λ_E, and γ_E are the in plane micropolar material constants, expressed in Eringen's notation [74], Σ_{ji}, M_{j3} are the asymmetric stress and couple-stress, and Γ_{ji} K_{j3} are the asymmetric strain and curvature tensors $(i, j = 1, 2)$, which are related to the displacements and rotation by

$$\Gamma_{ji} = u_{i,j} - e_{ji3}\varphi_3 \tag{4.2a}$$

$$K_{j3} = \varphi_{3,j} \tag{4.2b}$$

For simplicity, it is often convenient to decompose the asymmetric stress and strain tensors in their symmetric and antisymmetric components

$$\Sigma_{ij} = S_{ij} + T_{ij} \tag{4.3a}$$

$$\Gamma_{ij} = E_{ij} + A_{ij} \tag{4.3b}$$

where

$$S_{ij} = \frac{1}{2}(\Sigma_{ij} + \Sigma_{ji}) = S_{ji} \tag{4.4a}$$

$$T_{ij} = \frac{1}{2}(\Sigma_{ij} - \Sigma_{ji}) = -T_{ji} \tag{4.4b}$$

$$E_{ij} = \frac{1}{2}(\Gamma_{ij} + \Gamma_{ji}) = \frac{1}{2}(u_{i,j} + u_{j,i}) = E_{ji} \tag{4.4c}$$

$$A_{ij} = \frac{1}{2}(\Gamma_{ij} - \Gamma_{ji}) = e_{ij3}(\Omega_3 - \varphi_3) = -A_{ji} \tag{4.4d}$$

Using these simplifications, Eqn. 4.1 reduces to

$$\begin{bmatrix} S_{11} \\ S_{22} \\ S_{12} \\ T_{12} \\ M_{13} \\ M_{23} \end{bmatrix} = \begin{bmatrix} 2\mu+\lambda & \lambda & 0 & 0 & 0 & 0 \\ \lambda & 2\mu+\lambda & 0 & 0 & 0 & 0 \\ 0 & 0 & 2\mu & 0 & 0 & 0 \\ 0 & 0 & 0 & 2\mu_c & 0 & 0 \\ 0 & 0 & 0 & 0 & \gamma_c & 0 \\ 0 & 0 & 0 & 0 & 0 & \gamma_c \end{bmatrix} \begin{bmatrix} E_{11} \\ E_{22} \\ E_{12} \\ A_{12} \\ K_{13} \\ K_{23} \end{bmatrix} \tag{4.5}$$

The relationship between the constants in Eqn. 4.1 and 4.5 are

$$\mu_E = \mu - \mu_c \tag{4.6a}$$

$$k_E = 2\mu_c \tag{4.6b}$$

$$\lambda_E = \lambda \tag{4.6c}$$

$$\gamma_E = \gamma_c \tag{4.6d}$$

This form of the constitutive relationship is desired, because S_{ij} and E_{ij} correspond to the symmetric stresses and strains in classical elasticity, with μ and λ being the Lamé constants. The remaining two material constants (μ_c, γ_c) are the additional micropolar constants.

4.4 Micropolar Homogenization Method

In order to determine the material constants for a circular honeycomb structure, the micromechanical method by [55] will be applied. This homogenization method considers the principal of virtual work in terms of the the stresses and strains defined

in Eqn. 4.5

$$\int_V (S_{ji}\delta E_{ji} + T_{ji}\delta A_{ji} + M_{j3}\delta K_{j3})dV = \int_S (T_i\delta u_i + Q_3\delta\varphi_3)dS \tag{4.7}$$

where $i, j = 1, 2$ in 2D, V is the volume, and S is the surface at which surface traction T_i and surface couple Q_3 are acted on. The goal of this approach is to approximate the constitutive relationship of a composite sample by expressing the principal of virtual work in Eqn. 4.7, averaged over the RVE. This is done by applying the Hill-Mandel condition for micropolar continuum [55]

$$\int_V (S_{ji}\delta E_{ji} + T_{ji}\delta A_{ji} + M_{j3}\delta K_{j3})dV = V(\overline{S}_{ji}\overline{\delta E}_{ji} + \overline{T}_{ji}\overline{\delta A}_{ji} + \overline{M}_{j3}\overline{\delta k}_{j3}) \tag{4.8}$$

The overbars on the right hand side of Eqn. 4.8 denote the averaged quantities over the RVE. In addition to the simplification done to the left hand side of Eqn. 4.7, a similar simplification can be applied on the right hand side

$$\int_S (T_i\delta u_i + Q_3\delta\varphi_3)dS = \sum_{k=1}^{n} (f_i^{(k)}\delta u_i^{(k)} + \mu_3^{(k)}\delta\varphi_3^{(k)}) \tag{4.9}$$

f_i^k and μ_3^k are the force and moment acting on the k^{th} cell wall on the surface of the RVE. By substituting the above averaged expressions into Eqn. 4.7, the principal of virtual work simplifies to

$$\overline{S}_{ji}\overline{\delta E}_{ji} + \overline{T}_{ji}\overline{\delta A}_{ji} + \overline{M}_{j3}\overline{\delta K}_{j3} = \frac{1}{V}\sum_{k=1}^{n} (f_i^{(k)}\delta u_i^{(k)} + \mu_3^{(k)}\delta\varphi_3^{(k)}) \tag{4.10}$$

It should also be noted that the Hill-Mandel condition in Eqn. 4.8 is valid if and only if the correct admissible RVE boundary conditions are applied. For the present

analysis, kinematic boundary conditions will be considered

$$u_i^{(k)} = \overline{E}_{ji} x_j^{(k)} + e_{ji3}\overline{\Omega}_3 x_j^{(k)} \tag{4.11a}$$

$$\varphi_3^{(k)} = \overline{\Omega}_3 + \frac{1}{2} e_{ij3}\overline{A}_{ji} + \overline{K}_{j3} x_j^{(k)} \tag{4.11b}$$

where $\overline{E}_{ji}, \overline{\Omega}_3, \overline{A}_{ji}, \overline{K}_{j3}$ are arbitrary constant numbers and $x_j^{(k)}$ are the coordinates of the cell walls on the surface of the RVE. For reference, the proof of Hill's lemma along with the Hill-Mandel condition for micropolar continuum is shown in [75].

By substituting the boundary conditions in Eqn. 4.11 into Eqn. 4.10 and collecting the coefficients of $\overline{\delta E}_{ji}, \overline{\delta\Omega}_3, \overline{\delta A}_{ji}$, and $\overline{\delta M}_{j3}$, the following is obtained

$$\begin{gathered}\left(\overline{S}_{ji} - \frac{1}{V}\sum_{k=1}^{n}(f_i^{(k)} x_j^{(k)})\right)\delta\overline{E}_{ji} + \left(\overline{T}_{ji} - \frac{1}{2V}\sum_{k=1}^{n}(e_{ij3}\mu_3^{(k)})\right)\delta\overline{A}_{ji} + \\ \left(\overline{M}_{j3} - \frac{1}{V}\sum_{k=1}^{n}(x_j^{(k)}\mu_3^{(k)})\right)\delta\overline{K}_{j3} - \frac{1}{V}\sum_{k=1}^{n}(e_{ji3} f_i^{(k)} x_j^{(k)} + \mu_3^{(k)})\delta\overline{\Omega}_3 = 0\end{gathered} \tag{4.12}$$

In the above expression, the $\delta()$ and $\overline{()}$ are interchangeable since they are linear operators. For different displacement and rotation fields applied on the surface of the RVE, the constants $\overline{E}_{ji}, \overline{\Omega}_3, \overline{A}_{ji}, \overline{K}_{j3}$ need to be specified in such a way that Eqn. 4.12 is satisfied exactly. As a result, for each term

$$\overline{S}_{ji} = \frac{1}{2V}\sum_{k=1}^{n}(f_j^{(k)} x_i^{(k)} + f_i^{(k)} x_j^{(k)}) \text{ OR } \delta\overline{E}_{ji} = 0 \tag{4.13a}$$

$$\overline{T}_{ji} = \frac{1}{2V}\sum_{k=1}^{n}(e_{ij3}\mu_3^{(k)}) \text{ OR } \delta\overline{A}_{ji} = 0 \tag{4.13b}$$

$$\overline{M}_{j3} = \frac{1}{V}\sum_{k=1}^{n}(\mu_3^{(k)} x_j^{(k)}) \text{ OR } \delta\overline{K}_{j3} = 0 \tag{4.13c}$$

$$\sum_{k=1}^{n}(e_{ji3} f_i^{(j)} x_j^{(k)} + \mu_3^{(k)}) = 0 \text{ OR } \delta\overline{\Omega}_3 = 0 \tag{4.13d}$$

In Eqn 4.12, it should be highlighted that the variation of the strains or the global

rotation are zero only when these terms are specified on the boundary. They are non-zero if and only if they are not specified, in which case, their coefficients must be equal to zero. It should also be noted that the coefficient of $\delta\overline{\Omega}_3$ is the balance of angular momentum of the RVE. If this equilibrium condition is not satisfied, the RVE will not achieve equilibrium. If this is the case, $\delta\overline{\Omega}_3$ must be set to zero by specifying $\overline{\Omega}_3$ at the boundary.

4.5 Deformation Modes of RVE

The idea of the current homogenization method is to determine the average constitutive relationship of a structure by applying the boundary conditions specified in Eqn. 4.11 and calculating the average stresses and couple stresses defined by Eqn. 4.13, while the condition in Eqn. 4.12 is always satisfied. In doing this, the constitutive relationship is determined in an averaged sense. For a 2D, isotropic solid, this will be in form

$$\begin{bmatrix} \overline{S}_{11} \\ \overline{S}_{22} \\ \overline{S}_{12} \\ \overline{T}_{12} \\ \overline{M}_{13} \\ \overline{M}_{23} \end{bmatrix} = \begin{bmatrix} \overline{C}_{11} & \overline{C}_{12} & 0 & 0 & 0 & 0 \\ \overline{C}_{21} & \overline{C}_{22} & 0 & 0 & 0 & 0 \\ 0 & 0 & \overline{C}_{33} & 0 & 0 & 0 \\ 0 & 0 & 0 & \overline{C}_{44} & 0 & 0 \\ 0 & 0 & 0 & 0 & \overline{C}_{55} & 0 \\ 0 & 0 & 0 & 0 & 0 & \overline{C}_{66} \end{bmatrix} \begin{bmatrix} \overline{E}_{11} \\ \overline{E}_{22} \\ \overline{E}_{12} \\ \overline{A}_{12} \\ \overline{K}_{13} \\ \overline{K}_{23} \end{bmatrix} \tag{4.14}$$

where $\overline{C}_{12} = \overline{C}_{21}$, $\overline{C}_{11} = \overline{C}_{22}$, $\overline{C}_{33} = \overline{C}_{11} - \overline{C}_{12}$ and $\overline{C}_{55} = \overline{C}_{66}$. To determine the stiffness matrix $\overline{C}_{ij}$, the strains $\overline{E}_{ij}, \overline{A}_{ij}$, and $\overline{K}_{i3}$ will be considered one at a time on the RVE, and their responses $\overline{S}_{ij}, \overline{T}_{ij}$, and $\overline{M}_{i3}$ will be calculated to determine the stiffness matrix $\overline{C}_{ij}$. In 2D, the boundary conditions (Eqn. 4.14) being applied on the

surface of the RVE will be of the form

$$u_1^{(k)} = \overline{E}_{11}x_1^{(k)} + \overline{E}_{21}x_2^{(k)} - \overline{\Omega}_3 x_2^{(k)} \tag{4.15a}$$

$$u_2^{(k)} = \overline{E}_{12}x_1^{(k)} + \overline{E}_{22}x_2^{(k)} + \overline{\Omega}_3 x_1^{(k)} \tag{4.15b}$$

$$\varphi_3^{(k)} = \overline{\Omega}_3 - \overline{A}_{12} + \overline{K}_{13}x_1^{(k)} + \overline{K}_{23}x_2^{(k)} \tag{4.15c}$$

In Eqn. 4.14, it should be noted that the symmetric stresses are decoupled from the asymmetric strain ($\overline{A}_{12}$) and the curvatures ($\overline{K}_{13}$, $\overline{K}_{23}$) due to the centrosymmetry (non-chiral) of a material. Because of this, we can consider the classical and micropolar modes of deformation separately.

4.5.1 Classical Modes of Deformation

Because of the centrosymmetry of the material under consideration, the symmetric stress-strain relationship can be decoupled in the form

$$\begin{bmatrix} \overline{S}_{11} \\ \overline{S}_{22} \\ \overline{S}_{12} \end{bmatrix} = \begin{bmatrix} \overline{C}_{11} & \overline{C}_{12} & 0 \\ \overline{C}_{21} & \overline{C}_{22} & 0 \\ 0 & 0 & \overline{C}_{33} \end{bmatrix} \begin{bmatrix} \overline{E}_{11} \\ \overline{E}_{22} \\ \overline{E}_{12} \end{bmatrix} \tag{4.16}$$

To evaluate the constants $\overline{C}_{11}, \overline{C}_{12}$, and $\overline{C}_{33}$, which correspond to the stiffness of a material in classical elasticity, a single strain $\overline{E}_{11}$, $\overline{E}_{22}$, and $\overline{E}_{12}$ will be applied on the RVE, one at a time. These strains can be any constant real numbers. The boundary conditions that need to be considered on the RVE analysis are:

(1) Apply $\overline{E}_{11}$:

$$u_1^{(k)} = \overline{E}_{11}x_1^{(k)} \tag{4.17a}$$

$$u_2^{(k)} = 0 \tag{4.17b}$$

$$\varphi_3^{(k)} = free \tag{4.17c}$$

(2) Apply $\overline{E}_{22}$:

$$u_1^{(k)} = 0 \tag{4.18a}$$

$$u_2^{(k)} = \overline{E}_{22} x_2^{(k)} \tag{4.18b}$$

$$\varphi_3^{(k)} = free \tag{4.18c}$$

(3) Apply $\overline{E}_{12} = \overline{E}_{21}$:

$$u_1^{(k)} = \overline{E}_{21} x_2^{(k)} \tag{4.19a}$$

$$u_2^{(k)} = \overline{E}_{12} x_1^{(k)} \tag{4.19b}$$

$$\varphi_3^{(k)} = free \tag{4.19c}$$

With these set of displacement and rotations defined above, the first there columns of $\overline{C}_{ij}$ can be evaluated one at a time. Also, because of isotropy, not all of them are independent ($\overline{C}_{12} = \overline{C}_{21}$ and $\overline{C}_{33} = \overline{C}_{11} - \overline{C}_{12}$), but for generality, all three cases will be considered to verify their dependence.

4.5.2 Micropolar Modes of Deformation

Similarly, the micropolar asymmetrical stress-strain and couple stress-curvature relationship can be reduced to

$$\begin{bmatrix} \overline{T}_{12} \\ \overline{M}_{13} \\ \overline{M}_{23} \end{bmatrix} = \begin{bmatrix} \overline{C}_{44} & 0 & 0 \\ 0 & \overline{C}_{55} & 0 \\ 0 & 0 & \overline{C}_{66} \end{bmatrix} \begin{bmatrix} \overline{A}_{12} \\ \overline{K}_{13} \\ \overline{K}_{23} \end{bmatrix} \tag{4.20}$$

(4) Apply $\overline{A}_{12} = -\overline{A}_{21}$:

$$u_1^{(k)} = -\overline{\Omega}_3 x_2^{(k)} \tag{4.21a}$$

$$u_2^{(k)} = \overline{\Omega}_3 x_1^{(k)} \tag{4.21b}$$

$$\varphi_3^{(k)} = \overline{\Omega}_3 - \overline{A}_{12} \tag{4.21c}$$

(5) Apply $\overline{K}_{13}$:

$$u_1^{(k)} = free \tag{4.22a}$$

$$u_2^{(k)} = free \tag{4.22b}$$

$$\varphi_3^{(k)} = \overline{K}_{13} x_1^{(k)} \tag{4.22c}$$

(6) Apply $\overline{K}_{23}$:

$$u_1^{(k)} = free \tag{4.23a}$$

$$u_2^{(k)} = free \tag{4.23b}$$

$$\varphi_3^{(k)} = \overline{K}_{23} x_2^{(k)} \tag{4.23c}$$

It should be emphasized that the deformation modes considered above are not unique. As discussed by [73], a different choice of boundary conditions will result in different approximation of the stiffness matrix. For our present analysis, the boundary conditions in [56] are considered. The only requirement in selecting the displacement and rotation fields, however, is for conditions in Eqn 4.13 to be satisfied. Because of this, in Eqns. 4.21, the global rotation $\overline{\Omega}_3$ is required to be specified, otherwise the balance of angular momentum will not be satisfied (Eqn 4.13d).

4.6 Closed Form Expressions for the Macroscopic Properties

The homogenization method considered will be applied to a hexagonally packed, circular cell honeycomb shown in Fig. 4.1. For the analysis of the RVE with the kinematic boundary conditions given in Eqns. 4.17- 4.23, a commercial finite element code, ABAQUS, will be used. In the analysis, the structural members will be modeled as uniform linear elastic Euler-Bernoulli arc beams. Because of this, we know that the material properties will depend on the Young's modulus E, cell wall thickness t, and arc radius R, with a unit thickness. The deformation of the cell walls will be dominated by bending. Because of this, for thin arc beams $(t/R) << 0.1$, we can guess the analytical or closed form solution to be in the form

$$\overline{\mu} = \alpha_{\mu} E \left(\frac{t}{R}\right)^3 \tag{4.24a}$$

$$\overline{\lambda} = \alpha_{\lambda} E \left(\frac{t}{R}\right)^3 \tag{4.24b}$$

$$\overline{\mu}_c = \alpha_{\mu_c} E \left(\frac{t}{R}\right)^3 \tag{4.24c}$$

$$\overline{\gamma}_c = \alpha_{\gamma_c} E \left(\frac{t}{R}\right) t^2 \tag{4.24d}$$

The above expressions are inspired through nondimensional analysis, where $\alpha_{\mu}, \alpha_{\lambda}, \alpha_{\mu_c}$, and α_{γ_c} are constants that are found through a single numerical experiment. For a given set of local material properties and geometries (E, t, R), the macroscopic material constants can be numerically evaluated. From this, the constant coefficients can be directly determined, which are

$$\alpha_{\mu} \approx 2.3060 \tag{4.25a}$$

$$\alpha_{\lambda} \approx 19.1496 \tag{4.25b}$$

$$\alpha_{\mu_c} \approx 0.3112 \tag{4.25c}$$

$$\alpha_{\gamma_c} \approx 0.1001 \tag{4.25d}$$

It should be noted the results above are valid for when bending is dominant in the case when $(t/R) << 0.1$. In such a case, axial and transverse effects can be neglected. However, when $(t/R) < 0.1$, axial deformations must be considered in Eqns. 4.24. In such a case, we can guess the form of the material constants to be of the form

$$\overline{\mu} = \left(\frac{1}{\alpha_\mu E \left(\frac{t}{R}\right)^3} + \frac{1}{\beta_\mu E \left(\frac{t}{R}\right)} \right)^{-1} \tag{4.26a}$$

$$\overline{\lambda} = \left(\frac{1}{\alpha_\lambda E \left(\frac{t}{R}\right)^3} + \frac{1}{\beta_\lambda E \left(\frac{t}{R}\right)} \right)^{-1} \tag{4.26b}$$

$$\overline{\mu}_c = \left(\frac{1}{\alpha_{\mu_c} E \left(\frac{t}{R}\right)^3} + \frac{1}{\beta_{\mu_c} E \left(\frac{t}{R}\right)} \right)^{-1} \tag{4.26c}$$

$$\overline{\gamma}_c = \alpha_{\gamma_c} E \left(\frac{t}{R}\right) t^2 \tag{4.26d}$$

In the above expressions, $\beta_\mu, \beta_\lambda, \beta_{\mu_c}$, and β_{γ_c} are nondimensional constant numbers. Similar to before, by assigning the local properties E, t, R and numerically evaluating the macroscopic properties $\overline{\mu}, \overline{\lambda}, \overline{\mu}_c$, and $\overline{\gamma}_c$, these constants can be calculated by considering the values found in Eqns. 4.25.

$$\beta_\mu \approx 0.1447 \tag{4.27a}$$

$$\beta_\lambda \approx 0.2436 \tag{4.27b}$$

$$\beta_{\mu_c} \approx 0.0345 \tag{4.27c}$$

In Eqn. 4.26d, axial deformation was determined not to influence $\overline{\gamma}_c$. This will also be discussed in the next section. Also, the closed form solutions above are for the structure in Fig. 4.1a where the arc beams are in a state of plane stress in the out

of plane direction. Plain strain results can be determined by replacing $E \rightarrow \frac{E}{(1-v^2)}$, where v is the Poisson's ratio.

4.7 Verification of the Constants

As discussed earlier, the constants $\overline{\mu}$ and $\overline{\lambda}$ correspond to the Lamé constants of classical elasticity. These can be compared with results obtained in [65], where the macroscopic Young's modulus and Poisson's ratio were determined by neglecting axial and transverse shear deformations. Using Eqns. 4.24a,b, we evaluate the Young's modulus and Poisson's ratio, respectively

$$\overline{E} = \frac{4\overline{\mu}(\overline{\lambda}+\overline{\mu})}{2\overline{\mu}+\overline{\lambda}} = 8.329E\left(\frac{t}{R}\right)^3 \tag{4.28a}$$

$$\overline{v} = \frac{\overline{\lambda}}{2\overline{\mu}+\overline{\lambda}} = 0.806 \tag{4.28b}$$

which are exactly the values reported by [65].

The closed form solutions in Eqns. 4.24 and 4.26 are validated by comparing them to the numerical predictions for different sets of local properties for the arc beams (E, R and t). In table 4.1, we consider 4 sets of local properties ($(I)-(IV)$) and evaluate the global material constants $\overline{\mu}, \overline{\lambda}, \overline{\mu}_c$, and $\overline{\gamma}_c$. In the numerical solution, the material constants are based upon the inclusion of bending, axial, and transverse shear deformations of the arc beams of the circular honeycomb structure. As stated earlier, in Eqn. 4.24 only bending is considered and in Eqn. 4.26 transverse shear deformation is neglected, while bending and axial deformations are present. As a result, the numerical calculations of the material constants are used as a benchmark when evaluating the error of the closed form solutions.

In the first two sets, the local properties of the arc beams are $E = 33MPa$ and $R = 2.6mm$, while the value of the thickness is $t = R/8$ and $t = R/38$ for set (I)

Table 4.1: Comparison of closed form solutions with numerical calculations.

Local Properties	Micropolar Constant	Numerical Calculations	Eqn.4.24		Eqn.4.26	
			Closed Form	% Error	Closed Form	% Error
(I)	$\overline{\mu}$ (MPa)	0.1190	0.1486	24.9	0.1190	0.0
E=33MPa	$\overline{\lambda}$ (MPa)	0.6067	1.2343	103.4	0.5539	8.7
R=2.6mm	$\overline{\mu}_c$ (MPa)	0.0176	0.0201	14.2	0.0176	0.0
t=R/8	$\overline{\gamma}_c$ (MPa$\times mm^2$)	0.0430	0.0436	1.4	-	-
(II) E=33MPa R=2.6mm t=R/38	$\overline{\mu}$ (MPa)	1.3715×10^{-3}	1.3868×10^{-3}	1.1	1.3717×10^{-3}	0.0
	$\overline{\lambda}$ (MPa)	11.0341×10^{-3}	11.5166×10^{-3}	4.4	10.9220×10^{-3}	1.0
	$\overline{\mu}_c$ (MPa)	0.1858×10^{-3}	0.1872×10^{-3}	0.8	0.1860×10^{-3}	0.1
	$\overline{\gamma}_c$ (MPa$\times mm^2$)	0.4068×10^{-3}	0.4070×10^{-3}	0.0	-	-
(III)	$\overline{\mu}$ (MPa)	0.2524	0.3153	24.9	0.2524	0.0
E=70MPa	$\overline{\lambda}$ (MPa)	1.2869	2.6181	103.4	1.1749	8.7
R=4.2mm	$\overline{\mu}_c$ (MPa)	0.0373	0.04255	14.1	0.0373	0.0
t=R/8	$\overline{\gamma}_c$ (MPa$\times mm^2$)	0.2379	0.2414	1.5	-	-
(IV) E=70MPa R=4.2mm t=R/38	$\overline{\mu}$ (MPa)	2.9091×10^{-3}	2.9418×10^{-3}	1.1	2.9096×10^{-3}	0.0
	$\overline{\lambda}$ (MPa)	23.4051×10^{-3}	24.4291×10^{-3}	4.4	23.1678×10^{-3}	1.0
	$\overline{\mu}_c$ (MPa)	0.3941×10^{-3}	0.3970×10^{-3}	0.7	0.3945×10^{-3}	0.1
	$\overline{\gamma}_c$ (MPa$\times mm^2$)	2.2517×10^{-3}	2.2526×10^{-3}	0.0	-	-

and (II), respectively. We see that for a thick arc in set (I), the error of Eqn. 4.24 is significantly high, especially for the value of $\overline{\lambda}$, which is 103.4%. This is expected, since for thick arcs, higher order thickness effects need to be considered. Because of this, Eqn. 4.26 gives much more accurate estimation. The error of $\overline{\lambda}$ in this closed form solution is 8.7%. Despite this error due to the transverse shear effects, this is a relatively accurate estimation for most engineering applications. In addition, it is seen that the closed form solution Eqn. 4.24 gives accurate estimation of the micropolar constant, $\overline{\gamma}_c$, from which we conclude that axial deformation does not influence its approximation.

In set (II), we see that the error of both closed form solutions decrease as the thickness of the arcs are smaller. In such a case, we see that Eqn. 4.24 gives an accurate estimation of the material constants, which are less than 5%, while Eqn. 4.26's error is less than 1%. The above conclusions are also made for sets (III) and (IV).

Next, we analyze the effect of changing the remaining local arc beam properties, E and R, while the thickness t is held fixed, by comparing set (I) with (III) or set (II) with (IV). It is seen that the % error does not change when comparing these sets. From this, we can conclude that the validity of Eqn. 4.24 and Eqn. 4.26 depend upon the thickness of the arcs (relative to the arc radius R). For slender arc beams ($R/t >> 1$), Eqn. 4.24 can be applied to estimate the material constants, while for thick beams ($R/t > 1$), Eqn. 4.24 applies since axial deformation is considered.

The plots of the macroscopic material properties, $\overline{\mu}, \overline{\lambda}, \overline{\mu}_c$, and $\overline{\gamma}_c$ against the thickness of the arcs, or R/t, is shown in Fig. 4.2, for $E = 70MPa$ and $R = 4.2mm$. We see that for large values of R/t (thin arcs) the material constants decrease, but for small values of R/t (thick arcs), the material properties are much larger. Thus, the structure at the global scale is much stiffer when the cells are thick. In addition, it is also observed from Fig. 4.2a,b,c that the closed form solutions in Eqn. 4.24 and Eqn. 4.26 diverge when the thickness increases. This divergence is more significant

for the Lamé constants, $\overline{\mu}$ and $\overline{\lambda}$, but the micropolar constants, $\overline{\mu}_c$ and $\overline{\gamma}_c$ are not sensitive to thickness effects.

4.8 Closed Form Solution of Grid Structure and Regular Hexagon Honeycomb

Next, the above analysis is applied to 2 structures most commonly analyzed in literature, which are the square grid structure and the regular hexagon honeycomb shown in Fig. 4.3. Unlike the circular honeycomb, where bending of the cell walls always dominate when $\left(\frac{t}{\ell}\right) << 1$, for these structures, the bending moments yield to axial deformations when the structure is under global strains $\overline{E}_{11}$ and $\overline{E}_{22}$. Also, attempting to express the constitutive relation Eqn. 4.5 in terms of the constants $\overline{\mu}$ and $\overline{\lambda}$ presents an ambiguity. To avoid this, we will simply present the constitutive relationship in terms of $\overline{C}_{ij}$ in Eqn. 4.14. First, we will consider the grid structure shown in Fig 4.3a. An interesting property of this structure is that it has a Poisson's ratio equivalent to zero at the global scale. The estimations of the stiffness matrix of this structure available in literature is shown in table 4.2. The classical elasticity properties are given by [27]. In this analysis, the material properties show that when this structure is under a tension/compression loading, the deformation is dictated by the axial deformation of the beam members. This results in the the dependence of $\overline{C}_{11} = \overline{C}_{22}$ being proportional to $\left(\frac{t}{\ell}\right)$. In addition, because the grid members are modeled as beams, there is no lateral deformation, from which we obtain $\overline{C}_{12} = \overline{C}_{21} = 0$ or Poisson's ratio is zero. For the structure under shear loading, the shear modulus, $\overline{C}_{33}$, is dependent on $\left(\frac{t}{\ell}\right)^3$ because the grid members are bent.

In literature, a popular method of determining the micropolar constants has been to extend the Born-Von Karmon model of characterizing a classical continuum with linear springs to modeling a lattice with beams as a micropolar continuum [69].

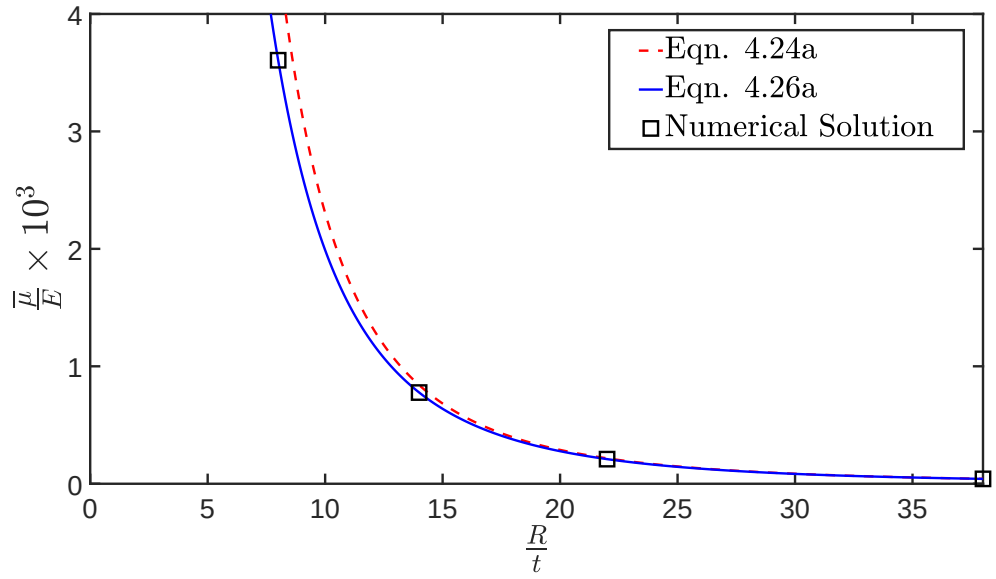
Eqn. 4.24a
Eqn. 4.26a
Numerical Solution
$\frac{\overline{\mu}}{E} \times 10^3$
$\frac{R}{t}$
0
1
2
3
4
0
5
10
15
20
25
30
35

(a)

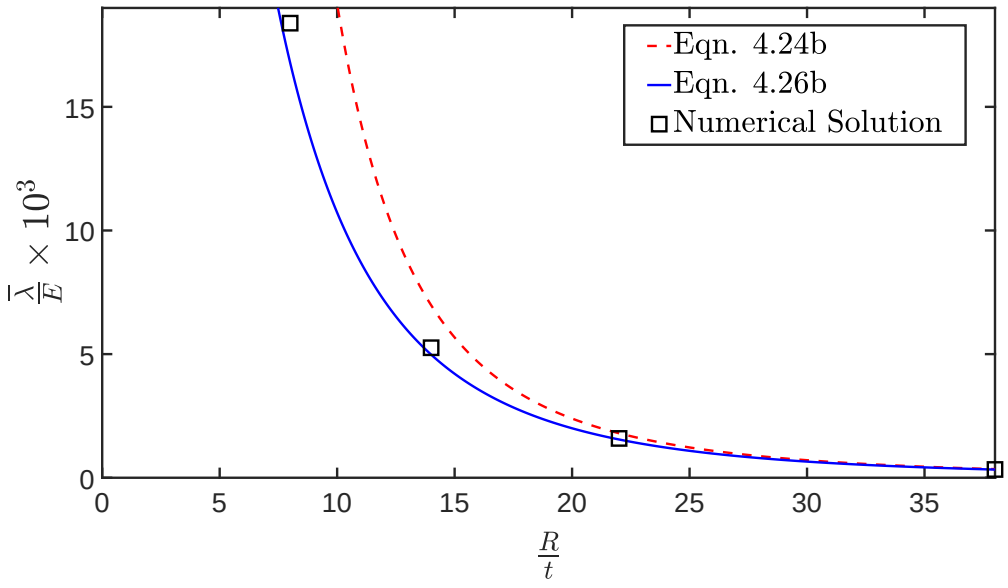
Eqn. 4.24b
Eqn. 4.26b
Numerical Solution
$\frac{\overline{\lambda}}{E} \times 10^3$
$\frac{R}{t}$
0
5
10
15
0
5
10
15
20
25
30
35

(b)

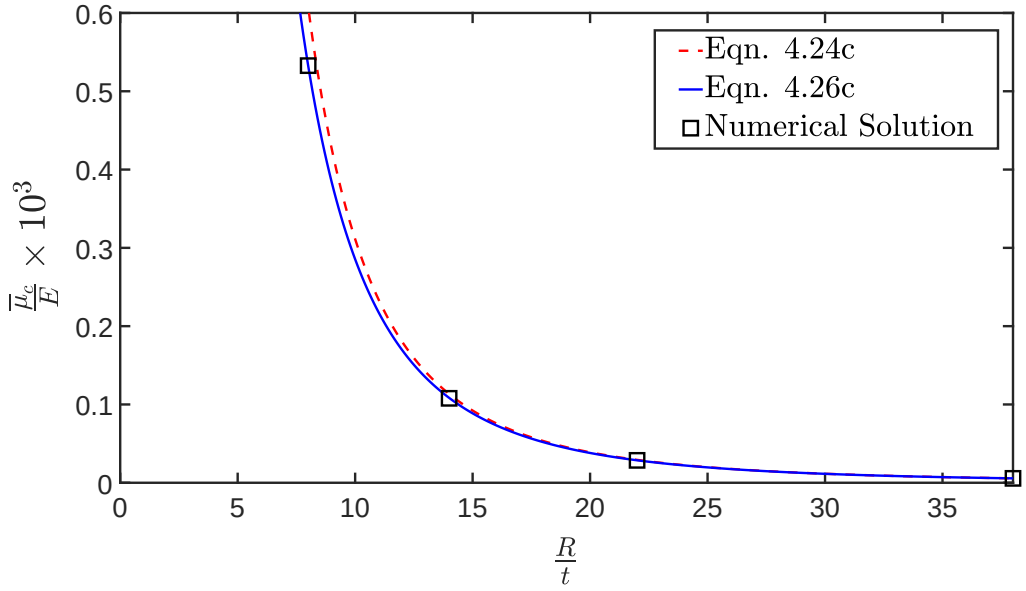

(c)

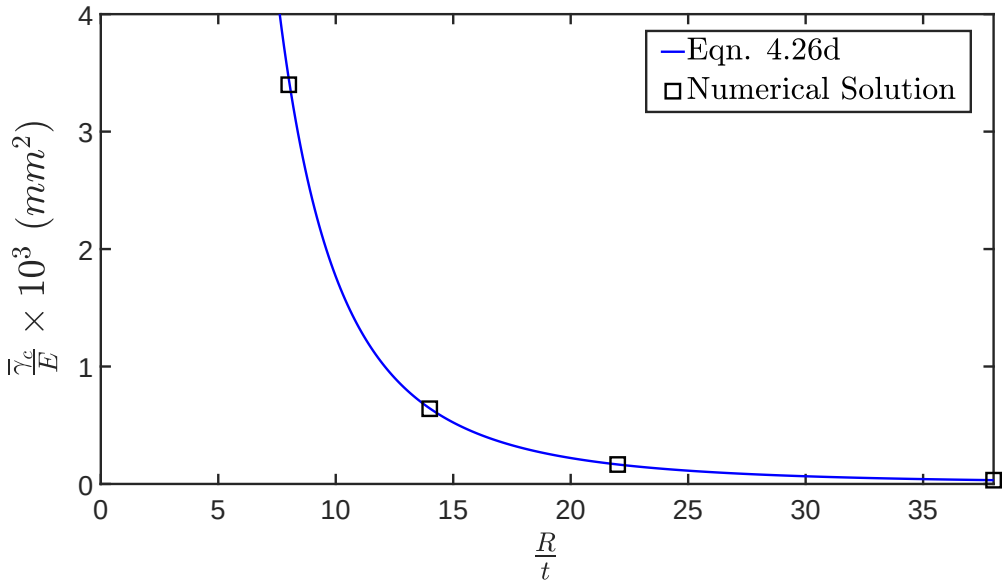

(d)

Figure 4.2: Effect of thickness t on material constants (a) $\overline{\mu}$, (b) $\overline{\lambda}$, (c) $\overline{\mu}_c$, and (d) $\overline{\gamma}_c$.

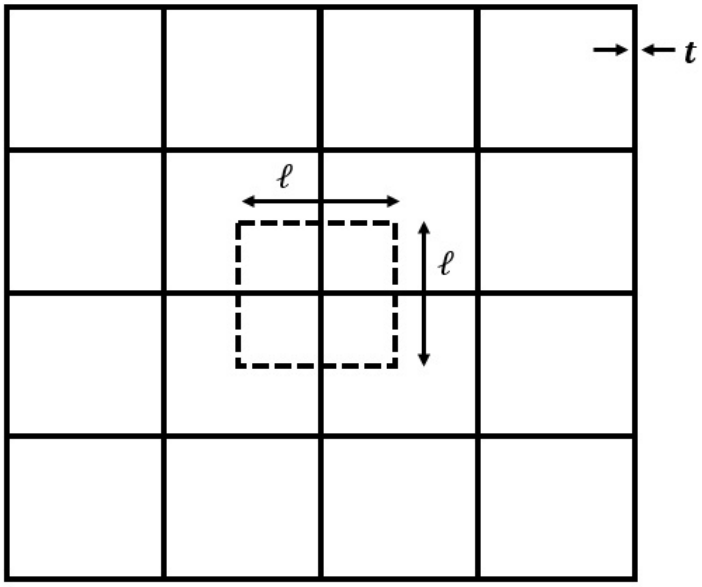

(a)

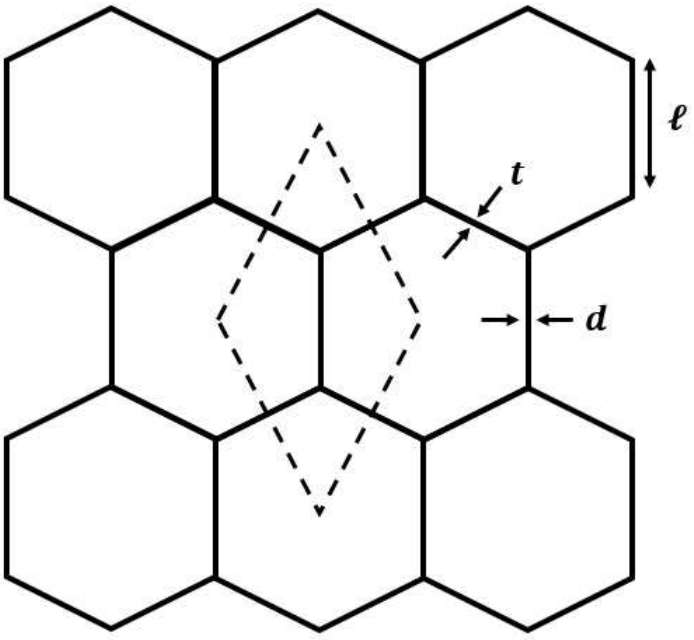

(b)

Figure 4.3: (a) grid and (b) regular hexagon structures along with their RVE under consideration.

Table 4.2: Stiffness matrix of a grid structure when $\frac{t}{\ell} << 1$.

Material Constants	Gibson and Ashby [27]	Chen et al. [69]	Nondimensional analysis	
			Closed Form	% Error: (E=70MPa, $\ell = 4.2mm, t = \ell/8$)
$\overline{C}_{11} = \overline{C}_{22}$	$E\left(\frac{t}{\ell}\right)$	$E\left(\frac{t}{\ell}\right)$	$E\left(\frac{t}{\ell}\right)$	0.0
$\overline{C}_{12} = \overline{C}_{21}$	0	0	0	0.0
$\overline{C}_{33}$	$E\left(\frac{t}{\ell}\right)^3$	$E\left(\frac{t}{\ell}\right)^3$	$E\left(\frac{t}{\ell}\right)^3$	3.7
$\overline{C}_{44}$	$*$	$E\left(\frac{t}{\ell}\right)^3$	$E\left(\frac{t}{\ell}\right)^3$	3.7
$\overline{C}_{55} = \overline{C}_{66}$	$*$	$\frac{1}{3}E\left(\frac{t}{\ell}\right)t^2$	$\frac{1}{12}E\left(\frac{t}{\ell}\right)t^2$	0.0

Through this, it is possible to express the constitutive relationship of the structure in terms of the local beam properties. However, this method has often been criticized, because the approximations of the material properties only retain first order terms when applying a Taylor series to express the discrete lattice as a continuum [67] and by considering higher order terms, the material constants $\overline{C}_{55} = \overline{C}_{66}$ do not converge. Despite this, in literature, this paradox is often ignored and only first order terms are considered, as in table 4.2. In the third column, the values reported by [69] using this method are shown.

In the last column, the same method used on the circular honeycomb to determine the closed form solution of the material constants is applied to the grid structure. The closed form solution, along with the % error when $\frac{t}{\ell} = \frac{1}{8}$ is shown. In determining % error, the closed form solution is compared with the numerical evaluation of the material properties, where axial, bending, and transverse shear deformation are all simultaneously considered. Because the error of the closed form solution is small (3.7% for $\overline{C}_{33}, \overline{C}_{44}$), it is validated that only axial deformation dominates the material constants $\overline{C}_{11} = \overline{C}_{22}$ and only bending dominates $\overline{C}_{33}$, $\overline{C}_{44}$, and $\overline{C}_{55} = \overline{C}_{66}$.

The same analysis is applied to the regular hexagon honeycomb. For this structure, we will consider two different cases, where 1) cell wall thickness is uniform ($d = t$)

and 2) thickness of the vertical walls are twice the thickness of the inclined walls ($d = 2t$). The latter case is considered because it is easier to produced a hexagonal honeycomb by partially bonding sheets and expanding them to form the structure seen above [76]. Because of this manufacturing method, the double wall honeycomb is a much more common structure. However, with the recent advances in 3D printing, the manufacturing of a single wall honeycomb is also becoming more practical.

The reported values of a single wall honeycomb structure are shown in table 4.3 for $\frac{t}{\ell} << 1$. The elasticity constants have previously been given by [27]. Similar to before, the dependence of $\overline{C}_{11} = \overline{C}_{22}$ and $\overline{C}_{12} = \overline{C}_{21}$ on $\left(\frac{t}{\ell}\right)$ is due to axial deformations dominating these material constants when $\frac{t}{\ell} << 1$, while $\overline{C}_{33}$ is proportional to $\left(\frac{t}{\ell}\right)^3$ because of bending of the beams. These values have been extensively analyzed and validated by numerous experimental results. Due to this, the validity of the Taylor series approach is in question, because the elasticity constants reported by [69] does not match with [27]. In addition, the material constant $\overline{C}_{33}$ is proportional to $\left(\frac{t}{\ell}\right)$.

For this structure, the micropolar material constants proposed by [70] has often been accepted as the norm. In this method, the RVE under consideration is shown in Fig. 4.3b. The elasticity constants of this approach match with [27]. However, in this method, the authors have assumed that the rigid joints of the honeycomb are restricted from rotating, which influences the evaluation of the material constant, $\overline{C}_{44}$. In our present analysis, we relax this assumption, which allows us to obtain a softer value of $\overline{C}_{44}$. As it is seen, the remaining material constants of our approach match exactly with [70].

Next, we seek to determine the validity of the closed form solutions for a thick beam lattice $\left(\frac{t}{\ell} = \frac{1}{8}\right)$. Similar to the previous structures, we compare the closed form solution with the numerical evaluation of these constants when axial, bending, and transverse shear deformations are all present. From table 4.3, we see that higher order effects are present for thick beams, but they cause the highest influence on the material

constant, $\overline{C}_{44}$, which has an error of 6.7%. For most engineering applications, this amount of error is acceptable considering the simplicity of the closed form solution for a thick beam lattice.

Next, we determine the material constants of the double walled honeycomb. The classical elasticity constants for this structure have been summarized by [76]. In this work, they report that this material is in fact anisotropic, $\overline{C}_{11} \neq \overline{C}_{22}$, but as the thickness of the walls decreases, ($\frac{t}{\ell} << 1$), these two constants approach each other. The elasticity constants of this material is summarized in table 4.4, in addition to the closed form solution determined by using nondimensional analysis. As it is seen, the classical elasticity constants match, however, there is a discrepancy between the reported values of $\overline{C}_{33}$. After considering this, it was determined that the shear modulus reported is based off the assumption that the moment of inertia of the double walled region is twice the moment of inertia of the single walled inclined beams, which is incorrect. Because of this, our value of $\overline{C}_{33}$ is correct. In addition, it is seen that for this structure, the anisotropy in $\overline{C}_{55}$ and $\overline{C}_{66}$ is significant. It should be stated that the micropolar constants of a double wall honeycomb reported here are expressed for the first time.

In addition, we verify the error in the closed form solution produced by thickness effects. Again, we consider a thick beam with $\frac{t}{\ell} = \frac{1}{8}$. The error is mostly significant in the material constant $\overline{C}_{44}$, which is 11.3%. In addition, the error calculated in the classical elasticity constants $\overline{C}_{11}$ and $\overline{C}_{22}$ also takes in account the assumption that these two values are equal and the classical elasticity constants are isotropic. These errors are less than 4%, which indicates that the classical elasticity constants can be approximated to be isotropic even for thick beams.

Table 4.3: Stiffness matrix of a regular hexagon honeycomb when $\frac{t}{\ell} << 1$ and $d = t$.

Material Constants	Gibson and Ashby [27]	Chen et al. [69]	Wang and Stronge [70]	Nondimensional analysis	
				Closed Form	% Error: (E=70MPa, $\ell = 4.2mm, t = \ell/8$)
$\overline{C}_{11} = \overline{C}_{22}$	$0.29E\left(\frac{t}{\ell}\right)$	$0.4330E\left(\frac{t}{\ell}\right)$	$0.2887E\left(\frac{t}{\ell}\right)$	$0.2887E\left(\frac{t}{\ell}\right)$	2.9
$\overline{C}_{12} = \overline{C}_{21}$	$0.29E\left(\frac{t}{\ell}\right)$	$0.4330E\left(\frac{t}{\ell}\right)$	$0.2887E\left(\frac{t}{\ell}\right)$	$0.2887E\left(\frac{t}{\ell}\right)$	3.1
$\overline{C}_{33}$	$1.15E\left(\frac{t}{\ell}\right)^3$	$0.2887E\left(\frac{t}{\ell}\right)$	$1.1547E\left(\frac{t}{\ell}\right)^3$	$1.1547E\left(\frac{t}{\ell}\right)^3$	5.2
$\overline{C}_{44}$	$*$	$0.5774E\left(\frac{t}{\ell}\right)^3$	$0.5774E\left(\frac{t}{\ell}\right)^3$	$0.4199E\left(\frac{t}{\ell}\right)^3$	6.7
$\overline{C}_{55} = \overline{C}_{66}$	$*$	$0.1925E\left(\frac{t}{\ell}\right)t^2$	$0.0481E\left(\frac{t}{\ell}\right)t^2$	$0.0481E\left(\frac{t}{\ell}\right)t^2$	0.0

Table 4.4: Stiffness matrix of a regular hexagon honeycomb when $\frac{t}{\ell} << 1$ and $d = 2t$.

Material Constants	Hohe and Becker [76]	Nondimensional analysis	
		Closed Form	% Error: (E=70MPa, $\ell = 4.2mm, t = \ell/8$)
$\overline{C}_{11}$	$0.35E\left(\frac{t}{\ell}\right)$	$0.3466E\left(\frac{t}{\ell}\right)$	1.5
$\overline{C}_{11}$	$0.35E\left(\frac{t}{\ell}\right)$	$0.3466E\left(\frac{t}{\ell}\right)$	1.5
$\overline{C}_{22}$	$0.35E\left(\frac{t}{\ell}\right)$	$0.3466E\left(\frac{t}{\ell}\right)$	3.4
$\overline{C}_{12} = \overline{C}_{21}$	$0.35E\left(\frac{t}{\ell}\right)$	$0.3460E\left(\frac{t}{\ell}\right)$	2.3
$\overline{C}_{33}$	$1.15E\left(\frac{t}{\ell}\right)^3$	$2.7595E\left(\frac{t}{\ell}\right)^3$	9.2
$\overline{C}_{44}$	$*$	$0.4784E\left(\frac{t}{\ell}\right)^3$	11.3
$\overline{C}_{55}$	$*$	$0.0481E\left(\frac{t}{\ell}\right)t^2$	0.0
$\overline{C}_{66}$	$*$	$0.1155E\left(\frac{t}{\ell}\right)t^2$	0.0

4.9 Conclusions

In this chapter, we discussed a recent micromechanics approach proposed by [55] and applied it to determine the micropolar constants of a hexagonally packed circular cell honeycomb, a grid structure, and a regular hexagon honeycomb with uniform as well as non-uniform wall thickness. In order to determine the closed form solution of the constitutive relation, we resorted to nondimensional analysis, were we first assumed the form of these expressions and used numerical analysis to determine the one unknown multiplicative constant. It should be noted that these expressions could have been derived analytically by solving the governing equations, but in order to simplify our analysis, we resorted to nondimensional analysis. It has been shown that the numerical error in our closed form solutions were negligible. They are only sensitive to the slenderness of the cell walls. This is due to higher order shear effects which develop in thick and short beams. However, for most engineering applications, our closed form solutions are practical, since it has been demonstrated for extreme cases of $t = R/8$ (or $t = \ell/8$) the error produced by these higher order shear effects are approximately 10.0%. In addition, we compared our expressions of the material constants to those available in literature. It is concluded that the methods applied can effectively determine the classical and micropolar properties of cellular solids.

CHAPTER 5

On the Buckling of a 2D Micropolar Strip

5.1 Introduction

In literature, various analytical solutions have been produced for linear micropolar theory [5], [6], [7], [77], [78], etc. However, analytical solutions pertaining to the geometric nonlinear region is limited. The challenge lies in the finite micropolar strain/curvature and displacement/rotation relation. Unlike in classical finite elasticity, where the Green-Lagrange strain measure is second order nonlinear in displacement, the proposed finite micropolar theory will be shown to be of infinite order because of trigonometric relation in the kinematics. In addition, in finite micropolar theory, by neglecting the length scales in the constitutive relation, the theory does not always reduce to finite elasticity. As a result, classical solutions cannot always be extracted from the general micropolar theory [45], [44]. In the previous chapters, in order to avoid such complications, geometric nonlinearity was introduced by assuming only the symmetric component of the strain tensor is nonlinear (Eqn. 2.62). This chapter instead examines the geometrically exact micropolar theory. An analytical solution of a 2D micropolar strip, under compression is obtained, which leads to a closed-form solution for buckling. In doing so, the effects of the additional micropolar material constants on the buckling load are analyzed. In the limiting case, when the thickness of the 2D strip becomes small in comparison to the overall length of

the structure, the micropolar beam equations are obtained. In the following chapter, the micropolar beam theory is also developed based on the geometric exact strain measures. In literature, simple micropolar beam theories have been proposed, for example in [79], [80], [81]. These beam theories have potential applications to micro-electromechanical systems (MEMS), where the relative size of the microstructure to the overall size of the structure is comparable.

5.2 Finite Micropolar Theory

The formulation of the finite micropolar theory can be found in [42], [43], [82], [83]. In considering the asymmetric stress ($\boldsymbol{\Sigma}$) and couple-stress ($\boldsymbol{M}$) tensors, conjugate asymmetric strains need to be defined. For this, we refer to the deformation gradient defined earlier

$$\boldsymbol{F} = \frac{\partial \boldsymbol{x}}{\partial \boldsymbol{X}} \tag{5.1}$$

which can also be expressed in terms of the asymmetric stretch tensor $\boldsymbol{U}$ and the kinematically independent microrotation tensor $\boldsymbol{R}$ ($\boldsymbol{R} \in SO(3)$)

$$\boldsymbol{F} = \boldsymbol{R} \cdot \boldsymbol{U} \tag{5.2}$$

In solving for the stretch tensor,

$$\boldsymbol{U} = \boldsymbol{R}^{-1} \cdot \boldsymbol{F} \tag{5.3}$$

or, by considering Rodrigues rotation formula in Eqn. 2.6, it simplifies to

$$U_{KL} = x_{k,K} \left(\cos\theta \delta_{kL} + (1 - \cos\theta) \frac{\varphi_k \varphi_l}{\theta^2} \delta_{lL} - \sin\theta \epsilon_{klm} \frac{\varphi_m}{\theta} \delta_{lL} \right)$$

In addition, the wryness tensor is defined

$$\Upsilon_{KL} = \theta_{,L}\frac{\varphi_k}{\theta}\delta_{kK} + \sin\theta\left(\frac{\varphi_k}{\theta}\right)_{,L}\delta_{kK} - (1-\cos\theta)\epsilon_{KMN}\frac{\varphi_k}{\theta}\left(\frac{\varphi_l}{\theta}\right)_{,L}\delta_{kM}\delta_{lN}$$

In the above equations, $x_k = X_K\delta_{Kk} + u_k$, $\theta = (\varphi_1^2 + \varphi_2^2 + \varphi_3^2)^{1/2}$, where X_K and x_k are the coordinates of a point in the material in the undeformed and deformed configuration, respectively, u_k and φ_k are the displacement and rotation vectors, respectively. For notational consistency with the previous chapters, we will use $\mathbf{\Gamma}$ to notate the stretch tensor $\boldsymbol{U}$ (or $\mathbf{\Gamma} = \boldsymbol{U}$). In addition, the wryness tensor is related to the curvature tensor by $\boldsymbol{K} = \mathbf{\Upsilon}^T$. It should be highlighted that these strain measures are trigonometric functions of dispacements/rotations, thus highly nonlinear. In proceeding, through a Taylor series expansion, they reduce in

$$\Gamma_{KL} = u_{L,K} - \epsilon_{KLM}\varphi_M - \frac{1}{2}\theta^2\delta_{KL} + \frac{1}{2}\varphi_K\varphi_L - \epsilon_{FLM}\varphi_M u_{F,K} + O(3) \tag{5.4a}$$

$$\Upsilon_{KL} = \varphi_{K,L} - \frac{1}{2}\epsilon_{KMN}\varphi_M\varphi_{N,L} + O(3) \tag{5.4b}$$

In applying perturbation method to obtain the linearized equations for buckling, it will be shown that only second order nonlinear terms are of relevance. Thus, finite micropolar theory is solvable for these classes of problems.

According to [82], [83], the micropolar strain energy density is defined as $\overline{U}(\mathbf{\Gamma}, \mathbf{\Upsilon})$. For a general (3D) isotropic micropolar material, it is expressed in terms of the invariants

$$\overline{U}(\mathbf{\Gamma}, \mathbf{\Upsilon}) = \frac{\lambda}{2}I_1^2 + \mu I_2 + (\mu + k)I_3 + \frac{\alpha}{2}I_4^2 + \beta I_5 + \gamma I_6 \tag{5.5}$$

$\lambda, \mu, k, \alpha, \beta$, and γ are material constants and the invariants are

$$I_1 = \Gamma_{ii} \tag{5.6a}$$

$$I_2 = \frac{1}{2}\Gamma_{ij}\Gamma_{ji} \tag{5.6b}$$

$$I_3 = \frac{1}{2}\Gamma_{ij}\Gamma_{ij} \tag{5.6c}$$

$$I_4 = \Upsilon_{ii} \tag{5.6d}$$

$$I_5 = \frac{1}{2}\Upsilon_{ij}\Upsilon_{ji} \tag{5.6e}$$

$$I_6 = \frac{1}{2}\Upsilon_{ij}\Upsilon_{ij} \tag{5.6f}$$

The total potential energy of a micropolar system is defined as

$$\Pi = U - W \tag{5.7}$$

where $U = \int_V \overline{U} dV$ is the total strain energy and W is the external work.

5.3 Problem Formulation

The geometry of the problem under consideration is shown in Fig. 5.1. A strip of material is subjected to uniaxial compression stress σ along the x_1 direction and deforms in the x_1-x_2 plane. A plane strain condition is assumed. For a 2D solid, the significant displacement components take the form, $u_1 = u_1(x_1, x_2)$, and $u_2 = u_2(x_1, x_2)$. In addition, the local rotation of the material has the form, $\varphi_3 = \varphi_3(x_1, x_2)$. The strip thickness is $2h$ and its length is a. For mathematical simplicity, the range of the solid in the x_1 direction will be $-\infty < x_1 < \infty$, but the deformation is assumed to be periodic with a wavelength $L = 2a$. This facilitates, as shown in [4], for the corresponding classical elasticity solution with thickness effects. In this boundary value problem, for equilibrium, the potential energy must be stationary ($\delta\Pi = 0$), or

$$\begin{aligned}\delta\Pi = 0 = \delta U - \delta W = \int_V [((2\mu + \lambda + k)\Upsilon_{11} + \lambda\Upsilon_{22})\delta\Upsilon_{11} + \\ ((2\mu + \lambda + k)\Upsilon_{22} + \lambda\Upsilon_{11})\delta\Upsilon_{22} + (\mu\Upsilon_{21} + (\mu + k)\Upsilon_{12})\delta\Upsilon_{12} + \\ (\mu\Upsilon_{12} + (\mu + k)\Upsilon_{21})\delta\Upsilon_{21} + \gamma K_{13}\delta K_{13} + \gamma K_{23}\delta K_{23}]dV - \int_A \sigma\delta u_1 \ell dS\end{aligned} \tag{5.8}$$

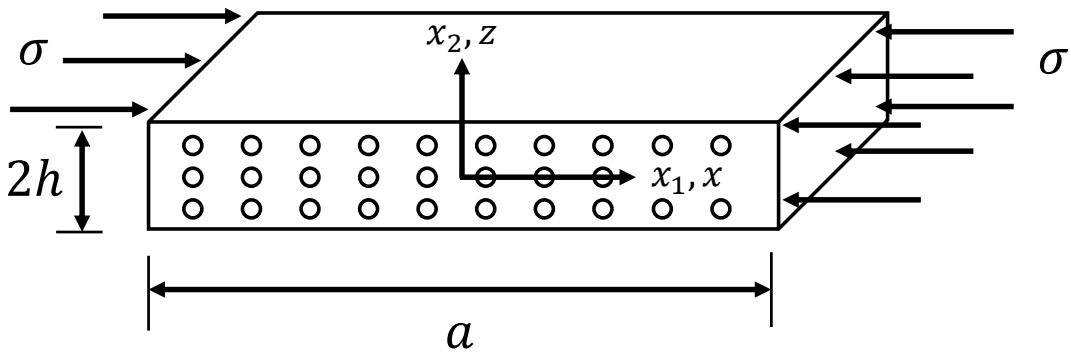

Figure 5.1: Configuration of the problem studied.

Following the procedure of the variational approach, the nonlinear equilibrium equations result in

$$\frac{\partial(\Sigma_{11}-\varphi_3\Sigma_{12})}{\partial x_1}+\frac{\partial(\Sigma_{21}-\varphi_3\Sigma_{22})}{\partial x_2}=0 \tag{5.9a}$$

$$\frac{\partial(\Sigma_{12}+\varphi_3\Sigma_{11})}{\partial x_1}+\frac{\partial(\Sigma_{22}+\varphi_3\Sigma_{21})}{\partial x_2}=0 \tag{5.9b}$$

$$\frac{\partial M_{13}}{\partial x_1}+\frac{\partial M_{23}}{\partial x_2}+(\Sigma_{12}+\varphi_3\Sigma_{11})-(\Sigma_{21}-\varphi_3\Sigma_{22})+ \tag{5.9c}$$
$$\frac{\partial u_1}{\partial x_1}\Sigma_{12}+\frac{\partial u_1}{\partial x_2}\Sigma_{22}-\frac{\partial u_2}{\partial x_1}\Sigma_{11}-\frac{\partial u_2}{\partial x_2}\Sigma_{21}=0$$

Eqn. 5.9a,b correspond to the conservation of linear momentum and Eqn. 5.9c to the conservation of angular momentum. The corresponding boundary conditions are

$$(\Sigma_{11}-\varphi_3\Sigma_{12}-\sigma)\ell+(\Sigma_{21}-\varphi_3\Sigma_{22})m=0 \tag{5.10a}$$

$$(\Sigma_{12}+\varphi_3\Sigma_{11})\ell+(\Sigma_{22}+\varphi_3\Sigma_{21})m=0 \tag{5.10b}$$

$$M_{13}\ell+M_{23}m=0 \tag{5.10c}$$

In Eqn. 5.8 and 5.10, $\ell=\cos(\vec{n},x_1)$, $m=\cos(\vec{n},x_2)$ are directional cosines between the normal vector $\vec{n}$ corresponding to a surface and the basis vector along the coordinate axis x_i. From Eqn. 5.4, the 2D strains in terms of displacements and local

rotation are

$$\Gamma_{11} = u_{1,1} - \frac{\varphi_3^2}{2} + \varphi_3 u_{2,1} + O(3) \tag{5.11a}$$

$$\Gamma_{22} = u_{2,2} - \frac{\varphi_3^2}{2} - \varphi_3 u_{1,2} + O(3) \tag{5.11b}$$

$$\Gamma_{12} = u_{2,1} - \varphi_3 - \varphi_3 u_{1,1} + O(3) \tag{5.11c}$$

$$\Gamma_{21} = u_{1,2} + \varphi_3 + \varphi_3 u_{2,2} + O(3) \tag{5.11d}$$

$$K_{13} = \varphi_{3,1} + O(3) \tag{5.11e}$$

$$K_{23} = \varphi_{3,2} + O(3) \tag{5.11f}$$

For a linear, isotropic micropolar solid, the constitutive relations between the stresses and the strains are,

$$\Sigma_{11} = (2\mu + \lambda + k)\Gamma_{11} + \lambda\Gamma_{22} \tag{5.12a}$$

$$\Sigma_{22} = (2\mu + \lambda + k)\Gamma_{22} + \lambda\Gamma_{11} \tag{5.12b}$$

$$\Sigma_{12} = (\mu + k)\Gamma_{12} + \mu\Gamma_{21} \tag{5.12c}$$

$$\Sigma_{21} = (\mu + k)\Gamma_{21} + \mu\Gamma_{12} \tag{5.12d}$$

$$M_{13} = \gamma K_{13} \tag{5.12e}$$

$$M_{23} = \gamma K_{23} \tag{5.12f}$$

Because of the principle of nonnegative internal energy, the micropolar constants λ, μ, k, γ in the constitutive relation must satisfy the inequalities,

$$0 \leq 3\lambda + 2\mu + k \tag{5.13a}$$

$$0 \leq 2\mu + k \tag{5.13b}$$

$$0 \leq k \tag{5.13c}$$

$$0 \leq \gamma \tag{5.13d}$$

In Eqn. 5.12, 5.13, it is seen that in 2D, a micropolar material is characterized by 4 material constants instead of 2 as in classical elasticity, and by setting the micropolar constants, γ, k to zero, the constitutive relation reduces to that of classical elasticity and λ, μ correspond to the Lamé constants. This fact will be used to recover the classical elasticity solution from the general micropolar solution for comparison of the two continuum theories.

5.4 Buckling Equations

In deriving the buckling equations of a micropolar solid, the equilibrium equations are first expressed in terms of displacements by using Eqns. 5.9, 5.11, and 5.12.

$$
\begin{aligned}
&(2\mu+\lambda+k)\frac{\partial^2 u_1}{\partial x_1^2}+(\mu+\lambda)\frac{\partial^2 u_2}{\partial x_1\partial x_2}+(\mu+k)\frac{\partial^2 u_1}{\partial x_2^2}\\
&+k\frac{\partial \varphi_3}{\partial x_2}-2\left(\mu+\lambda-\frac{k}{2}\right)\varphi_3\frac{\partial \varphi_3}{\partial x_1}\\
&+(\mu+\lambda)\frac{\partial \varphi_3}{\partial x_1}\left(\frac{\partial u_2}{\partial x_1}-\frac{\partial u_1}{\partial x_2}\right)\\
&+(\mu+\lambda)\varphi_3\left(\frac{\partial^2 u_2}{\partial x_1^2}-\frac{\partial^2 u_2}{\partial x_2^2}-2\frac{\partial^2 u_1}{\partial x_1 x_2}\right)-\\
&(\mu+\lambda)\frac{\partial \varphi_3}{\partial x_2}\left(\frac{\partial u_1}{\partial x_1}+\frac{\partial u_2}{\partial x_2}\right)+O(3)=0
\end{aligned}
\tag{5.14a}
$$

$$
\begin{aligned}
&(\mu+\lambda)\frac{\partial^2 u_1}{\partial x_1\partial x_2}+(\mu+k)\frac{\partial^2 u_2}{\partial x_1^2}+(2\mu+\lambda+k)\frac{\partial^2 u_2}{\partial x_2^2}\\
&-k\frac{\partial \varphi_3}{\partial x_1}-2\left(\mu+\lambda-\frac{k}{2}\right)\varphi_3\frac{\partial \varphi_3}{\partial x_2}\\
&+(\mu+\lambda)\frac{\partial \varphi_3}{\partial x_1}\left(\frac{\partial u_1}{\partial x_1}+\frac{\partial u_2}{\partial x_2}\right)+\\
&(\mu+\lambda)\varphi_3\left(\frac{\partial^2 u_1}{\partial x_1^2}-\frac{\partial^2 u_1}{\partial x_2^2}+2\frac{\partial^2 u_2}{\partial x_1\partial x_2}\right)\\
&-(\mu+\lambda)\frac{\partial \varphi_3}{\partial x_2}\left(\frac{\partial u_1}{\partial x_2}-\frac{\partial u_2}{\partial x_1}\right)+O(3)=0\\
&\gamma\left(\frac{\partial^2 \varphi_3}{\partial x_1^2}+\frac{\partial^2 \varphi_3}{\partial x_2^2}\right)+k\left(\frac{\partial u_2}{\partial x_1}-\frac{\partial u_1}{\partial x_2}-2\varphi_3\right)
\end{aligned}
\tag{5.14b}
$$

$$+2\left(\mu+\lambda-\frac{k}{2}\right)\varphi_3\left(\frac{\partial u_1}{\partial x_1}+\frac{\partial u_2}{\partial x_2}\right)+ \tag{5.14c}$$
$$(\mu+\lambda)\left(\frac{\partial u_1}{\partial x_1}\frac{\partial u_1}{\partial x_2}+\frac{\partial u_2}{\partial x_2}\frac{\partial u_1}{\partial x_2}-\frac{\partial u_1}{\partial x_1}\frac{\partial u_2}{\partial x_1}-\frac{\partial u_2}{\partial x_1}\frac{\partial u_2}{\partial x_2}\right)$$
$$+O(3)=0$$

Next, the displacement and rotational fields are perturbed: $u_1 = u_1^0 + \bar{\lambda}u_1'$, $u_2 = u_2^0+\bar{\lambda}u_2'$, and $\varphi_3 = \varphi_3^0+\bar{\lambda}\varphi_3'$, where $\bar{\lambda}$ identifies the buckled state and u_1^0, u_2^0, φ_3^0 are the known linear prebuckled displacement and rotational solutions. The equations above are linearized by substituting the perturbed kinematics into the equations above. To linearize, only first order terms of $\bar{\lambda}$ are kept. Thus, the higher order polynomial terms associated with $O(3)$ are irrelevant.

In the prebuckled state, the only nonzero stress in Fig. 5.1 is $\Sigma_{11}^0 = -\sigma$. From this, the displacement and rotation fields are,

$$u_1^0 = -\frac{(2\mu+\lambda+k)\sigma}{(2\mu+\lambda+k)^2-\lambda^2}x_1 = -\frac{(1-v_m^2)\sigma}{E_m}x_1 \tag{5.15a}$$
$$u_2^0 = \frac{\lambda\sigma}{(2\mu+\lambda+k)^2-\lambda^2}x_2 = \frac{v_m(1+v_m)\sigma}{E_m}x_2 \tag{5.15b}$$
$$\varphi_3^0 = 0 \tag{5.15c}$$

In Eqn. 5.15, $E_m = (2\mu+k)(3\lambda+2\mu+k)(2\lambda+2\mu+k)^{-1}$ and $v_m = \lambda(2\mu+2\lambda+k)^{-1}$, which represent the micropolar Young's modulus and Poisson's ratio, [84], respectively.

Introducing the perturbations in Eqn. 5.14, and considering Eqn. 5.15, the buckling equations are,

$$(2\mu+\lambda+k)\frac{\partial^2 u}{\partial x^2}+(\mu+\lambda)\frac{\partial^2 w}{\partial x\partial z}+(\mu+k)\frac{\partial^2 u}{\partial z^2}+A_1\frac{\partial\varphi}{\partial z}=0 \tag{5.16a}$$
$$(\mu+\lambda)\frac{\partial^2 u}{\partial x\partial z}+(2\mu+\lambda+k)\frac{\partial^2 w}{\partial z^2}+(\mu+k)\frac{\partial^2 w}{\partial x^2}-A_1\frac{\partial\varphi}{\partial x}=0 \tag{5.16b}$$
$$\gamma\frac{\partial^2\varphi}{\partial x^2}+\gamma\frac{\partial^2\varphi}{\partial z^2}-A_1\frac{\partial u}{\partial z}+A_1\frac{\partial w}{\partial x}-A_2\varphi=0 \tag{5.16c}$$

where,

$$A_1 = k + \frac{\sigma(\mu+\lambda)(2\mu+k)}{(2\mu+\lambda+k)^2-\lambda^2} \tag{5.17a}$$

$$A_2 = \frac{2k^2+2\sigma(\mu+\lambda)+k(4\lambda+4\mu-\sigma)}{2\mu+2\lambda+k} \tag{5.17b}$$

In Eqn. 5.16, x_1, x_2, u_1', u_2' and φ_3' are replaced by x, z, u, w, and φ, respectively. The solution of the displacement and rotation fields are assumed to be of the form,

$$u(x,z) = \psi(z)\cos(\eta x) \tag{5.18a}$$

$$w(x,z) = \phi(z)\sin(\eta x) \tag{5.18b}$$

$$\varphi(x,z) = \theta(z)\cos(\eta x) \tag{5.18c}$$

where $\eta = \frac{2\pi}{L}$ (L is the wavelength of the deformation mode). This solution is valid due to the assumption that the deformation mode is periodic in the x_1 direction as stated earlier. Substituting Eqn. 5.18 into Eqn. 5.16, a linear system of ordinary differential equations in terms of the functions $\psi(z), \phi(z)$, and $\theta(z)$ are obtained. Solving them results in,

$$\begin{aligned}\psi(z) = {} & \psi_1\sinh(\eta z) + \psi_2\cosh(\eta z) + \psi_3 z\sinh(\eta z) \\ & + \psi_4 z\cosh(\eta z) + \psi_5\sinh(\eta\tilde{m}z) + \psi_6\cosh(\eta\tilde{m}z)\end{aligned} \tag{5.19a}$$

$$\begin{aligned}\phi(z) = {} & \left(\psi_2 + \frac{\tilde{k}_3}{\eta}\psi_3\right)\sinh(\eta z) + \\ & \left(\psi_1 + \frac{\tilde{k}_3}{\eta}\psi_4\right)\cosh(\eta z) + \psi_4 z\sinh(\eta z) + \\ & \psi_3 z\cosh(\eta z) + \frac{\psi_6}{\tilde{m}}\sinh(\eta\tilde{m}z) + \frac{\psi_5}{\tilde{m}}\cosh(\eta\tilde{m}z)\end{aligned} \tag{5.19b}$$

$$\begin{aligned}\theta(z) = {} & \tilde{k}_1\psi_3\sinh(\eta z) + \tilde{k}_1\psi_4\cosh(\eta z) + \\ & \eta\frac{\tilde{k}_2}{\tilde{m}}\psi_6\sinh(\eta\tilde{m}z) + \eta\frac{\tilde{k}_2}{\tilde{m}}\psi_5\cosh(\eta\tilde{m}z)\end{aligned} \tag{5.19c}$$

In Eqns. 5.19, $\tilde{k}_1, \tilde{k}_2, \tilde{k}_3$, and $\tilde{m}^2$ are nondimensional,

$$\tilde{k}_1 = -\frac{2\tilde{A}_1(2+\tilde{\lambda}+\tilde{k})}{\tilde{A}_1^2+\tilde{A}_2(\tilde{\lambda}+1)} \tag{5.20a}$$

$$\tilde{k}_2 = \frac{\tilde{A}_1^2-(1+\tilde{k})\tilde{A}_2}{\tilde{\gamma}\tilde{A}_1} \tag{5.20b}$$

$$\tilde{k}_3 = \frac{\tilde{A}_1^2-(3+2\tilde{k}+\tilde{\lambda})\tilde{A}_2}{\tilde{A}_1^2+(1+\tilde{\lambda})\tilde{A}_2} \tag{5.20c}$$

$$\tilde{m}^2 = \frac{(1+\tilde{k})(\tilde{A}_2+\tilde{\gamma})-\tilde{A}_1^2}{\tilde{\gamma}(1+\tilde{k})} \tag{5.20d}$$

where

$$\tilde{k} = \frac{k}{\mu} \tag{5.21a}$$

$$\tilde{\lambda} = \frac{\lambda}{\mu} \tag{5.21b}$$

$$\tilde{\gamma} = \frac{\gamma\eta^2}{\mu} \tag{5.21c}$$

$$\tilde{s} = \frac{\sigma}{2\mu} \tag{5.21d}$$

$$\tilde{A}_1 = \tilde{k} + \frac{2\tilde{s}(1+\tilde{\lambda})(2+\tilde{k})}{(2+\tilde{\lambda}+\tilde{k})^2-\tilde{\lambda}^2} \tag{5.21e}$$

$$\tilde{A}_2 = \frac{2\tilde{k}^2+4\tilde{s}(1+\tilde{\lambda})+\tilde{k}(4\tilde{\lambda}+4-2\tilde{s})}{2+2\tilde{\lambda}+\tilde{k}} \tag{5.21f}$$

Eqns. 5.21a,b,c, are the nondimensionalized material properties and Eqn. 5.21d is the nondimensional applied stress. After solving the displacement and rotation fields in Eqn. 5.18, the critical buckling load is determined by applying the boundary conditions, at $z = \pm h$.

$$\Sigma'_{21} = \Sigma'_{22} = M'_{23} = 0 \text{ at } z = \pm h \tag{5.22}$$

where the primes indicate the perturbed stresses ($\Sigma_{21} = \Sigma^0_{21} + \bar{\lambda}\Sigma'_{21}, \Sigma_{22} = \Sigma^0_{22} + \bar{\lambda}\Sigma'_{22}, M_{23} = M^0_{23} + \bar{\lambda}M'_{23}$). Applying the boundary conditions, we obtain a homoge-

neous linear system of 6 equations with 6 unknowns $(\psi_1, \psi_2, \psi_3, \psi_4, \psi_5, \psi_6)$. Taking the determinant of this linear system of equations, the transcendental equation, Δ, is obtained, which is a function of the nondimensional material parameters $\tilde{k}$, $\tilde{\lambda}$, $\tilde{\gamma}$, and the applied load $\tilde{s}$. Setting $\Delta = \Delta(\tilde{k}, \tilde{\lambda}, \tilde{\gamma}, \tilde{s}) = 0$, the critical value of $\tilde{s}$ is determined numerically, and this corresponds to the buckling load.

5.5 1D Micropolar Beam Theory (1DMB)

In classical elasticity, the thickness effects in Fig. 5.1 disappear as the length over height ratio becomes large, in which case, 1D theories such as the Euler-Bernoulli beam theory can be recovered. Similarly, 1D micropolar beam theory (1DMB) is derived using an asymptotic series expansion of the displacement and rotation fields, [85].

$$u(x,z) \simeq u_0(x) + z\chi(x) \tag{5.23a}$$

$$w(x,z) \simeq w(x) \tag{5.23b}$$

$$\varphi_3 \simeq \varphi(x) \tag{5.23c}$$

The corresponding non-zero strains are,

$$\Gamma_{11} = \frac{du_0(x)}{dx} + z\frac{d\chi(x)}{dx} \tag{5.24a}$$

$$\Gamma_{12} = \frac{dw(x)}{dx} - \varphi(x) \tag{5.24b}$$

$$\Gamma_{21} = \chi(x) + \varphi(x) \tag{5.24c}$$

$$K_{13} = \frac{d\varphi(x)}{dx} \tag{5.24d}$$

Assuming $\Sigma_{22} = 0$, the stresses are,

$$\Sigma_{11} = \frac{E_m}{1 - v_m^2} \left(\frac{du_0(x)}{dx} + z \frac{d\chi(x)}{dx} \right) \tag{5.25a}$$

$$\Sigma_{12} = \mu \left(\chi(x) + \frac{dw(x)}{dx} \right) + k \left(\frac{dw(x)}{dx} - \varphi(x) \right) \tag{5.25b}$$

$$\Sigma_{21} = \mu \left(\chi(x) + \frac{dw(x)}{dx} \right) + k \left(\chi(x) + \varphi(x) \right) \tag{5.25c}$$

$$M_{13} = \gamma \frac{d\varphi(x)}{dx} \tag{5.25d}$$

E_m and v_m are the micropolar Young's modulus and Poisson's ratio defined earlier.

The 1DMB equilibrium equations are derived using the variational method. The external work W is determined by assuming the beam to be inextensible or $\Gamma_{11} = 0$. From this assumption, $u(x = a) = \int_0^a \varphi(\frac{\varphi}{2} - \frac{dw}{dx})dx$ (a is the length of the beam) and the external work is,

$$W = \int_0^a P\varphi \left(\frac{dw}{dx} - \frac{\varphi}{2} \right) dx \tag{5.26}$$

P is the external compressive load applied on the beam. Note, in classical elasticity, the local and global rotations are equal, i.e. $\varphi = \frac{dw}{dx}$. This is obtained when considering the micropolar material constants to be zero, as discussed in Appendix D. From this, the external work reduces to $W = \int_0^a P \left(\frac{dw}{dx} \right)^2 dx$, which is the expression for inextensible classical beams under compression. Using the variational method, the equilibrium equations are obtained

$$-\frac{dN}{dx} = 0 \tag{5.27a}$$

$$-\frac{d(\Sigma_{12}A)}{dx} + P\frac{d\varphi(x)}{dx} = 0 \tag{5.27b}$$

$$-\frac{d}{dx} \left(D_m \frac{d\chi(x)}{dx} \right) + \Sigma_{21}A = 0 \tag{5.27c}$$

$$\Sigma_{21}A - \Sigma_{12}A - \frac{d(M_{13}A)}{dx} + P \left(\varphi - \frac{dw}{dx} \right) = 0 \tag{5.27d}$$

$N(x) = \frac{E_m A}{1-v_m^2}\frac{du_0(x)}{dx}$ is the axial force, A is the beam cross sectional area, and $D_m = \frac{E_m I}{1-v_m^2}$ is the rigidity, $I = \frac{1}{12}A(2h)^2$ is the area moment of inertia of a beam with a rectangular cross section. The general boundary conditions for a micropolar beam are,

$$N\delta u_0(x)|_0^a = 0 \tag{5.28a}$$

$$(\Sigma_{12}A - P\varphi)\,\delta w(x)|_0^a = 0 \tag{5.28b}$$

$$\left(D_m\frac{d\chi(x)}{dx}\right)\delta\chi(x)|_0^a = 0 \tag{5.28c}$$

$$(M_{13}A)\delta\varphi(x)|_0^a = 0 \tag{5.28d}$$

Assuming A and D_m are constant along the length of the beam, and the boundary conditions are simply-supported, the equilibrium equations, in terms of displacements are,

$$(\mu+k)\frac{d^2w(x)}{dx^2} + \mu\frac{d\chi(x)}{dx} - \left(k+\frac{P}{A}\right)\frac{d\varphi(x)}{dx} = 0 \tag{5.29a}$$

$$-\frac{D_m}{A}\frac{d^2\chi(x)}{dx^2} + \mu\frac{dw(x)}{dx} + (\mu+k)\chi(x) + k\varphi = 0 \tag{5.29b}$$

$$\gamma\frac{d^2\varphi}{dx^2} - 2\left(k+\frac{P}{A}\right)\varphi + \left(k+\frac{P}{A}\right)\frac{dw}{dx} - k\chi(x) = 0 \tag{5.29c}$$

with boundary conditions,

$$w(0) = w(a) = 0 \tag{5.30a}$$

$$\frac{d\chi(0)}{dx} = \frac{d\chi(a)}{dx} = 0 \tag{5.30b}$$

$$\frac{d\varphi(0)}{dx} = \frac{d\varphi(a)}{dx} = 0 \tag{5.30c}$$

The solution to Eqn. 5.29, results in,

$$w(x) = w \sin\left(\frac{\pi x}{a}\right) \tag{5.31a}$$

$$\chi(x) = \chi \cos\left(\frac{\pi x}{a}\right) \tag{5.31b}$$

$$\varphi(x) = \varphi \sin\left(\frac{\pi x}{a}\right) \tag{5.31c}$$

The coefficients, w, χ, and φ, are constant. The critical load for the beam is determined by substituting Eqns. 5.31 into Eqns. 5.29 to obtain a linear set of equations. Taking the determinant of this, the critical buckling load is obtained as,

$$\begin{aligned}\tilde{s}_{cr}^{1DMB} = \frac{1}{4(1+\tilde{k}+\tilde{D}_m\tilde{h}^2)}\{&\tilde{D}_m\tilde{h}^2(1-\tilde{k}) - \tilde{k}(2+\tilde{k}) \\ &+ \{(\tilde{D}_m\tilde{h}^2(1+\tilde{k}) + \tilde{k}(2+\tilde{k}))(\tilde{k}(2+\tilde{k}) \\ &+ 4\tilde{\gamma}(1+\tilde{D}_m\tilde{h}^2+\tilde{k}) + \tilde{D}_m\tilde{h}^2(1+5\tilde{k}))\}^{1/2}\}\end{aligned} \tag{5.32}$$

where $\tilde{h} = h\eta$, $\tilde{D}_m = \frac{\tilde{E}_m}{3(1-\tilde{\nu}_m^2)}$, $\tilde{E}_m = \frac{(2+\tilde{k})(3\tilde{\lambda}+\tilde{k}+2)}{2\tilde{\lambda}+\tilde{k}+2}$, and $\tilde{\nu}_m = \frac{\tilde{\lambda}}{2\tilde{\lambda}+\tilde{k}+2}$. Taking the micropolar constants $\tilde{\gamma} = \tilde{k} = 0$, $\tilde{s}_{cr}^{1DMB}$ reduces to the Timoshenko critical load $\tilde{s}_{cr}^{1DMB} = \tilde{s}_{cr}^{T}$ (Appendix E).

5.6 Results

5.6.1 Buckling Load

In order to establish the predictions of 2D micropolar theory, the results are compared against the classical elasticity solution for the case of $\tilde{\gamma} = \tilde{k} = 0$ and $\tilde{\lambda} = 2.0$. As stated in Appendix E, by setting $\tilde{\gamma} = \tilde{k} = 0$, the stress and strain tensors become symmetric and the microstructure of the solid is neglected. As a result, the 2D micropolar theory can be compared with classical elasticity. This is shown in Fig. 5.2, where the buckling load is plotted against the ratio of length to thickness of the strip. The

discrepancy between the micropolar solution and the elasticity solution is due to the Von-Karman type assumption made in [4], where linear strains are assumed to be insignificant in comparison with rotations. This assumption has been relaxed in the present derivation of 2D micropolar theory, which provides more accurate results in comparison to [4]. In the limiting case when the thickness of the layer becomes small, the critical loads of the 2D elasticity and 2D micropolar theories converge. In addition, 1D theories such as Euler-Bernoulli and Timoshenko beam theories are recovered when the length to thickness ratio becomes large. The Euler-Bernoulli beam theory is shown to provide an upper bound for the buckling load, while Timoshenko beam theory is seen to approach the 1DMB solution from below.

The effects of the micropolar constants (of the 2D micropolar theory, $\tilde{\gamma}$ and $\tilde{k}$) are analyzed in order to see their effect on the buckling load. For simplicity, the ratio of the Lamé constants is $\tilde{\lambda} = 2.0$ and in Fig. 5.3, the buckling load is plotted against length to thickness ratio of the strip. Fig. 5.3a, the effect of the micropolar constant $\tilde{k}$ is analyzed when $\tilde{\gamma} = 0$. When $\tilde{k} = 0$, the stress and strain tensors become symmetric (Appendix D). It is observed that the buckling load monotonically increases as $\tilde{k}$ is increased. Similarly, in Fig. 5.3b, the effect of the nondimensional characteristic length of the microstructure, $\tilde{\gamma}$, on the critical load is analyzed when taking $\tilde{k} = 0$. It is seen that as $\tilde{\gamma}$ is increased, the critical load is again monotonically increasing. The effect of nonzero $\tilde{k}$ and $\tilde{\gamma}$ is analyzed in Fig. 5.3c. The coupling of these constants in the transcendental equation again gives rise to an increase in the critical load.

The 1DMB critical load in Eqn. 5.32 is validated by comparing it to the 2D micropolar solution in Fig. 5.4. These two theories are compared for different values of the micropolar constants $\tilde{k}$ and $\tilde{\gamma}$ when $\tilde{\lambda} = 2.0$. First, $\tilde{k} = \tilde{\gamma} = 0$ in Fig. 5.4a. In this case, the 2D micropolar solution reduces to the elasticity solution and the 1DMB critical load given in Eqns. 5.29 reduces to the Timoshenko critical load as stated earlier. Next, the micropolar constants $\tilde{k}$ and $\tilde{\gamma}$ are increased. Figure 5.4b shows

the effect of nonzero $\tilde{k}$ when $\tilde{\gamma} = 0$. For large values of $\frac{L}{2\pi h}$, the 1DMB converges to the micropolar solution from below. Similarly, the effect of nonzero $\tilde{\gamma}$ is analyzed when $\tilde{k} = 0$ (Fig. 5.4c). 1DMB solution again converges to the micropolar solution. The effect of nonzero $\tilde{k}$ and $\tilde{\gamma}$ is seen in Fig. 5.4d. Similar to the previous cases, the 1DMB solution again approaches the micropolar solution from below for a large value of length to thickness ratio. As expected, the 1DMB approximation is seen to be valid when the length to thickness ratio is large.

5.6.2 Buckling Modes

The global buckling modes of a micropolar material are also analyzed. In this section, the modes will be shown for the cases when the length to thickness ratio is small ($\frac{L}{2\pi h} = 0.6$) and large ($\frac{L}{2\pi h} = 6.0$). The effect of the micropolar constants on the buckling modes will be considered by first analyzing the mode shapes when $\tilde{k} = \tilde{\gamma} = 0$ in Fig. 5.5 and when $\tilde{k}, \tilde{\gamma}$ are nonzero in Fig. 5.6. In Fig. 5.5a,b, the transverse deflection of the solid is first analyzed when $\tilde{k} = \tilde{\gamma} = 0$. The terminal position, or the buckled state, is shown with solid lines and the initial (prebuckled) state is in dashed lines. As seen, the deformation mode of $w(x, z)$ is symmetric for when ($\frac{L}{2\pi h} = 0.6$) and ($\frac{L}{2\pi h} = 6.0$). Next, the mode of $u(x, z)$ is shown in Fig. 5.5c,d. Because this function is harmonic in the x-direction, as seen in Eqn. 5.18a, the function $\psi(z)$ will be plotted across the z-axes. When $\frac{L}{2\pi h} = 0.6$, $\psi(z)$ varies nonlinearly across the thickness of the solid. This is induced by the shear effects which are present when the thickness becomes comparable with the wavelength of the structure. As the slenderness is increased ($\frac{L}{2\pi h} = 6.0$), these effects become negligible and the displacement u becomes linear across the cross section of the solid. Because of this, Kirchhoff's hypothesis becomes valid and Euler-Bernoulli beam theory can be applied. The variation of the rotation across the thickness of the solid is shown in a similar fashion (Fig. 5.5e,f). Because the value of $\tilde{k} = 0$ in this case, this local rotation becomes the global rotation

(macrorotation) of the solid's cross section (Appendix D). The magnitude of this is minimum at the center and it is maximum at the top and the bottom surfaces. For $\frac{L}{2\pi h} = 0.6$, the difference between the center of the solid and the surfaces is much larger than for $\frac{L}{2\pi h} = 6.0$. As the value of $\frac{L}{2\pi h}$ increases (or thickness of the solid decreases), the φ becomes constant across the z-direction.

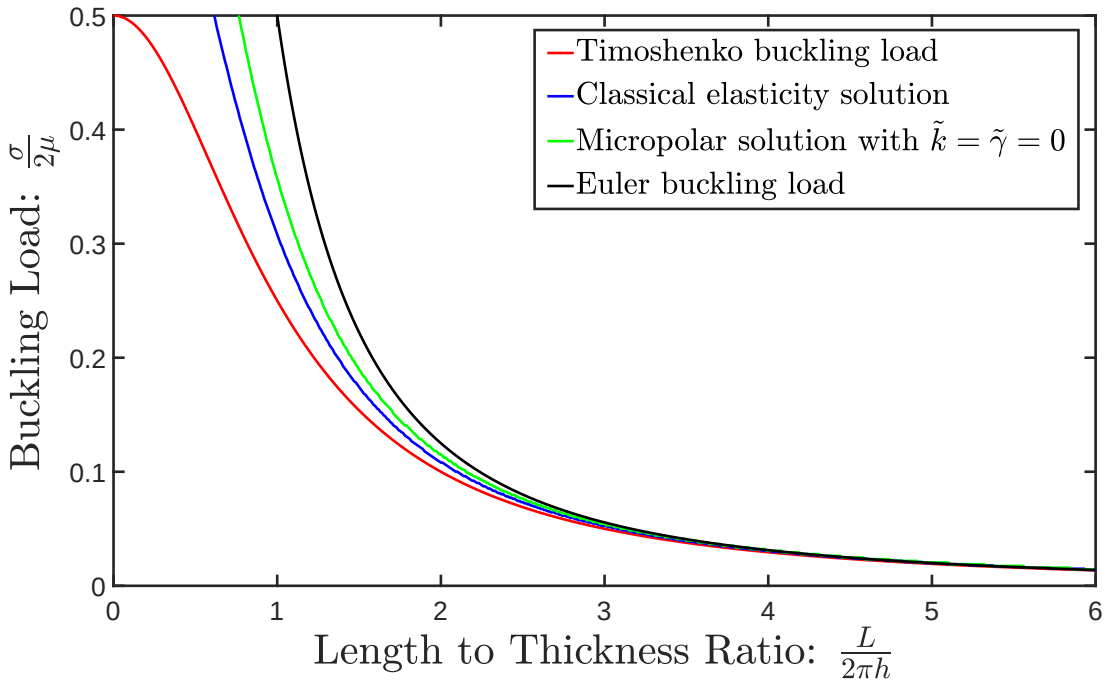

Figure 5.2: Comparison between Timoshenko theory (red), elasticity solution according to [4] (blue), micropolar theory (green), Euler-Bernoulli beam theory (black) when $\tilde{k} = \tilde{\gamma} = 0$ and $\tilde{\lambda} = 2.0$.

The deformation modes in Fig. 5.6 show the effect of micropolarity when $\tilde{k} = 0.4$ and $\tilde{\gamma} = 0.2$. In Fig. 5.6a,b, the mode shape of the transverse deflection is again symmetric for both $\frac{L}{2\pi h} = 0.6$ and $\frac{L}{2\pi h} = 6.0$. In Fig. 5.6c, the variation of u across the thickness of the solid is "more" linear than in Fig. 5.5c. This is because of the interaction of the shear and couple-stresses. Unlike in classical elasticity, the local rotations across the z-axes induce u to vary "more" linearly across the thickness. Increasing the slenderness of the solid ($\frac{L}{2\pi h} = 6.0$), u becomes "more" linear. The mode shape of the rotation across the z-axes is shown in Fig. 5.6e,f. Unlike classical

elasticity, this rotational field represents the local rotation (microrotation) of the solid. It is seen that the local rotation is minimum at the center and approaches a maximum value at the top and bottom surfaces of the solid. When the slenderness increases, the variation of the local rotation across the z-direction becomes negligible, as seen in Fig. 5.6f. This has been tacitly assumed in 1DMB for slender beams in Eqn. 5.31c.

5.7 Conclusions

The effect of a material's microstructure on the buckling of a solid material was captured using micropolar theory. In doing so, the nonlinear micropolar buckling equations were derived. In order to verify the results, the micropolar buckling solution was compared with the elasticity solution by setting the micropolar constants $\tilde{k} = \tilde{\gamma} = 0$. By increasing the micropolar constants $\tilde{k}$ and $\tilde{\gamma}$, the buckling load was shown to increase. For slender solids, the 1D micropolar beam theory (1DMB) was developed and this theory was shown to be in good agreement with the micropolar exact solution in the limit, $\frac{L}{2\pi h} \to \infty$. In addition, the buckling modes were analyzed. The micropolar constants, $\tilde{k}$ and $\tilde{\gamma}$ were seen to have no effect on the transverse deflection, $w(x, z)$, which displayed a symmetric mode at the critical load. The local rotation distribution across the thickness of the solid, corresponding to the buckling load, was also analyzed. As seen, the local rotation was a minimum at the center of the solid and had a maximum value at the top and bottom surfaces. As the thickness of the solid decreases, it was shown that the local rotation has little variation across the cross section (independent of z-coordinate).

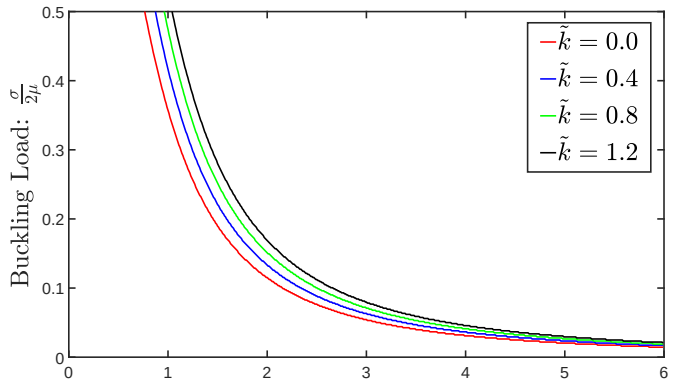

(a) $\tilde{k} \neq 0$, $\tilde{\gamma} = 0$, and $\tilde{\lambda} = 2.0$

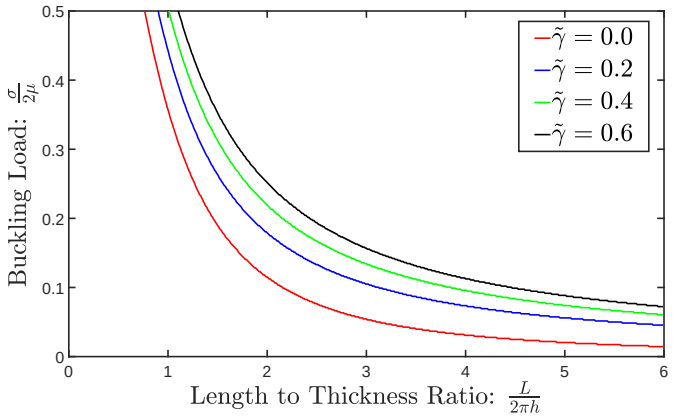

(b) $\tilde{k} = 0$, $\tilde{\gamma} \neq 0$, and $\tilde{\lambda} = 2.0$

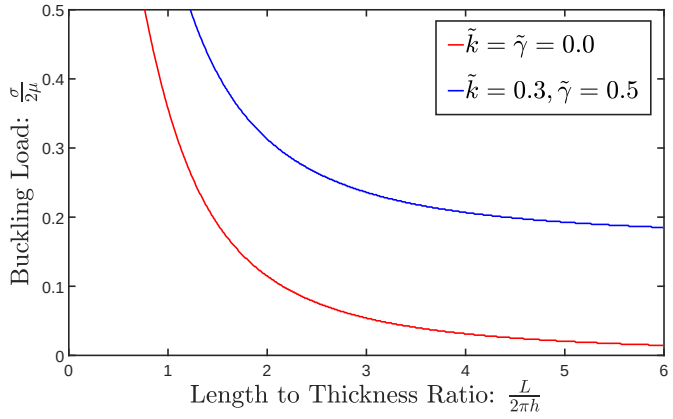

(c) $\tilde{k} \neq 0$, $\tilde{\gamma} \neq 0$, and $\tilde{\lambda} = 2.0$

Figure 5.3: The effect of the micropolar constant (a) $\tilde{k}$, (b) $\tilde{\gamma}$, and (c) their coupling effect on the buckling load $\tilde{s} = \frac{\sigma}{2\mu}$.

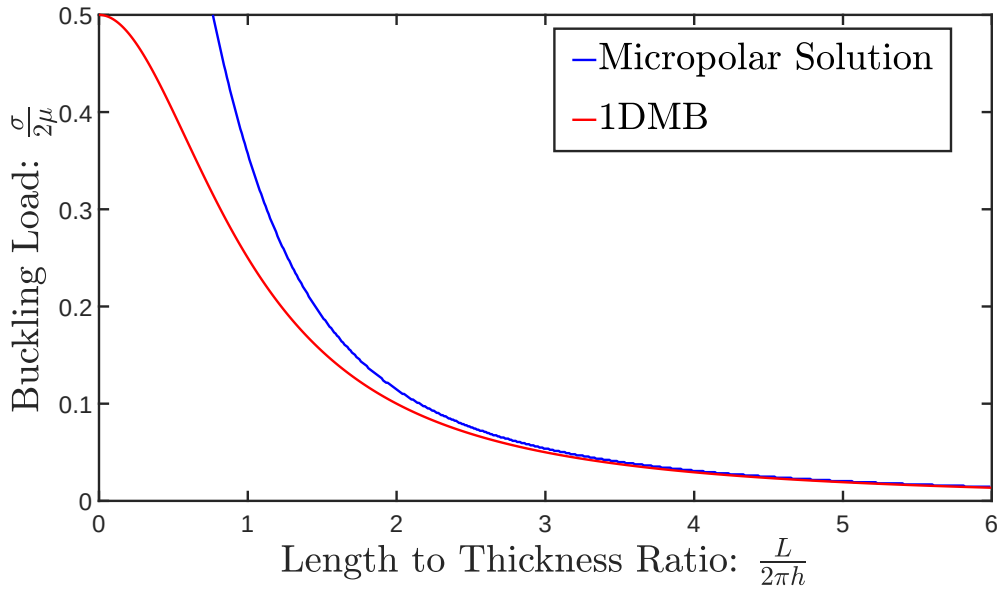

(a) $\tilde{\gamma} = 0, \tilde{k} = 0$

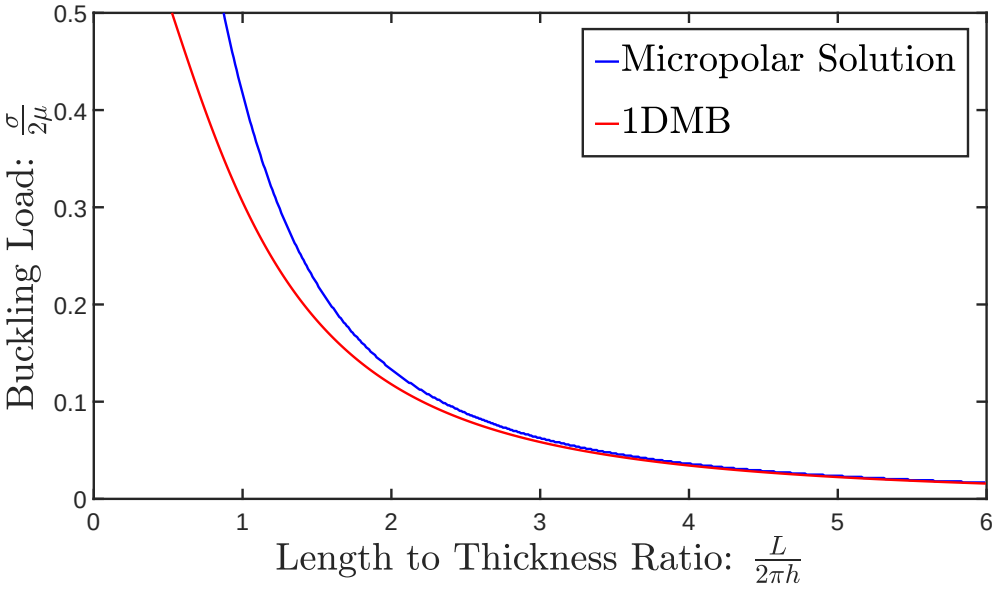

(b) $\tilde{\gamma} = 0, \tilde{k} = 0.4$

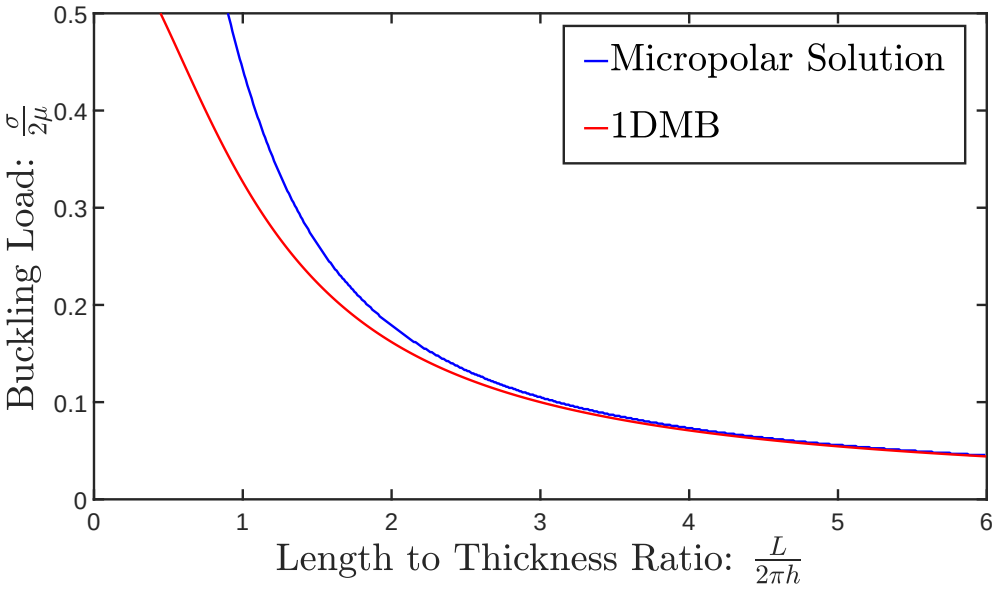

(c) $\tilde{\gamma} = 0.2, \tilde{k} = 0$

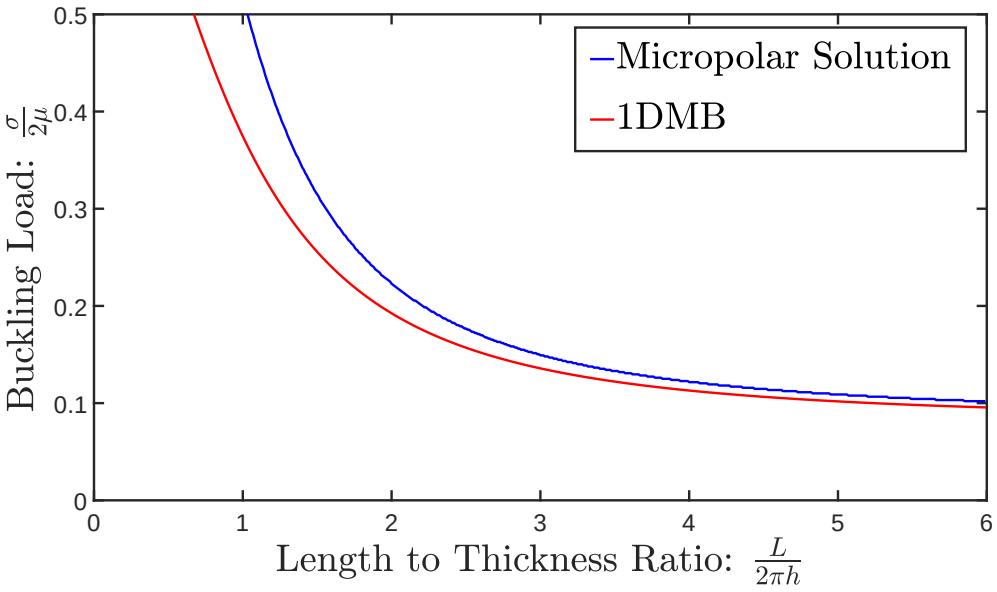

(d) $\tilde{\gamma} = 0.2, \tilde{k} = 0.4$

Figure 5.4: Comparison of 1DMB theory (red) with the micropolar solution (blue).

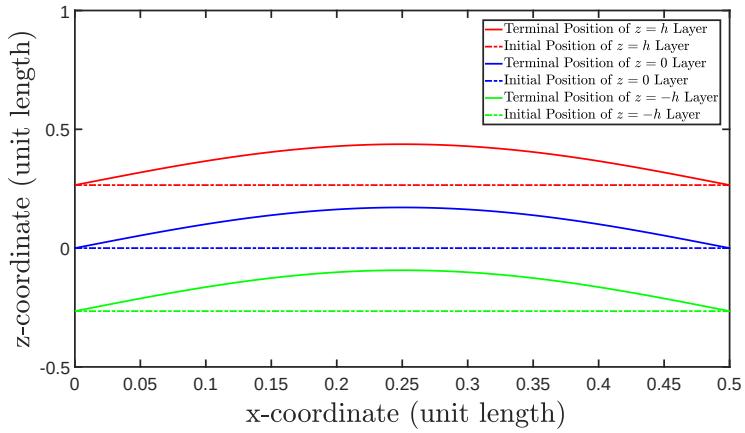

(a) $\frac{L}{2\pi h} = 0.6$

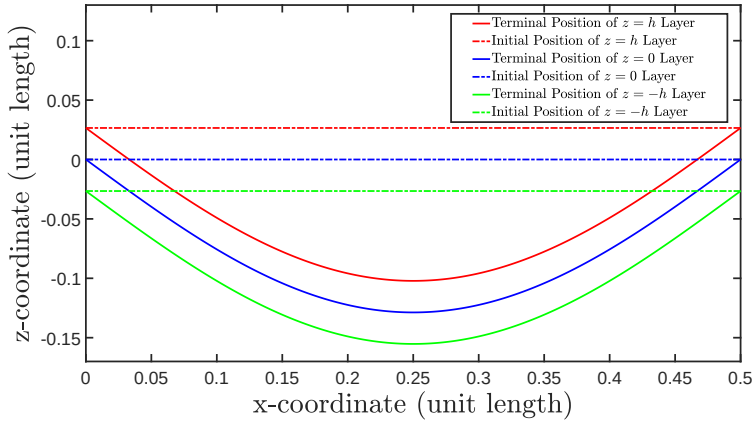

(b) $\frac{L}{2\pi h} = 6.0$

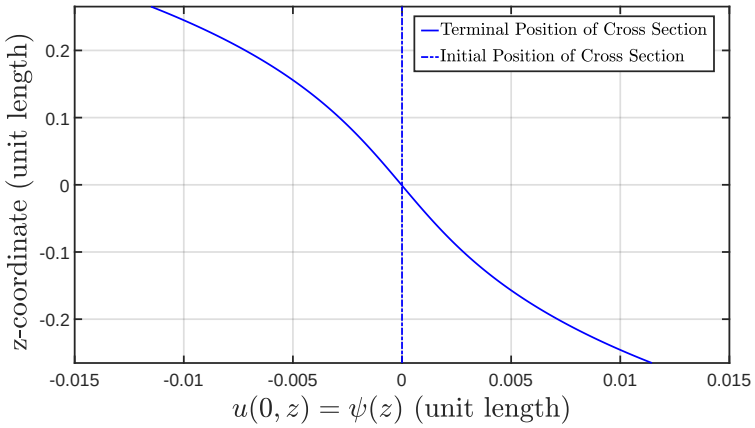

(c) $\frac{L}{2\pi h} = 0.6$

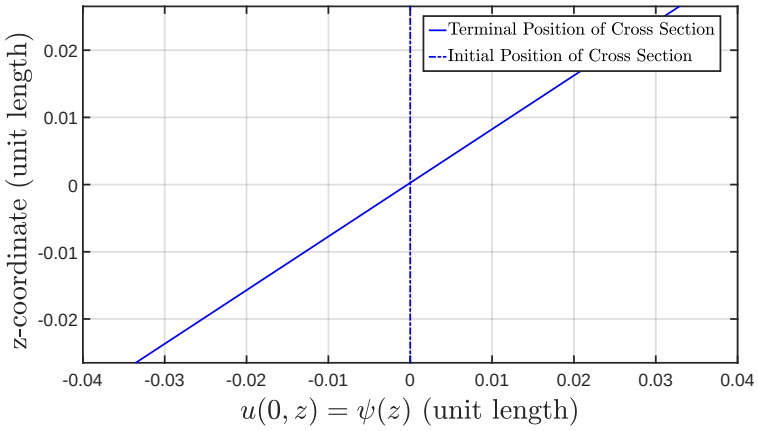

(d) $\frac{L}{2\pi h} = 6.0$

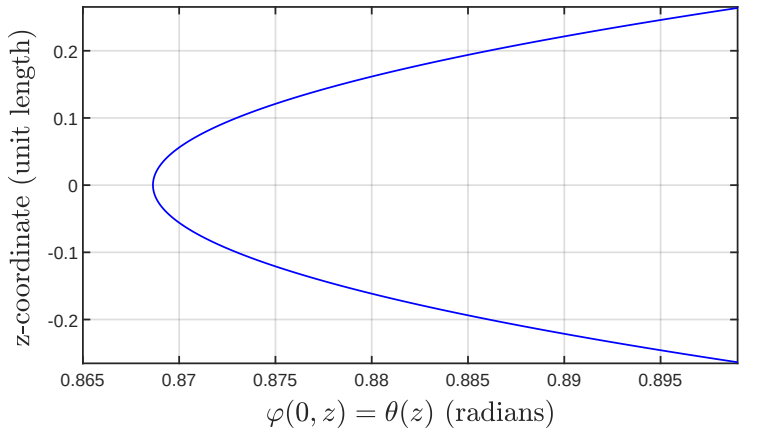

(e) $\frac{L}{2\pi h} = 0.6$

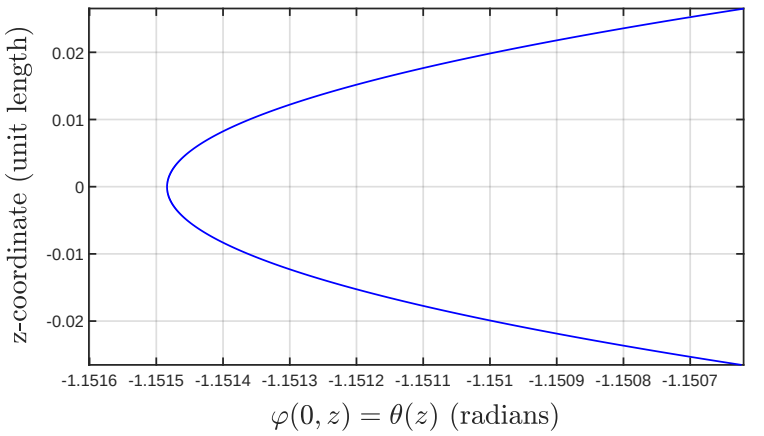

(f) $\frac{L}{2\pi h} = 6.0$

Figure 5.5: Deformation modes for an elastic solid ($\tilde{k} = \tilde{\gamma} = 0$) for low and high values of $\frac{L}{2\pi h}$.

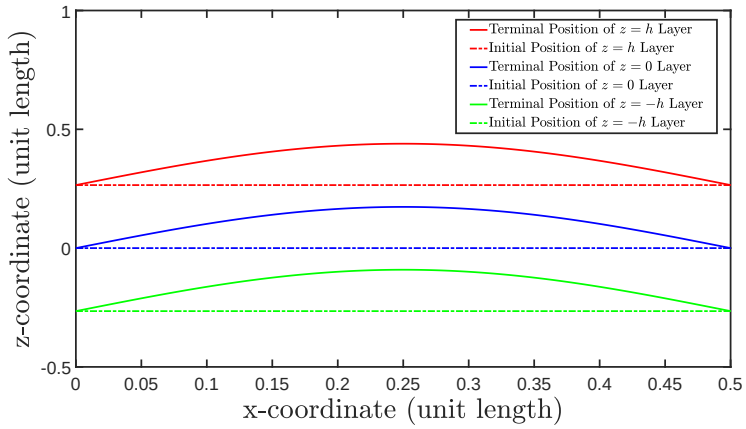

(a) $\frac{L}{2\pi h} = 0.6$

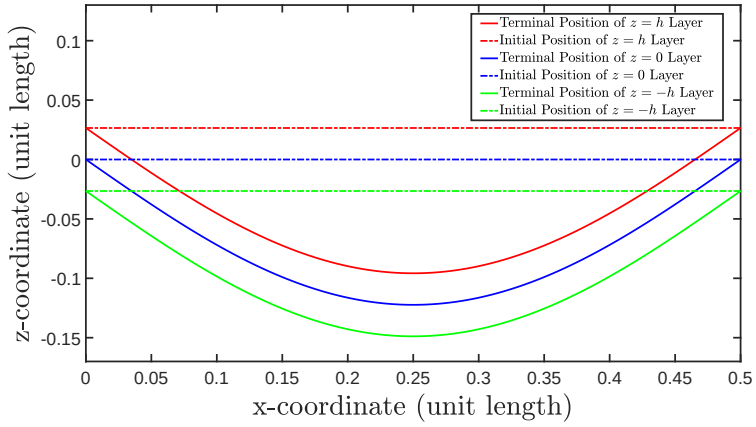

(b) $\frac{L}{2\pi h} = 6.0$

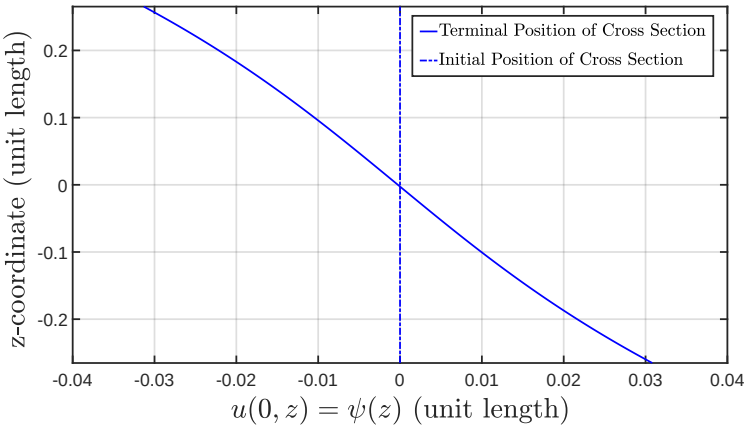

(c) $\frac{L}{2\pi h} = 0.6$

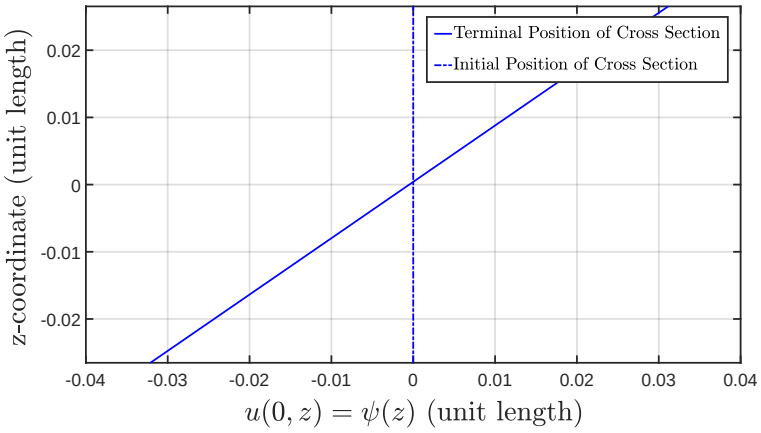

(d) $\frac{L}{2\pi h} = 6.0$

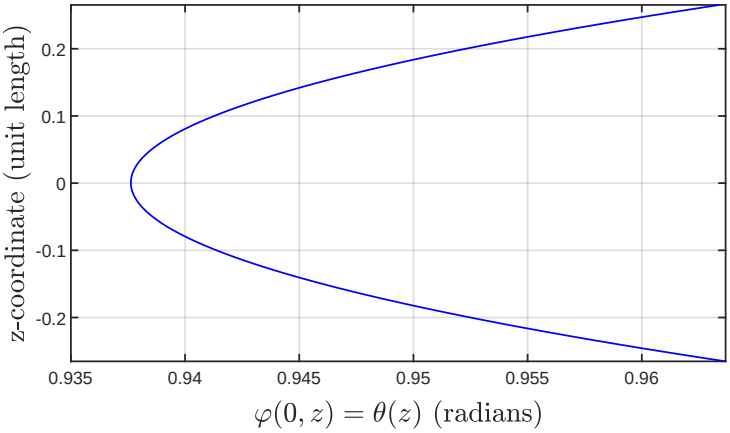

(e) $\frac{L}{2\pi h} = 0.6$

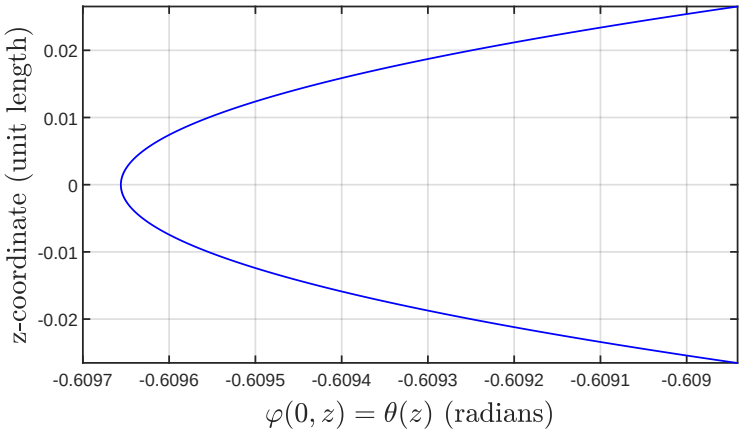

(f) $\frac{L}{2\pi h} = 6.0$

Figure 5.6: Deformation modes for a micropolar solid ($\tilde{k} = 0.4, \tilde{\gamma} = 0.2$) for low and high values of $\frac{L}{2\pi h}$.

CHAPTER 6

Concluding Remarks and Future Work

In this dissertation, geometrically and materially nonlinear micropolar theory was developed. In Chapter 2, the continuum model, with local rotational degrees of freedom and internal couple-stresses was applied to analyze fiber reinforced composites. In this high fidelity model, the effects of the local fiber rotation/moments were incorporated in the continuum formulation. Following this, an updated Lagrangian nonlinear finite element method was applied for numerical analysis. It was done using a fortran based user element (UEL) subroutine with the commercial software ABAQUS. The utility of the higher order micropolar theory and the introduction of the length scale parameters was demonstrated in understanding localization phenomenon observed in fiber reinforced composites. Unlike previous studies in this area, it was shown that localization can be induced as a structural instability of the homogeneous micropolar continuum, instead of a material instability with a softening relation in the constitutive model, which is in violation of the Drucker stability criterion. In addition, the localization width was shown to be a function of the micropolar length scale parameter, while the localization angle is influenced by the additional micropolar shear modulus. In this study, only 2D analysis was done for simplicity. In the future, the corresponding 3D nonlinear finite element formulation will be beneficial for predicting localization in 3D structures, such as fiber tows in textile composites.

In Chapter 3, physics based numerical tests were proposed for predicting the

additional material constants of 2D fiber reinforced composites. Similar tests can be done on 3D structures, which incorporate the twisting deformation modes of the fibers. This mode of deformation introduces an additional length scale parameter associated with the torsion of the fibers. Its effects on the localization width and angle was not considered in the 2D analysis, but should be studied for 3D fiber tows.

In Chapter 4, volume averaging methods were used to determine the micropolar properties of cellular solids. Using nondimensional analysis, closed form expressions were obtained for the material constants. Similar to fiber kinking in fiber reinforced solids, when under compression, weak discontinuities (continuous macroscopic displacement, discontinuous gradients) have also been observed in polymeric cellular medium. One challenge has been the prediction of localization in these class of materials at the continuum scale. In the future, similar micropolar models will be considered for cellular solids.

With respect to the homogenization method in Chapter 4, one of the current challenges pertains to extending similar micromechanics methods to determining the effective micropolar properties of multi-phase Cauchy medium. The difficulty is presently in enforcing local rotation on the boundary of a heterogenous microstructure, which is discussed in Appendix F. Currently, more research is needed in developing micromechanics methods for this purpose.

In the nonlinear micropolar model considered in Chapter 2, the symmetric component of the strain tensor was assumed to be nonlinear, however, its skew-symmetric and curvature strains were assumed to be linear. In Chapter 5, the general finite micropolar theory was discussed. The strain energy was assumed to be a function of an asymmetric strain and curvature strains, from which classical results are irreducible. In the future, correct (admissible) strain measures are necessary which meet this requirement. As a result, a possible area of research is in defining asymmetric strain measures, from which Green-Lagrange strain is obtained in the absence of the

micropolar constants in the constitutive relation.

APPENDIX A

2D Micropolar Elastoplastic Stiffness Matrix

In this appendix, the 2D elastoplastic stiffness introduced in Eqn. 2.48 is derived. Considering the micropolar Hill's yield surface, the gradients of the plastic potential are

$$\hat{n}^{\Sigma}_{11} = \frac{1}{\sigma_e}\left(\overline{G}(\hat{S}_{11} - \hat{S}_{33}) + \overline{H}(\hat{S}_{11} - \hat{S}_{22})\right) \tag{A.1a}$$

$$\hat{n}^{\Sigma}_{22} = \frac{1}{\sigma_e}\left(\overline{F}(\hat{S}_{22} - \hat{S}_{33}) + \overline{H}(\hat{S}_{22} - \hat{S}_{11})\right) \tag{A.1b}$$

$$\hat{n}^{\Sigma}_{33} = \frac{1}{\sigma_e}\left(\overline{F}(\hat{S}_{33} - \hat{S}_{22}) + \overline{G}(\hat{S}_{33} - \hat{S}_{11})\right) \tag{A.1c}$$

$$\hat{n}^{\Sigma}_{12} = \hat{n}^{\Sigma}_{21} = \frac{1}{\sigma_e}\overline{N}\hat{S}_{12} \tag{A.1d}$$

$$\hat{n}^{M}_{13} = \frac{1}{\sigma_e}\overline{Y}\hat{M}_{13} \tag{A.1e}$$

$$\hat{n}^{M}_{23} = \frac{1}{\sigma_e}\overline{Z}\hat{M}_{23} \tag{A.1f}$$

The corresponding values of $\hat{\boldsymbol{H}}^{\Sigma}$ and $\hat{\boldsymbol{H}}^{M}$ are

$$\hat{H}^{\Sigma}_{11} = \hat{C}_{11}\hat{n}^{\Sigma}_{11} + \hat{C}_{12}\hat{n}^{\Sigma}_{22} + \hat{C}_{12}\hat{n}^{\Sigma}_{33} \tag{A.2a}$$

$$\hat{H}^{\Sigma}_{22} = \hat{C}_{12}\hat{n}^{\Sigma}_{11} + \hat{C}_{22}\hat{n}^{\Sigma}_{22} + \hat{C}_{v}\hat{n}^{\Sigma}_{33} \tag{A.2b}$$

$$\hat{H}^{\Sigma}_{33} = \hat{C}_{12}\hat{n}^{\Sigma}_{11} + \hat{C}_{v}\hat{n}^{\Sigma}_{22} + \hat{C}_{22}\hat{n}^{\Sigma}_{33} \tag{A.2c}$$

$$\hat{H}_{12}^{\Sigma} = 2\left(\hat{C}_{33} + \hat{C}_{34}\right)\hat{n}_{12}^{\Sigma} \tag{A.2d}$$

$$\hat{H}_{21}^{\Sigma} = 2\left(\hat{C}_{33} - \hat{C}_{34}\right)\hat{n}_{12}^{\Sigma} \tag{A.2e}$$

$$\hat{H}_{13}^{M} = \hat{C}_{55}\hat{n}_{13}^{M} \tag{A.2f}$$

$$\hat{H}_{23}^{M} = \hat{C}_{66}\hat{n}_{23}^{M} \tag{A.2g}$$

Next, by defining the vector $\{\hat{\boldsymbol{H}}\}$

$$\{\hat{\boldsymbol{H}}\}^T = \{\hat{H}_{11}^{\Sigma} \quad \hat{H}_{22}^{\Sigma} \quad \frac{\hat{H}_{12}^{\Sigma} + \hat{H}_{21}^{\Sigma}}{2} \quad \frac{\hat{H}_{12}^{\Sigma} - \hat{H}_{21}^{\Sigma}}{2} \quad \hat{H}_{13}^{M} \quad \hat{H}_{23}^{M}\} \tag{A.3}$$

the plastic multiplier is

$$\dot{\lambda} = \frac{\{\hat{\boldsymbol{H}}\}^T\{\dot{\hat{\boldsymbol{\gamma}}}\}}{h} \tag{A.4}$$

where the numerator corresponds to the loading/unloading condition defined in Eqn. 2.43 and the denominator is

$$h = E_p + \hat{H}_{11}^{\Sigma}\hat{n}_{11}^{\Sigma} + \hat{H}_{22}^{\Sigma}\hat{n}_{22}^{\Sigma} + \hat{H}_{33}^{\Sigma}\hat{n}_{33}^{\Sigma} + (\hat{H}_{12}^{\Sigma} + \hat{H}_{21}^{\Sigma})\hat{n}_{12}^{\Sigma} + \hat{H}_{13}^{M}\hat{n}_{13}^{M} + \hat{H}_{23}^{M}\hat{n}_{23}^{M} > 0 \tag{A.5}$$

The elastoplastic constitutive relation defined in Eqn. 2.48 results in

$$\{\dot{\hat{\boldsymbol{\sigma}}}\} = [\hat{\boldsymbol{C}}^{ep}]\{\dot{\hat{\boldsymbol{\gamma}}}\} = \left([\hat{\boldsymbol{C}}^{e}] - \frac{1}{h}\{\hat{\boldsymbol{H}}\}\{\hat{\boldsymbol{H}}\}^T\right)\{\dot{\hat{\boldsymbol{\gamma}}}\} \tag{A.6}$$

where the arrangements of the vectors $\{\dot{\hat{\boldsymbol{\sigma}}}\}$ and $\{\dot{\hat{\boldsymbol{\gamma}}}\}$ are given in Eqn. 2.49 and the elastic stiffness $[\hat{\boldsymbol{C}}^{e}]$ was defined in Eqn. 2.26. Also, the out-of-plane nonzero stress

rate is

$$\dot{\hat{S}}_{33} = \left(\hat{C}^e_{12} - \frac{\hat{H}^\Sigma_{33}\hat{H}^\Sigma_{11}}{h}\right)\dot{\hat{e}}_{11} + \left(\hat{C}^e_v - \frac{\hat{H}^\Sigma_{33}\hat{H}^\Sigma_{22}}{h}\right)\dot{\hat{e}}_{22} + \left(-\frac{\hat{H}^\Sigma_{33}(\hat{H}^\Sigma_{12} + \hat{H}^\Sigma_{21})}{2h}\right)(2\dot{\hat{e}}_{12}) + \left(-\frac{\hat{H}^\Sigma_{33}(\hat{H}^\Sigma_{12} - \hat{H}^\Sigma_{21})}{2h}\right)(2\dot{\hat{A}}_{12}) + \left(-\frac{\hat{H}^\Sigma_{33}\hat{H}^\Sigma_{13}}{h}\right)\dot{\hat{K}}_{13} + \left(-\frac{\hat{H}^\Sigma_{33}\hat{H}^\Sigma_{23}}{h}\right)\dot{\hat{K}}_{23} \tag{A.7}$$

APPENDIX B

Nonlinear Micropolar Finite Element Matrices

In the finite element algebraic equations presented in Eqn. 2.88, the matrices are defined for a 4-noded quadrilateral element (Fig. 2.4). The stiffness matrices and the nodal residual force vector are

$$[\,{}^{n}_{n}\boldsymbol{K}_{L}] = \int_{{}^{n}V} [\,{}^{n}_{n}\boldsymbol{B}_{L}]^{T} \left([\,{}_{n}\boldsymbol{C}^{ep}] + [\,{}_{n}\boldsymbol{C}^{\sigma}]\right) [\,{}^{n}_{n}\boldsymbol{B}_{L}] d\,{}^{n}V \tag{B.1a}$$

$$[\,{}^{n}_{n}\boldsymbol{K}_{NL}] = \int_{{}^{n}V} [\,{}^{n}_{n}\boldsymbol{B}_{NL}]^{T} [\,{}^{n}\boldsymbol{\tau}] [\,{}^{n}_{n}\boldsymbol{B}_{NL}] d\,{}^{n}V \tag{B.1b}$$

$$\{\,{}^{n}_{n}\boldsymbol{F}\} = \int_{{}^{n}V} [\,{}^{n}_{n}\boldsymbol{B}_{L}]^{T} \{\,{}^{n}\tilde{\boldsymbol{\tau}}\} d\,{}^{n}V \tag{B.1c}$$

Based on the arrangement of the nodal displacements and rotations according to Eqn. 2.87, the B-matrices above are defined in terms of the shape functions

$$[\,{}^{n}_{n}\boldsymbol{B}_{L}] = \begin{bmatrix} {}_{n}N_{1,1} & 0 & 0 & & {}_{n}N_{4,1} & 0 & 0 \\ 0 & {}_{n}N_{1,2} & 0 & & 0 & {}_{n}N_{4,2} & 0 \\ {}_{n}N_{1,2} & {}_{n}N_{1,1} & 0 & & {}_{n}N_{4,2} & {}_{n}N_{4,1} & 0 \\ -\,{}_{n}N_{1,2} & {}_{n}N_{1,1} & -\,2\,{}_{n}N_{1} & \cdots & -\,{}_{n}N_{4,2} & {}_{n}N_{4,1} & -\,2\,{}_{n}N_{4} \\ 0 & 0 & {}_{n}N_{1,1} & & 0 & 0 & {}_{n}N_{4,1} \\ 0 & 0 & {}_{n}N_{1,2} & & 0 & 0 & {}_{n}N_{4,2} \end{bmatrix} \tag{B.2}$$

$$[\,{}^{n}_{n}\boldsymbol{B}_{NL}] = \begin{bmatrix} {}_{n}N_{1,1} & 0 & 0 & & {}_{n}N_{4,1} & 0 & 0 \\ {}_{n}N_{1,2} & 0 & 0 & \dots & {}_{n}N_{4,2} & 0 & 0 \\ 0 & {}_{n}N_{1,1} & 0 & & 0 & {}_{n}N_{4,1} & 0 \\ 0 & {}_{n}N_{1,2} & 0 & & 0 & {}_{n}N_{4,2} & 0 \end{bmatrix} \tag{B.3}$$

Also, the residual Cauchy stresses and couple-stresses, are arranged in $[\,{}^{n}\boldsymbol{\tau}]$ and $\{\,{}^{n}\tilde{\boldsymbol{\tau}}\}$ as

$$[\,{}^{n}\boldsymbol{\tau}] = \begin{bmatrix} {}^{n}S_{11} & {}^{n}S_{12} & 0 & 0 \\ {}^{n}S_{12} & {}^{n}S_{22} & 0 & 0 \\ 0 & 0 & {}^{n}S_{11} & {}^{n}S_{12} \\ 0 & 0 & {}^{n}S_{12} & {}^{n}S_{22} \end{bmatrix} \tag{B.4}$$

$$\{\,{}^{n}\tilde{\boldsymbol{\tau}}\} = \begin{Bmatrix} {}^{n}S_{11} & {}^{n}S_{22} & {}^{n}S_{12} & {}^{n}T_{12} & {}^{n}M_{13} & {}^{n}M_{23} \end{Bmatrix}^{T} \tag{B.5}$$

APPENDIX C

Concentric Cylinder Model (CCM)

In obtaining the effective elastic properties, relating the symmetric stresses to the symmetric strains, the concentric cylinder model (CCM) is considered. The composite material is represented by 2 layered concentric cylinders, as seen in Fig. C.1. The radius of the inner and the outer cylinders, r_a and r_b, respectively, are chosen such that the volume fraction of the concentric cylinders are the same as the composite under consideration ($V^f = \frac{r_a^2}{r_b^2}$). The elastic properties are obtained by solving a set of boundary value problems and relating the external loads to the deformation of the concentric cylinders. The effective transversely-isotropic composite properties in terms of the transversely-isotropic fiber, isotropic matrix, and a specified fiber volume fraction V^f are

$$\hat{E}_{11} = \hat{E}_{11}^f(1+\gamma)V^f + E^m(1+\delta)(1-V^f) \tag{C.1a}$$

$$\hat{E}_{22} = \hat{E}_{33} = \left(\frac{\eta^f V^f}{\hat{E}_{22}^f} + \frac{\eta^m(1-V^f)}{E^m}\right)^{-1} \tag{C.1b}$$

$$\hat{v}_{12} = \frac{(1-V^f)(1-\hat{v}_{23}^f - 2\hat{v}_{12}^f\hat{v}_{21}^f)v^m E^m}{E^m(1-V^f)(1-\hat{v}_{23}^f - 2\hat{v}_{12}^f\hat{v}_{21}^f) + \hat{E}_{22}^f(1+V^f+(1-V^f)v^m - 2V^f(v^m)^2)} + \tag{C.1c}$$

$$\frac{\left(v^m + V^f(2\hat{v}_{12}^f - v^m) + (v^m)^2(1-2V^f\hat{v}_{12}^f - V^f)\right)\hat{E}_{22}^f}{E^m(1-V^f)(1-\hat{v}_{23}^f - 2\hat{v}_{12}^f\hat{v}_{21}^f) + \hat{E}_{22}^f(1+V^f+(1-V^f)v^m - 2V^f(v^m)^2)}$$

$$\hat{G}_{12} = \hat{G}_{13} = G^m\left(\frac{(G^m + \hat{G}_{12}^f) - V^f(G^m - \hat{G}_{12}^f)}{(G^m + \hat{G}_{12}^f) + V^f(G^m - \hat{G}_{12}^f)}\right) \tag{C.1d}$$

$$\hat{G}_{23} = \frac{V^f + \eta_4(1 - V^f)}{(V^f/\hat{G}^f_{23}) + \eta_4(1 - V^f)/G^m} \tag{C.1e}$$

where

$$\gamma = \frac{2\hat{v}^f_{21}E^m(1 - \hat{v}^f_{23} - 2\hat{v}^f_{12}\hat{v}^f_{21})(\hat{v}^f_{12} - v^m)V^f}{\hat{E}^f_{22}(1 + v^m)(1 + V^f(1 - 2v^m)) + E^m(1 - \hat{v}^f_{23} - 2\hat{v}^f_{12}\hat{v}^f_{21})(1 - V^f)} \tag{C.2a}$$

$$\delta = \frac{2\hat{E}^f_{22}v^m V^f(v^m - \hat{v}^f_{12})}{\hat{E}^f_{22}(1 + v^m)(1 + V^f(1 - 2v^m)) + E^m(1 - \hat{v}^f_{23} - 2\hat{v}^f_{12}\hat{v}^f_{21})(1 - V^f)} \tag{C.2b}$$

$$\eta^f = \frac{\hat{E}^f_{11}V^f + ((1 - \hat{v}^f_{12}\hat{v}^f_{21})E^m + v^m\hat{v}^f_{21}\hat{E}^f_{11})(1 - V^f)}{\hat{E}^f_{11}V^f + E^m(1 - V^f)} \tag{C.2c}$$

$$\eta^m = \frac{((1 - (v^m)^2)\hat{E}^f_{11} - (1 - v^m\hat{v}^f_{12})E^m)V^f + E^m(1 - V^f)}{\hat{E}^f_{11}V^f + E^m(1 - V^f)} \tag{C.2d}$$

$$\eta_4 = \frac{3 - 4v^m + G^m/\hat{G}^f_{23}}{4(1 - v^m)} \tag{C.2e}$$

$$\hat{v}^f_{21} = \hat{v}^f_{12}\frac{\hat{E}^f_{22}}{\hat{E}^f_{11}} \tag{C.2f}$$

The fiber properties are indicated by the superscript f and the isotropic matrix properties by m. E, G, v are the Youngs modulus, shear modulus, and Poisson's ratio, respectively. The transversely-isotropic fiber properties, indicated by $\hat{(\,)}$ in order to highlight the anisotropy of the fibers, are specified in a fiber-aligned coordinate system $\hat{x}_i$.

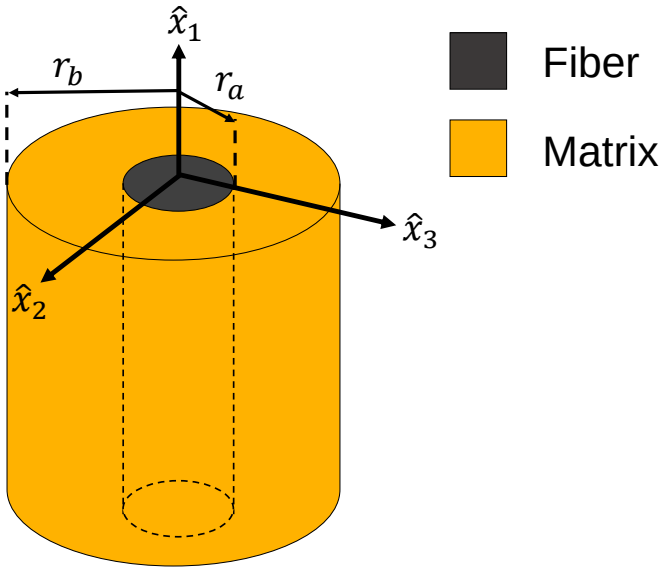

Figure C.1: Concentric cylinder representation of a fiber reinforced composite.

APPENDIX D

Material Constants

Because of the principle of nonnegative internal energy in Eqn. 5.13, the micropolar constants k and γ will be assumed to be positive. In Eqn. 5.21, the nondimensional micropolar constants, $\tilde{k} = \frac{k}{\mu}$ and $\tilde{\gamma} = \frac{\gamma\eta^2}{\mu}$, will also be taken to be positive by assuming $\mu > 0$. By setting these constants to zero, the classical elasticity results will be recovered. The equilibrium, strain-displacement, and the constitutive equations will reduce to the classical elasticity equations and the two constants, λ and μ, will correspond to the two Lamé constants for an isotropic, elastic solid. In this case, the nondimensional constant $\tilde{\lambda}$ in Eqn. 5.21b will depend on the Poisson's ratio (v).

$$\tilde{\lambda} = \frac{\lambda}{\mu} = \frac{\frac{Ev}{(1+v)(1-2v)}}{\frac{E}{2(1+v)}} = \frac{2v}{1-2v} \tag{D.1}$$

For the numerical simulations in the results section, the Poisson's ratio v will be taken to be $v = \frac{1}{3}$, which is common for most engineering materials. For simplicity, this value will also be used for cases when $\tilde{k}$ and $\tilde{\gamma}$ are nonzero.

The physical meaning of the parameter $\tilde{\gamma}$ is related to the characteristic length of the microstructure. The dimension of $\frac{\gamma}{\mu}$ is length squared, which represents the microstructure's characteristic length. Multiplying the characteristic length squared by η^2 results in the ratio of the microstructure characteristic length squared and the global length of the structure squared multiplied by $(2\pi)^2$ constant ($\tilde{\gamma} = \frac{(2\pi)^2\gamma}{\mu L^2}$). In applications, $\tilde{\gamma} \ll 1$, but in our analysis, we will assume that it can approach to values

as large as 0.6.

The material constant $\tilde{k}$ represents the asymmetry of stresses and strains of the material. Looking at the constitutive relations, Eqn. 5.12c,d, when $k = 0$, $T_{12} = T_{21}$. From this, it can be shown that $\Gamma_{12} = \Gamma_{21}$. It can also be proven that the local rotation is equal to the global rotation ($\varphi_3 = \frac{1}{2}\left(\frac{\partial u_2}{\partial x_1} - \frac{\partial u_1}{\partial x_2}\right)$) by expressing Γ_{12} and Γ_{21} in terms of displacement and setting these strains to be equal.

APPENDIX E

Buckling Load Predictions of Classical Beam Theories

The Euler-Bernoulli and Timoshenko theories were mentioned for comparison with the derived critical loads. In this section, these loads and their nondimensional forms, which were used in Fig. 5.2, will be stated. The generalized plane strain Euler-Bernoulli critical load (P_{cr}^{E}) for a simply-supported beam is,

$$P_{cr}^{E} = \frac{EI}{1-v^2}\frac{\pi^2}{a^2} \tag{E.1}$$

where E is Young's modulus, v is Poisson's ratio, and $I = \frac{1}{12}A(2h)^2$ is the area moment of inertia, with A being the cross section area at which the stress σ is applied and h, a are half the total height of the cross section and the length of the beam, respectively, as shown in Fig. 5.1. Next, P_{cr} is set in a nondimensional form;

$$P_{cr}^{E} = \frac{EI}{1-v^2}\frac{\pi^2}{a^2} = \frac{E(2h)^2A}{12(1+v)(1-v)}\left(\frac{2\pi}{L}\right)^2 = \frac{2\mu A}{3(1-v)}\left(\frac{2\pi h}{L}\right)^2 \tag{E.2a}$$

$$\tilde{s}_{cr}^{E} = \frac{\sigma_{cr}^{E}}{2\mu} = \frac{P_{cr}^{E}}{2A\mu} = \frac{1}{3(1-v)}\left(\frac{2\pi h}{L}\right)^2 \tag{E.2b}$$

where $\mu = \frac{E}{2(1+v)}$ is the shear modulus and $v = \frac{\tilde{\lambda}}{2(\tilde{\lambda}+1)}$.

In Timoshenko beam theory, the critical buckling load is

$$P_{cr}^{T} = \frac{P_{cr}^{E}}{1 + \frac{P_{cr}^{E}}{\mu A}} \tag{E.3}$$

In nondimensional form, Eqn. E.3 simplifies to

$$\tilde{s}_{cr}^{T} = \frac{\sigma_{cr}^{T}}{2\mu} = \frac{P_{cr}^{T}}{2A\mu} = \frac{\frac{\sigma_{cr}^{E}}{2\mu}}{1 + \frac{\sigma_{cr}^{E}}{m\mu}} = \frac{\frac{\sigma_{cr}^{E}}{2\mu}}{1 + \frac{2}{m}\left(\frac{\sigma_{cr}^{E}}{2\mu}\right)} \tag{E.4}$$

It was also stated in the development of Eqn. 5.32, that the 1DMB buckling load, $\tilde{s}_{cr}^{1DMB}$, reduces to the Timoshenko critical load $\tilde{s}_{cr}^{T}$ when $\tilde{\gamma} = \tilde{k} = 0$ ($\tilde{s}_{cr}^{1DMB}$=$\tilde{s}_{cr}^{T}$).

APPENDIX F

Homogenization Approaches

In Chapter 4, the micromechanics approach for obtaining the effective properties of cellular microstructure was discussed. In this appendix, the extension of such micromechanics methods to modeling a multi-phase continuous medium as a homogeneous micropolar continuum is discussed and the limitations of such approaches are highlighted. The problem is posed as follows: given a heterogeneous microstructure of N-phases (Fig. F.1), what is the corresponding effective stiffness of the homogenized micropolar material such that the strain energy stored in the heterogeneous composite (U_c) and the homogeneous micropolar material (U_h) equate, or

$$U_c = U_h \tag{F.1}$$

The heterogeneous domain is selected such that it is a representative volume element (RVE) of the composite. The domain of the RVE is denoted $\mathcal{B}$, with its boundary $\partial\mathcal{B}$. The geometry of the homogenized domain is assumed to correspond to the heterogeneous domain, with lengths l_1 and l_2, and a volume V as shown in Fig. F.1. Because we are interested in replacing the heterogeneous medium with a homogeneous micropolar medium, U_h is defined as,

$$U_h = \frac{V}{2}(\overline{S}_{ji}\overline{\delta E}_{ji} + \overline{T}_{ji}\overline{\delta A}_{ji} + \overline{M}_{j3}\overline{\delta k}_{j3}) \tag{F.2}$$

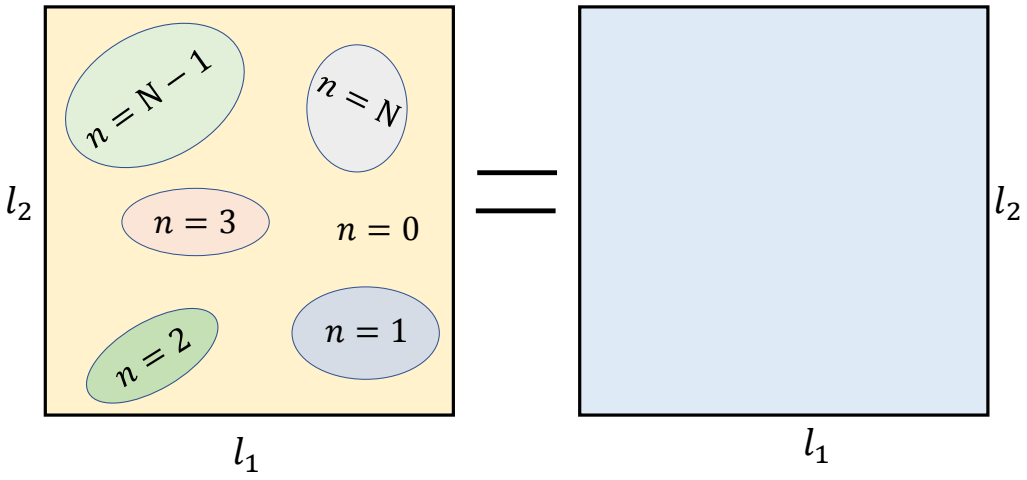

Figure F.1: Representation of a heterogeneous (left) microstructure with an equivalent homogenized medium (right).

An arbitrary displacement loading on the boundary $\partial\mathcal{B}$ does not always result in the assumption in Eqn. F.1. Employing the Hill-Mandel condition as discussed in Chapter 4 for cellular solids, the kinematic boundary conditions that are required to satisfy this for a N-phased micropolar continuum are

$$u_1 = \overline{E}_{11}x_1 + \overline{E}_{12}x_2 - \overline{\Omega}_3 x_2 \tag{F.3a}$$

$$u_2 = \overline{E}_{12}x_1 + \overline{E}_{22}x_2 + \overline{\Omega}_3 x_1 \tag{F.3b}$$

$$\varphi_3 = \overline{\Omega}_3 - \overline{A}_{12} + \overline{K}_{13}x_1 + \overline{K}_{23}x_2 \tag{F.3c}$$

where the kinematics and coordinates are specified on $\partial\mathcal{B}$. Given the general constitutive model between the effective stresses and strains,

$$\begin{bmatrix} \overline{S}_{11} \\ \overline{S}_{22} \\ \overline{S}_{12} \\ \overline{T}_{12} \\ \overline{M}_{13} \\ \overline{M}_{23} \end{bmatrix} = \begin{bmatrix} \overline{C}_{11} & \overline{C}_{12} & \overline{C}_{13} & \overline{C}_{14} & \overline{C}_{15} & \overline{C}_{16} \\ \overline{C}_{12} & \overline{C}_{22} & \overline{C}_{23} & \overline{C}_{24} & \overline{C}_{25} & \overline{C}_{26} \\ \overline{C}_{13} & \overline{C}_{23} & \overline{C}_{33} & \overline{C}_{34} & \overline{C}_{35} & \overline{C}_{36} \\ \overline{C}_{14} & \overline{C}_{24} & \overline{C}_{34} & \overline{C}_{44} & \overline{C}_{45} & \overline{C}_{46} \\ \overline{C}_{15} & \overline{C}_{25} & \overline{C}_{35} & \overline{C}_{45} & \overline{C}_{55} & \overline{C}_{56} \\ \overline{C}_{16} & \overline{C}_{26} & \overline{C}_{36} & \overline{C}_{46} & \overline{C}_{56} & \overline{C}_{66} \end{bmatrix} \begin{bmatrix} \overline{E}_{11} \\ \overline{E}_{22} \\ \overline{E}_{12} \\ \overline{A}_{12} \\ \overline{K}_{13} \\ \overline{K}_{23} \end{bmatrix} \tag{F.4}$$

to obtain the material constants $\overline{C}_{ij}$, a single strain is applied one at a time, while the remaining strain components are set to zero. The corresponding stress measures are obtained through

$$\overline{S}_{ij} = \frac{1}{2V}\int_{\partial\mathcal{B}} (t_i x_j + t_j x_i) dA \tag{F.5a}$$

$$\overline{T}_{12} = \frac{1}{2V}\varepsilon_{ji3}\int_{\partial\mathcal{B}} Q_3 dA \tag{F.5b}$$

$$\overline{M}_{i3} = \frac{1}{V}\int_{\partial\mathcal{B}} Q_3 x_i dA \tag{F.5c}$$

where t_i and Q_3 are the traction and couple-traction, respectively. For example, to determine the material constants $\overline{C}_{i5}$, the nonzero curvature $\overline{K}_{13}$ is specified, while the other strain components are set to zero. The corresponding displacements on $\partial\mathcal{B}$ are

$$u_1 = 0 \tag{F.6a}$$

$$u_2 = 0 \tag{F.6b}$$

$$\varphi_3 = \overline{K}_{13} x_1 \tag{F.6c}$$

Next, evaluating the macroscopic stresses with Eqn. F.5, the material constants $\overline{C}_{i5}$ are determined. The remaining material constants are obtained by applying the remaining strains. The limitation of the foregoing approach should be highlighted. In order for the rotational degrees of freedom to be specified on $\partial\mathcal{B}$, the heterogeneous medium must be such that rotation is kinematically admissible. This is possible for medium consisting of micropolar constituents or cellular beam/shell structures with rotational degrees of freedom. The extension of the micromechanics approach to obtain the effective micropolar properties of a heterogeneous N-phase Cauchy medium does not apply because of the inability to enforce rotations on the boundary of such constituents. As a result, micromechanics methods which are geared for this purpose need to be yet developed.

BIBLIOGRAPHY

[1] Eringen, A. C., "Theory of Micropolar Elasticity," Technical Report 1, Princeton University, Office of Naval Research Department of the Navy, June 1967.

[2] NG, W. H., Salvi, A. G., and Waas, A. M., "Characterization of the in-situ non-linear shear response of laminated fiber-reinforced composites," *Composites Science and Technology*, Vol. 70, No. 7, 2010, pp. 1126– 1134.

[3] Prabhakar, P. and Waas, A. M., "Upscaling from a micro-mechanics model to capture laminate compressive strength due to kink banding instability," *Computational Materials Science*, Vol. 67, 2013, pp. 40–47.

[4] Ji, W. and Waas, A. M., "2D elastic analysis of the sandwich panel buckling problem: benchmark solution and accurate finite element formulations," *Zeitschrift fr angewandte Mathematik und Physik*, Vol. 61, 2010, pp. 897–917.

[5] Dyszlewicz, J., "Problem of Stress Concentration in a Micropolar Medium Problem of Circular Hole," *Studia Geotechnica et Mechanica*, Vol. 8, 1986, pp. 25–36.

[6] Dyszlewicz, J., "On the Concentration of Stresses in a Micropolar Medium. Problem of a Perfectly Stiff Circular Inclusion," *Studia Geotechnica et Mechanica*, Vol. 9, No. 1-2, 1987, pp. 59–69.

[7] Kaloni, P. N. and Ariman, T., "Stress concentration effects in micropolar elasticity," *Zeitschrift fr angewandte Mathematik und Physik*, Vol. 18, No. 1, 1967, pp. 136–141.

[8] Bernard, X. D., Eichhubl, P., and Aydin, A., "Dilation bands: A new form of localized failure in granular media," *Geophysical Research Letters*, Vol. 29, No. 24, 2002, pp. 1–4.

[9] Aydin, A., Borja, R. I., and Eichhubl, P., "Geological and mathematical framework for failure modes in granular rock," *Journal of Structural Geology*, Vol. 28, No. 1, 2006, pp. 83–98.

[10] Wei, Q., Kecskes, L., Jiao, T., Hartwig, K. T., Ramesh, K. T., and Ma, E., "Adiabatic shear banding in ultrafine-grained Fe processed by severe plastic deformation," *Acta Materialia*, Vol. 52, No. 7, 2004, pp. 1859–1869.

[11] Abeyaratne, R. and Triantafyllidis, N., "The emergence of shear bands in plane strain," *International Journal of Solids and Structures*, Vol. 17, No. 12, 1981, pp. 1113–1134.

[12] Chen, Z. and Schreyer, H. L., "A numerical solution scheme for softening problems involving total strain control," *Computers and Structures*, Vol. 37, No. 6, 1989, pp. 1043–1050.

[13] Cervera, M., Chiumenti, M., and Capua, D. D., "Benchmarking on bifurcation and localization in J2 plasticity for plane stress and plane strain conditions," *Computer Methods in Applied Mechanics and Engineering*, Vol. 241-244, No. 1, 2012, pp. 206–224.

[14] Belyschko, T., Liu, W. K., and Moran, B., *Nonlinear Finite Elements for Continua and Structures*, John Wiley and Sons, 2000.

[15] De Borst, R., Sluys, L. J., Muhlhaus, H. B., and Pamin, J., "Fundamental Issues in Finite Element Analysis of Localization of Deformation," *Engineering computations*, Vol. 10, No. 99-121, 1993, pp. 99–121.

[16] Baant, Z. P. and Belytschko, T. B., "Continuum Theory for Strain Softening," *Journal of Engineering Mechanics*, Vol. 110, No. 12, 1984, pp. 1666–1692.

[17] Lasry, D. and Belytschko, T., "Localization limiters in transient problems," *International Journal of Solids and Structures*, Vol. 24, No. 6, 1988, pp. 581–597.

[18] Triantafyllidis, N. and Aifantis, E. C., "A gradient approach to localization of deformation. I. hyperelastic materials," *Journal of Elasticity*, Vol. 16, No. 3, 1986, pp. 225–237.

[19] Rosen, B. W., "Mechanics of composite strengthening," *Fiber Composite Materials*, 1965, pp. 37–75.

[20] Argon, A. S., "Fracture of Composites," *Treatise of Materials Science and Technology*, Vol. 1, 1972, pp. 79–114.

[21] Budiansky, B. and Fleck, N. A., "Compressive failure of fibre composites," *Journal of the Mechanics and Physics of Solids*, Vol. 41, No. 1, 1993, pp. 183–211.

[22] Kyriakides, S., Arseculeratne, R., Perry, E. J., and Liechti, K. M., "On the compressive failure of fiber reinforced composites," *International Journal of Solids and Structures*, Vol. 32, No. 6-7, 1995, pp. 689–738.

[23] Lee, S. H. and Waas, A. M., "Compressive response and failure of fiber reinforced unidirectional composites," *International Journal of Fracture*, Vol. 100, No. 3, 1999, pp. 275– 306.

[24] Davidson, P. and Waas, A. M., "Mechanics of kinking in fiber-reinforced composites under compressive loading," *Mathematics and Mechanics of Solids*, Vol. 21, No. 6, 2016, pp. 667– 684.

[25] Schultheisz, C. R. and Waas, A. M., "Compressive failure of composites, part I: Testing and micromechanical theories," *Progress in Aerospace Sciences*, Vol. 32, No. 1, 1996, pp. 1– 42.

[26] Waas, A. M. and Schultheisz, C. R., "Compressive failure of composites, part II: Experimental studies," *Progress in Aerospace Sciences*, Vol. 32, No. 1, 1996, pp. 43– 78.

[27] Gibson, L. J. and Ashby, M. F., *Cellular Solids: Structure and Properties*, Cambridge University Press, 1999.

[28] D'Mello, R. J., *Compression Response and Energy Absorption of Filled Circular Cell Honeycombs*, PhD Thesis, University of Michigan, 2014.

[29] Shaw, M. C. and Sata, T., "The plastic behavior of cellular materials," *International Journal of Mechanical Sciences*, Vol. 8, No. 7, 1966, pp. 469–472.

[30] Prabhakar, P., *Failure Mode Interaction in Fiber Reinforced Laminated Composites*, PhD Thesis, University of Michigan, 2013.

[31] Hasanyan, A. D. and Waas, A. M., "Localization in Anisotropic Elastoplastic Micropolar Media: Application to Fiber," *Journal of the Mechanics and Physics of Solids (accepted for publication)*, 2018.

[32] Hasanyan, A. D. and Waas, A. M., "Compressive Failure of Fiber Composites: A Homogenized, Mesh Independent Model," *2018 AIAA/ASCE/AHS/ASC Structures, Structural Dynamics, and Materials Conference*, 2018, pp. 1–28.

[33] Hasanyan, A. D. and Waas, A. M., "Micropolar constitutive relations for cellular solids," *Journal of Applied Mechanics*, Vol. 83, No. 4, 2016, pp. 1–10.

[34] Hasanyan, A. D. and Waas, A. M., "On the Buckling of a Two-Dimensional Micropolar Strip," *Journal of Applied Mechanics*, Vol. 82, No. 4, 2015, pp. 1–10.

[35] Sun, C. T. and Chen, J. L., "A Simple Flow Rule for Characterizing Nonlinear Behavior of Fiber Composites," *Journal of Composite Materials*, Vol. 23, 1989, pp. 1009–1020.

[36] Fleck, N. A. and Shu, J. Y., "Microbuckle initiation in fiber composites: a finite element study," *Journal of the Mechanics and Physics of Solids*, Vol. 43, No. 12, 1995, pp. 1887–1918.

[37] Steigmann, D. J., "Theory of elastic solids reinforced with fibers resistant to extension, flexure and twist," *International Journal of Non-Linear Mechanics*, Vol. 47, No. 7, 2012, pp. 734–742.

[38] Steigmann, D. J., "Effects of Fiber Bending and Twisting Resistance on the Mechanics of Fiber-reinforced Elastomers," *Nonlinear Mechanics of Soft Fibrous Materials*, Vol. 559, 2015, pp. 269–305.

[39] Goda, I., Assidi, M., and Ganghoffer, J. F., "A 3D elastic micropolar model of vertebral trabecular bone from lattice homogenization of the bone microstructure," *Biomechanics and Modeling in Mechanobiology*, Vol. 13, No. 1, 2014, pp. 53–83.

[40] Ostoja-Starzewski, M., *Microstructural Randomness and Scaling in Mechanic of Materials*, chap. 6, Chapman and Hall, London, 2008.

[41] De Borst, R., "Simulation of strain localization: a reappraisal of the Cosserat continuum," *Engineering computations*, Vol. 8, No. 4, 1991, pp. 317–332.

[42] Ramezani, S., Naghdabadi, R., and Sohrabpour, S., "Non-linear finite element implementation of micropolar hypo-elastic materials," *Computer Methods in Applied Mechanics and Engineering*, Vol. 197, No. 49–50, 2008, pp. 4149–4159.

[43] Steinmann, P., "A micropolar theory of finite deformation and finite rotation multiplicative elastoplasticity," *International Journal of Solids and Structures*, Vol. 31, No. 8, 1994, pp. 1063–1084.

[44] Neff, P., "A finite-strain elasticplastic Cosserat theory for polycrystals with grain rotations," *International Journal of Engineering Science*, Vol. 44, No. 8–9, 2006, pp. 574–594.

[45] Neff, P. and Mnch, I., "Simple shear in nonlinear Cosserat elasticity: Bifurcation and induced microstructure," *Continuum Mechanics and Thermodynamics*, Vol. 21, No. 3, 2009, pp. 195–221.

[46] Alsaleh, M. I., Voyiadjis, G. Z., and Alshibli, K. A., "Modelling strain localization in granular materials using micropolar theory: mathematical formulations," *International Journal for Numerical and Analytical Methods in Geomechanics*, Vol. 30, No. 15, 2006, pp. 1501–1524.

[47] Bathe, K.-J., *Finite element procedures*, Pretice-Hall, 1996.

[48] Prabhakar, P. and Waas, A. M., "Interaction between kinking and splitting in the compressive failure of unidirectional fiber reinforced laminated composites," *Composite Structures*, Vol. 98, 2013, pp. 85–92.

[49] Yerramalli, C. S. and Waas, A. M., "The Effect of Fiber Diameter on the Compressive Strength of Composites - A 3D Finite Element Based Study," *Computer Modeling in Engineering and Sciences*, Vol. 6, No. 1, 2004, pp. 1–16.

[50] Yerramalli, C. S. and Waas, A. M., "Micromechanics model for damage and failure analyses of laminated fibrous composites," *Engineering Fracture Mechanics*, Vol. 52, No. 2, 1995, pp. 231–242.

[51] Li, V. C., Wang, Y., and Backe, S., "A micromechanical model of tension-softening and bridging toughening of short random fiber reinforced brittle matrix composites," *Journal of the Mechanics and Physics of Solids*, Vol. 39, No. 5, 1991, pp. 607–625.

[52] Christensen, R. M., *Mechanics of Composite Materials*, Wiley, 1979.

[53] Zhang, D., , and Waas, A. M., "A micromechanics based multiscale model for nonlinear composites," *Acta Mechanica*, Vol. 225, No. 4-5, 2014, pp. 1391– 1417.

[54] Patel, D. K., Hasanyan, A. D., and Waas, A. M., "N-Layer concentric cylinder model (NCYL): an extended micromechanics-based multiscale model for nonlinear composites," *Acta Mechanica*, Vol. 228, No. 1, 2016, pp. 275– 306.

[55] Onck, P. R., "Cosserat modeling of cellular solids," *Comptes Rendus Mcanique*, Vol. 330, No. 11, 2002, pp. 717– 722.

[56] Trovalusci, P., Ostoja-Starzewski, M., De Bellis, M. L., and Murrali, A., "Scale-dependent homogenization of random composites as micropolar continua," *European Journal of Mechanics - A/Solids*, Vol. 49, 2015, pp. 396– 407.

[57] Forest, S. and Sab, K., "Cosserat overall modeling of heterogeneous materials," *Mechanics Research Communications*, Vol. 25, No. 4, 1998, pp. 449– 454.

[58] De Bellis, M. L. and Addessi, D., "A Cosserat based multi-scale model for masonry structures," *International Journal for Multiscale Computational Engineering*, Vol. 9, No. 5, 2011, pp. 543– 563.

[59] Hsu, S. Y., Vogler, T. J., and Kyriakides, S., "Compressive Strength Predictions for Fiber Composites," *Journal of Applied Mechanics*, Vol. 65, No. 7, 1998, pp. 7–16.

[60] Lin, T.-C., Chen, T.-J., and Huang, J.-S., "In-plane elastic constants and strengths of circular cell honeycombs," *Composite Science and Technology*, Vol. 72, No. 12, 2012, pp. 1380–1386.

[61] Chung, J. and Waas, A. M., "In-Plane Biaxial Crush Response of Polycarbonate Honeycombs," *Journal of Engineering Mechanics*, Vol. 127, No. 2, 2001, pp. 180–193.

[62] D'Mello, R. J. and Waas, A. M., "Inplane crush response and energy absorption of circular cell honeycomb filled with elastomer," *Composite Structures*, Vol. 106, No. 1, 2013, pp. 491–501.

[63] Papka, S. D. and Kyriakides, S., "In-plane Crushing of a Polycarbonate Honeycomb," *International Journal of Solids and Structures*, Vol. 35, No. 3–4, 2013, pp. 491–501.

[64] Poritski, H. and Horvay, G., "Stresses in Pipe Bundles," *Journal of Applied Mechanics*, Vol. 18, 1951, pp. 241–250.

[65] Chung, J. and Waas, A. M., "The inplane elastic properties of circular cell and elliptical cell honeycombs," *Acta Mechanica*, Vol. 144, No. 1, 2000, pp. 29–42.

[66] Lin, T.-C. and Huang, J.-S., "In-plane mechanical properties of elliptical cell honeycombs," *Composite Structures*, Vol. 104, 2013, pp. 14–20.

[67] Baant, Z. P. and Christensen, M., "Analogy between micropolar continuum and grid frames under initial stress," *International Journal of Solids and Structures*, Vol. 8, No. 3, 1972, pp. 327–346.

[68] Kumar, R. S. and McDowell, D. L., "Generalized continuum modeling of 2-D periodic cellular solids," *International Journal of Solids and Structures*, Vol. 41, No. 26, 2004, pp. 7399–7422.

[69] Chen., J. Y., Huang, Y., and Ortiz, M., "Fracture analysis of cellular materials: A strain gradient model," *Journal of the Mechanics and Physics of Solids*, Vol. 46, No. 5, 1998, pp. 789–828.

[70] Wang, X. L. and Stronge, W. J., "Micropolar Theory for two-dimensional stresses in elastic honeycomb," *The Royal Society*, Vol. 445, No. 1986, 1999, pp. 2091–2116.

[71] Mora, R. J. and Waas, A. M., "Evaluation of the Micropolar elasticity constants for honeycombs," *Acta Mechanica*, Vol. 192, No. 1, 2007, pp. 1–16.

[72] Chung, J. and Waas, A. M., "The micropolar elasticity constants of circular cell honeycombs," *Proceeding of the Royal Society A*, Vol. 465, No. 2101, 2009, pp. 25–39.

[73] Fatemi, J., Onck, P. R., Poort, G., and Keulen, F. V., "Cosserat moduli of anisotropic cancellous bone: A micromechanical analysis," *Journal de Physique IV*, Vol. 105, 2003, pp. 273–280.

[74] Jasiuk, I. and Ostoja-Starzewski, M., "From Lattices and Composites to Micropolar Continua," *Micromechanics and Nanoscale Effects*, Vol. 10, No. 12, 2003, pp. 175–212.

[75] Li, X. and Liu, Q., "A version of Hills lemma for Cosserat continuum," *Acta Mechanica Sinica*, Vol. 25, No. 4, 2009, pp. 499–506.

[76] Hohe, J. and Becher, W., "Effective stress-strain relations for two-dimensional cellular sandwich cores: Homogenization, material models, and properties," *Applied Mechanics Reviews*, Vol. 55, No. 1, 2001, pp. 61–87.

[77] Kumar, R. and Partap, G., "Rayleigh Lamb Waves in Micropolar Isotropic Elastic Plate," *Applied Mathematics and Mechanics*, Vol. 27, No. 8, 2006, pp. 1049–1059.

[78] Nowacki, W. and Olszak, W., *Micropolar Elasticity*, Springer, 1970.

[79] Ding, N., Xu, X., and Zheng, Z., "A size-dependent nonlinear microbeam model based on the micropolar elasticity theory," *Acta Mechanica*, Vol. 227, No. 12, 2016, pp. 3497–3515.

[80] Khorshidi, M. A., Shariati, M., and Emam, S. A., "Postbuckling of functionally graded nanobeams based on modified couple stress theory under general beam theory," *International Journal of Mechanical Sciences*, Vol. 110, 2016, pp. 160–169.

[81] Khorshidi, M. A., Shariati, M., and Emam, S. A., "Bending analysis of micropolar elastic beam using a 3-D finite element method," *International Journal of Engineering Science*, Vol. 38, No. 3, 2000, pp. 275–286.

[82] Kafadar, C. B. and Eringen, A. C., "Micropolar Media-I The Classical Theory," *International Journal of Engineering Science*, Vol. 9, No. 3, 1971, pp. 271–305.

[83] Erbay, S., Erbay, H. A., and Dost, S., "Nonlinear wave modulation in micropolar elastic media I. Longitudinal waves," *International Journal of Engineering Science*, Vol. 29, No. 7, 1991, pp. 845–858.

[84] Gauthier, R. D. and Jahsman, W. E., "A Quest for Micropolar Elastic Constants," *Journal of Applied Mechanics*, Vol. 42, No. 2, 1975, pp. 369–374.

[85] Ramezani, S., Naghdabadi, R., and Sohrabpour, S., "Analysis of micropolar elastic beams," *European Journal of Mechanics A/Solids*, Vol. 28, No. 2, 2009, pp. 202–208.